



THE HONG KONG
POLYTECHNIC UNIVERSITY

香港理工大學

Pao Yue-kong Library

包玉剛圖書館

Copyright Undertaking

This thesis is protected by copyright, with all rights reserved.

By reading and using the thesis, the reader understands and agrees to the following terms:

1. The reader will abide by the rules and legal ordinances governing copyright regarding the use of the thesis.
2. The reader will use the thesis for the purpose of research or private study only and not for distribution or further reproduction or any other purpose.
3. The reader agrees to indemnify and hold the University harmless from and against any loss, damage, cost, liability or expenses arising from copyright infringement or unauthorized usage.

IMPORTANT

If you have reasons to believe that any materials in this thesis are deemed not suitable to be distributed in this form, or a copyright owner having difficulty with the material being included in our database, please contact lbsys@polyu.edu.hk providing details. The Library will look into your claim and consider taking remedial action upon receipt of the written requests.

The Hong Kong Polytechnic University

Department of Applied Physics

**Low-Temperature Sintered Lead-free
Piezoelectric Ceramics and Their Applications
for Vibratory Gyrosensors**

WONG MAU TAK

A thesis submitted in partial fulfillment of the requirements for
the degree of Master of Philosophy

July 2013

CERTIFICATE OF ORIGINALITY

I hereby declare that this thesis is my own work and that, to the best of my knowledge and belief, it reproduces no material previously published or written, nor material that has been accepted for the award of any other degree or diploma, except where due acknowledgement has been made in the text.

_____ (Signed)

WONG MAU TAK (Name of student)



Abstract

The main objectives of the present work are to prepare low-temperature sintered lead-free piezoelectric ceramics and to fabricate piezoelectric vibratory gyro-sensors using the lead-free piezoelectric ceramics. For environmental protection reasons, lead-free piezoelectric ceramics have been extensively studied for replacing the widely used piezoelectric ceramics such as $\text{PbZr}_x\text{Ti}_{1-x}\text{O}_3$ (PZT), which contain a large amount of toxic lead. $\text{K}_{0.5}\text{Na}_{0.5}\text{NbO}_3$ (KNN) is one of the most promising candidates for the lead-free piezoelectric ceramics. Besides the saving of energy, low-temperature sintering is always an important topic for the fabrication of ceramic components, in particular for co-fired multi-layered components. The low sintering temperature allows the use of relatively cheap inner electrodes, such as Pd/Ag rather than Pt. In this work, two methods, high-energy ball milling and liquid phase sintering, have been evaluated for lowering the sintering temperature of $0.91\text{K}_{0.47}\text{Na}_{0.47}\text{Li}_{0.06}\text{NbO}_3\text{-}0.09\text{NaSbO}_3$ (KNLN-NS) ceramics which have been shown to possess good piezoelectric properties.

The high-energy ball milling technique has been shown to be effective in reducing the grain size and lowering the sintering temperature of a number of compounds and oxides, including perovskite oxides. Our results show that the grains of the KNLN-NS ceramics are reduced from $\sim 3 \mu\text{m}$ to $\sim 1 \mu\text{m}$ after the high-energy ball milling process at 200 rpm for 2 h. However, there is no significant change in the sintering temperature that remains at a high temperature of 1080°C . On the other hand, probably due to the smaller grain size, the piezoelectric properties of the ceramics decrease by about 30%.



THE HONG KONG POLYTECHNIC UNIVERSITY

A sintering aid comprising of Cu and Ba in a molar ratio of 71.5/28.5 has been used to lower the sintering temperature of the KNLN-NS ceramics. The sintering aid is effective in decreasing the sintering temperature, improving the densification and reducing the dielectric loss of the KNLN-NS ceramics. For the ceramic added with 2.5 wt% of the sintering aid (i.e., KNLN-NS-Cu/Ba-2.5), the sintering temperature is decreased to 980°C, the density is increased to $\sim 4.4 \text{ g/cm}^3$ and the dielectric loss is reduced to 1.0%. As the sintering aid becomes molten at a eutecture temperature of 890°C, the densification of the ceramics is promoted via liquid-phase sintering. However, partly due to the secondary phase and hardening effect, the piezoelectric properties of the KNLN-NS-Cu/Ba-2.5 ceramics are decreased, giving a d_{33} of 134 pC/N. If less sintering aid is used, the ceramics become porous, the density decreases and the dielectric loss at low frequencies is sensitive to moisture. However, they can still be effectively poled at high temperatures and exhibit relatively good and stable piezoelectric properties ($d_{33} = 153 \text{ pC/N}$). Owing to the low sintering temperature and dielectric loss, the KNLN-NS-Cu/Ba ceramics are promising for practical applications, in particular for multi-layered components.

Bimorph-type piezoelectric vibratory gyro-sensors have been fabricated using both the KNLN-NS (sintered at 1080°C) and KNLN-NS-Cu/Ba (sintered at 1000°C) ceramics, and an electronic readout circuit has been developed to detect the small signals induced in the gyro-sensors subjected to a rotation and to give a dc output voltage proportional to the rotation speed. The piezoelectric vibratory gyro-sensor is made up of a stack of two oppositely poled ceramic plates and is electrically driven to vibrate at its bending resonance frequency. Subjected to a rotation, a Coriolis force is



THE HONG KONG POLYTECHNIC UNIVERSITY

induced, bending it in a direction normal to both the vibrating and rotation directions. The charges induced on the gyro-sensor by the induced bending are detected by the electronic readout circuit that comprising of charge amplifiers, differential amplifier and demodulator. All the gyro-sensors exhibit a linear relationship between the dc output voltage and rotation speed. Our results also show that the high dielectric loss at low frequencies of the KNLN-NS-Cu/Ba ceramic arisen from moisture absorption does not affect the performance of gyro-sensors that operated at high frequencies such as 20-30 kHz. A good compromise between the dimension and sensitivity is obtained for a gyro-sensor of size 4 mm × 0.6 mm × 0.6 mm. The sensitivity of such a gyro-sensor fabricated using the KNLN-NS-Cu/Ba ceramic reaches a high value of 0.57-0.84 mV/dps in the range of -360 dps to +360 dps.



Acknowledgements

I would like to acknowledge my supervisor, Dr. K. W. Kwok for his continuous encouragement, support and guidance during this study.

I would also like to thank the technical support provided by the Materials Research Centre (MRC) of the Hong Kong Polytechnic University.

Finally, I would like to acknowledge the support from my family and my friends during this study.



Table of contents

Abstract	I
Acknowledgements	IV
Table of contents.....	V
List of figures and tables	IX
List of publications	XIV
CHAPTER 1 INTRODUCTION	15
1.1 INTRODUCTION.....	15
1.2 BACKGROUND	15
1.3 PIEZOELECTRICITY AND FERROELECTRICITY	17
<i>1.3.1 Piezoelectricity</i>	17
<i>1.3.2 Ferroelectricity</i>	19
<i>1.3.3 KNN-based Piezoelectric Ceramics</i>	21
1.4 LOW-TEMPERATURE SINTERING TECHNIQUES	26
<i>1.4.1 High Energy Ball Milling</i>	28
<i>1.4.2 Sintering Aids</i>	31
1.5 GYRO-SENSORS	34
<i>1.5.1 Coriolis Effect</i>	35
<i>1.5.2 Piezoelectric Vibratory Gyro-sensors</i>	36
1.5.2.1 Tuning Fork Gyro-sensor.....	37
1.5.2.2 Thickness-shear Plate Gyro-sensor.....	38
1.5.2.3 Circular Cylindrical Shell Gyro-sensor	39



THE HONG KONG POLYTECHNIC UNIVERSITY

1.5.2.4 Ring Gyro-sensor..... 41

1.5.2.5 Bimorph-type (beam-type) Gyro-sensor..... 43

1.6 SCOPE OF WORK 45

CHAPTER 2 FABRICATION OF PIEZOELECTRIC CERAMICS AND PIEZOELECTRIC GYRO-SENSORS..... 46

2.1 INTRODUCTION..... 46

2.2 FABRICATION OF PIEZOELECTRIC CERAMICS..... 46

 2.2.1 *Ball Milling and High-energy Ball Milling*..... 47

 2.2.2.1 Conventional Ball Milling 48

 2.2.2.2 High-energy Ball Milling..... 49

 2.2.2 *Calcination* 49

 2.2.3 *Sintering Aids* 50

 2.2.4 *Dry Pressing* 50

 2.2.5 *Binder Removal and Sintering*..... 51

 2.2.6 *Polishing and Electroding* 54

 2.2.7 *Poling* 54

2.3 FABRICATION OF PIEZOELECTRIC VIBRATORY GYRO-SENSORS 57

 2.3.1 *Preparation of Piezoelectric Plates*..... 59

 2.3.2 *Stacking, Cutting and Electroding the Bimorph Beams Gyro-sensors* 59

CHAPTER 3 CHARACTERIZATIONS OF CERAMICS 61

3.1 INTRODUCTION..... 61

3.2 DENSITY 61



THE HONG KONG POLYTECHNIC UNIVERSITY

3.3 CRYSTALLINE STRUCTURE 62

3.4 MICROSTRUCTURE 63

3.5 FERROELECTRIC HYSTERESIS LOOP 63

3.6 DIELECTRIC PROPERTIES 65

3.7 PIEZOELECTRIC PROPERTIES MEASUREMENT 66

3.8 RESULTS AND DISCUSSION 67

 3.8.1 KNLN-NS Ceramics Prepared by High-Energy Ball Milling 67

 3.8.2 KNLN-NS ceramics prepared Using Sintering Aid..... 72

 3.8.2.1 KNLN-NS Ceramics..... 72

 3.8.2.2 KNLN-NS-Cu/Ba Ceramics 77

3.9 SUMMARY 90

CHAPTER 4 CHARACTERIZATION OF PIEZOELECTRIC GYRO-SENSORS 92

4.1 INTRODUCTION..... 92

4.2 ELECTRONIC READOUT CIRCUIT 94

 4.2.1 Charge Amplifier 95

 4.2.2 Phase shifter 96

 4.2.3 Differential amplifier 97

 4.2.4 Demodulator..... 98

 4.2.5 Low Pass Filter..... 99

 4.2.6 Voltage amplifier..... 100

4.3 RESULTS AND DISCUSSION 101

 4.3.1 KNLN-NS Ceramic Gyro-sensors 101



THE HONG KONG POLYTECHNIC UNIVERSITY

4.3.2 KNLN-NS-Cu/Ba Ceramic Gyro-sensors..... 107

4.4 SUMMARY 111

CHAPTER 5 CONCLUSIONS..... 113

REFERENCES..... 115



List of figures and tables

Figure 1.1 The direct piezoelectric effect.	18
Figure 1.2 Perovskite crystal structure of ABO_3	18
Figure 1.3 The relationship between dielectrics, piezoelectrics, pyroelectrics and ferroelectrics.	19
Figure 1.4 A typical ferroelectric hysteresis loop.	20
Figure 1.5 Phase diagram of the system $KNbO_3$ - $NaNbO_3$ [3].	23
Figure 1.6 Coriolis effect on vibrating object.	36
Figure 1.7 The Schematic diagram of tuning fork gyro-sensor [81].	38
Figure 1.8 The Schematic diagram of thickness-shear plate gyro-sensor [88].	39
Figure 1.9 The Schematic diagram of circular cylindrical shell gyro-sensor [96].	40
Figure 1.10 Vibration modes of circular cylindrical shell gyro-sensor: (a) sensing mode, (b) driving mode [96].	41
Figure 1.11 The Schematic diagram of a ring gyro-sensor [96].	42
Figure 1.12 The vibration modes of a ring gyro-sensor [96].	42
Figure 1.13 The schematic diagram of bimorph beam gyro-sensor.	44
Figure 2.1 Flow chat for fabrication of piezoelectric ceramics.	47
Figure 2.2 Schematic diagram showing the ball milling.	48
Figure 2.3 Schematic diagram of the dry pressing of ceramic disk.	51
Figure 2.4 Schematic diagram of the binder removal process.	52
Figure 2.5 Temperature profile of the binder removal process.	52
Figure 2.6 Temperature profile of the sintering process.	53



THE HONG KONG POLYTECHNIC UNIVERSITY

Figure 2.7 Schematic diagrams of stages in solid-state sintering [98].....53

Figure 2.8 Temperature profile of the silver electrodes firing process.54

Figure 2.9 The switching of the ferroelectric grains polarization under DC electric field.
.....55

Figure 2.10 Schematic diagram of the DC poling circuit for ceramic sample.....56

Figure 2.11 The polarization directions of the piezoelectrics.58

Figure 2.12 The schematic diagram of piezoelectric vibratory gyro-sensor.....58

Figure 2.13 The schematic diagram of cutting the double layers ceramic into rod shape.
.....60

Figure 3.1 The schematic diagram of X-ray diffraction in crystal.....63

Figure 3.2 Schematic diagram of the experiment setup for P-E loop measurement.....65

Figure 3.3 The schematic diagram of a d_{33} meter.67

Figure 3.4 SEM micrograph of the KNN ceramic prepared by CBM.68

Figure 3.5 SEM micrograph of the KNN ceramic prepared by HEBM.69

Figure 3.6 Ferroelectric hysteresis loops of the KNLIN-NS ceramics prepared by CBM
and HEBM.70

Figure 3.7 SEM micrograph of the KNLN-NS ceramic prepared by CBM.71

Figure 3.8 SEM micrograph of the KNLN-NS ceramic prepared by HEBM.....71

Figure 3.9 Density measurement of KNLN-NS with different sintering temperature....72

Figure 3.10 SEM micrograph of KNLN-NS sintering at (a) 1080°C, (b) 1060°C, (c)
1040°C, (d) 1020°C and (e) 1000 °C.....73

Figure 3.11 Dielectric properties of KNLN-NS of different sintering temperature
measured at 1 kHz.....74



THE HONG KONG POLYTECHNIC UNIVERSITY

Figure 3.12 Piezoelectric properties of KNLN-NS of different sintering temperature. .75

Figure 3.13 Variation of ϵ_r with the day after poled for KNLN-NS ceramics.76

Figure 3.14 Variation of $\tan\delta$ with the day after poled for KNLN-NS ceramics.77

Figure 3.15 Variation of density with x for the KNLN-NS-Cu/Ba-x ceramics.78

Figure 3.16 SEM micrographs of the KNLN-NS-Cu/Ba-x ceramics: (a) x = 1.25; (b) x = 2.5; (c) x = 3.75; and (d) x = 5.79

Figure 3.17 Ferroelectric hysteresis loops (100Hz) of KNLN-NS-Cu/Ba-x ceramics: (a) x = 0; (b) x = 1.25; (c) x = 2.5; (d) x = 3.75; and (e) x = 5.80

Figure 3.18 E_c and P_r of KNLN-NS-Cu/Ba-x ceramics measured at 100 Hz.....81

Figure 3.19 X-ray diffraction patterns of the KNLN-NS-Cu/Ba-x ceramics: (a) $\theta = 20^\circ$ - 80° and (b) $\theta = 44^\circ$ - 48°82

Figure 3.20 Dielectric properties of KNLN-NS-Cu/Ba-x ceramics measured at 1 kHz.83

Figure 3.21 Piezoelectric properties of KNLN-NS-Cu/Ba-x ceramics.....84

Figure 3.22 Dielectric properties of KNLN-NS-Cu/Ba-x ceramics measured at 1 kHz after poled.....85

Figure 3.23 Density measurement of KNLN-NS-Cu/Ba-2.5 sintered at different temperature.....87

Figure 3.24 SEM micrograph of KNLN-NS-Cu/Ba-2.5 sintered at (a) 1020°C , (b) 1000°C , (c) 980°C , (d) 960°C and (e) 940°C88

Figure 3.25 Dielectric properties of KNLN-NS-Cu/Ba-2.5 sintered at different temperature measured at 1 kHz.....89

Figure 3.26 Piezoelectric properties of KNLN-NS-Cu/Ba-2.5 sintered at different temperature.....90



THE HONG KONG POLYTECHNIC UNIVERSITY

Figure 4.1 Photo of the readout circuit. 93

Figure 4.2 The block diagram of the readout circuit..... 94

Figure 4.3 The circuit diagram of the charge amplifier..... 96

Figure 4.4 The circuit diagram of phase shifter. 97

Figure 4.5 The circuit diagram of the differential amplifier. 98

Figure 4.6 The circuit diagram of the demodulator..... 99

Figure 4.7 The circuit diagram of the low pass filter. 100

Figure 4.8 The circuit diagram of the voltage amplifier. 101

Figure 4.9 Photo of KNLN-NS gyro-sensors with the dimension of: (a) 1mm × 9 mm,
(b) 0.6mm × 4 mm, (c) 0.6mm × 3 mm, (d) 0.6mm × 2 mm..... 102

Figure 4.10 Photo depicting the connections of gyro-sensor. 103

Figure 4.11 Impedance and phase spectra of the KNLN-NS gyro-sensors with the
dimension of (a) 1mm × 9 mm, (b) 0.6mm × 4 mm, (c) 0.6mm × 3 mm, (d)
0.6mm × 2 mm. 104

Figure 4.12 Experiment setup for gyro-sensor output measurement. 106

Figure 4.13 The output voltage against rotation speed curves of different KNLN-NS
gyro-sensors. 107

Figure 4.14 Photo KNLN-NS-Cu/Ba-x gyro-sensors: (a) x = 1.25 and (b) x = 2.5..... 109

Figure 4.15 Impedance and phase spectra of the KNLN-NS-Cu/Ba-x gyro-sensors: (a) x
= 1.25 and (b) x = 2.5..... 109

Figure 4.16 The tanδ spectrum of KNLN-NS-Cu/Ba-1.25 ceramics..... 110

Figure 4.17 The output voltage against rotation speed curves of KNLN-NS-Cu/Ba-x
piezoelectric gyro-sensors..... 111



Table 1.1 Characteristic of KNN ceramics with different preparation methods.....24

Table 1.2 Summary of the properties of KNN doped with different materials by Guo *et al.*.....25

Table 1.3 Piezoelectric properties of KNLN-NS and PZT.....26

Table 2.1 General processing conditions for fabricating the KNLN-NS ceramics.....57

Table 3.1 Characteristics of KNN ceramics prepared by CBM and HEBM..... 68

Table 3.2 Charateristic of KNLN-NS ceramics prepared by CBM and HEBM. 70

Table 4.1 Characteristic of the KNLN-NS gyro-sensors. 105

Table 4.2 Characteristic of the KNLN-NS-Cu/Ba gyro-sensors 108



List of publications

1. Mau-Tak Wong and K.W. Kwok, “Low-Temperature Sintered $K_{0.5}Na_{0.5}NbO_3$ -Based Ceramics for Vibratory Gyro-sensor Applications”, **International Journal of Applied Ceramic Technology**. (Submitted)



Chapter 1 Introduction

1.1 Introduction

This chapter briefly describes the fundamentals of piezoelectricity and ferroelectricity. A short review of literature on the studies of lead-free KNN-based materials is given to introduce the properties of those materials. A short review of literature on the studies of low-temperature sintering techniques is given to discuss the achievements. A brief introduction of bimorph piezoelectric gyro-sensors is given to explain the structure and working principle. Finally, the scope of work is given to introduce the work of this project and the details of each chapter.

1.2 Background

Piezoelectric materials are technologically important because of their applications in various kinds of devices including gyroscope, ultrasonic medical imaging, ultrasonic nondestructive testing, speakers, resonators, gas igniters, pressure sensors etc [1,2,3]. Due to the excellent piezoelectric and ferroelectric properties, lead-based materials, such as $\text{PbZr}_x\text{Ti}_{1-x}\text{O}_3$ (PZT), $\text{Pb}(\text{Mg}_{1/3}\text{Nb}_{2/3})\text{O}_3$ (PMN), $\text{Pb}(\text{Mg}_{1/3}\text{Nb}_{2/3})\text{O}_3\text{-PbTiO}_3$ (PMN-PT) and $\text{Pb}(\text{Zn}_{1/3}\text{Nb}_{2/3})\text{O}_3\text{-PbTiO}_3$ (PZN-PT) have been dominating the defense and civilian applications for the past few decades [4,5].



For the reasons of environmental protection, there has been substantial research interest in exploring new lead-free piezoelectric or ferroelectric materials which can be used as alternatives to replace lead-based materials. Potassium sodium niobate ($\text{K}_{0.5}\text{Na}_{0.5}\text{NbO}_3$, abbreviated as KNN) ceramic has attracted considerable attention recently and has been considered one of the most promising alternatives to the lead-based piezoelectric ceramics. It possesses superior piezoelectric and ferroelectric properties, which are often ascribed to the presence of a polymorphic phase boundary (PPB) between two orthorhombic phases [3]. KNN has an orthorhombic crystal structure at room temperature and undergoes two phase transitions at high temperatures, i.e., the orthorhombic-tetragonal phase transition at T_{o-t} (200°C) and the tetragonal-cubic phase transition at T_c (Curie temperature, 420°C) [6]. For a well-sintered KNN ceramic prepared by hot-press sintering, it has a high T_c ($\sim 420^\circ\text{C}$), a large piezoelectric coefficient ($d_{33} \sim 160$ pC/N), a large electromechanical coupling coefficient ($k_p \sim 0.45$), and a high density ($\rho = 4.46$ g/cm³) [7,8]. However, because of the high volatility of alkaline elements at high temperatures, it is difficult to prepare well-sintered dense KNN ceramics under atmospheric conditions. For a KNN ceramic sintered by ordinary sintering, there is serious degradation in density ($\rho = 4.25$ g/cm³) and piezoelectric properties ($d_{33} \sim 80$ pC/N and $k_p \sim 0.36$) [7,8]. The piezoelectric properties of KNN are not as good as lead-based materials such as PZT. Therefore, there has been a lot of research works focused on improving the sinterability as well as piezoelectric properties of KNN, either by adding sintering aids such as CuO and MnO₂, doping with various ions such as Ag and Li, or the formation of solid solutions such as KNN-BaTiO₃ [9],



KNN-LiNbO₃ [10], KNN-SrTiO₃ [11] and KNN-LiTaO₃ [12]. Novel fabrication techniques such as template grain growth and spark plasma sintering have also been developed for improving the properties of KNN [13]. On the other hand, there are only a few works studying the applications of KNN-based ceramics [14].

1.3 Piezoelectricity and Ferroelectricity

1.3.1 Piezoelectricity

The direct piezoelectric effect was first demonstrated by Pierre Curie and his older brother Jacques Curie in Paris on 2nd August 1880 [15]. They reported the relationship between the applied mechanical load and induced electric charge. The effect was observed on certain types of crystals such as tourmaline, quartz, topaz, cane sugar, and Rochelle salt (sodium potassium tartrate tetrahydrate). Rochelle salt and quartz exhibited the strongest piezoelectric responses at that time. However, they did not predict the converse piezoelectric effect, which was deduced mathematically from thermodynamic principles by Gabriel Lippmann in 1881 [16].

When a mechanical stress is applied to a piezoelectric material, electrical charges that are proportional to the stress are generated. This effect is called the direct piezoelectric effect. Figure 1.1 shows the schematic diagrams illustrating the direct piezoelectric effect. On the other hand, when an electric field is applied to a



THE HONG KONG POLYTECHNIC UNIVERSITY

piezoelectric material, a change in dimensions is produced. This is called the converse piezoelectric effect. Both the effects have been observed not only in single crystals but also in polycrystalline materials such as PZT and barium titanate (BaTiO_3). Most of the piezoelectric materials have a perovskite ABO_3 crystal structure which is shown in Figure 1.2.

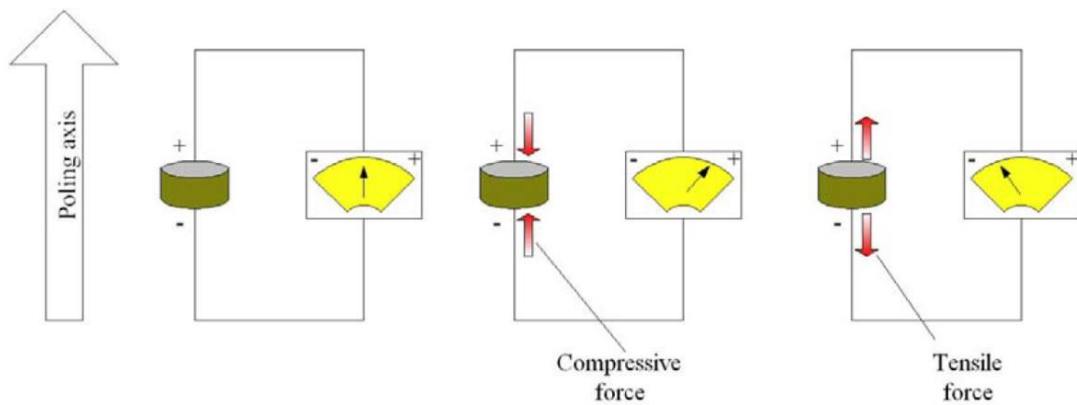


Figure 1.1 The direct piezoelectric effect.

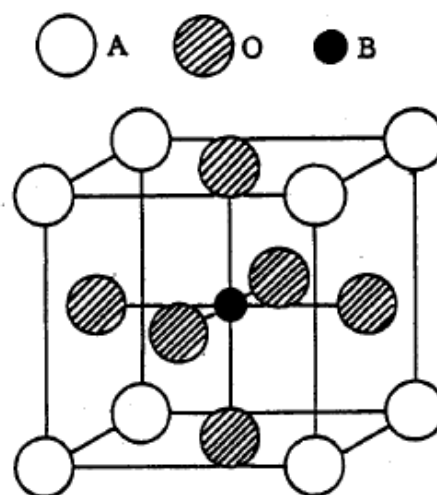


Figure 1.2 Perovskite crystal structure of ABO_3 .



The direct and converse piezoelectric effects can be described by the following equations:

$$D = dT \quad (1.1)$$

$$S = dE \quad (1.2)$$

where D is the electric displacement, T is the stress, E is the electric field, S is the strain, and d is the piezoelectric coefficient. The first equation describes the direct piezoelectric effect while the second equation describes the converse piezoelectric effect [17].

1.3.2 Ferroelectricity

Depending on the crystal structure, a material may exhibit simply dielectric properties, or together with piezoelectric, pyroelectric and ferroelectric properties. As demonstrated in Figure 1.3, piezoelectrics may not be ferroelectric, but ferroelectrics must be piezoelectric [3].

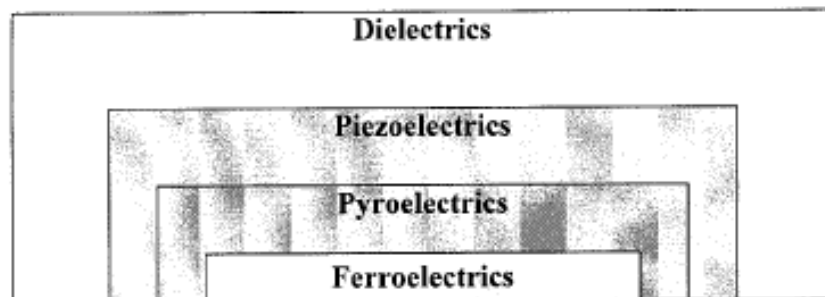


Figure 1.3 The relationship between dielectrics, piezoelectrics, pyroelectrics and ferroelectrics.

There are two major criteria for classifying a material as a ferroelectric: the



THE HONG KONG POLYTECHNIC UNIVERSITY

existence of a spontaneous polarization and the switching (or re-orientation) of the spontaneous polarization [18]. One of the typical features of ferroelectric materials is ferroelectric hysteresis that is generally manifested by a polarization hysteresis (P-E) loop, i.e., the polarization P is a double-valued function of the applied electric field E . A typical P-E loop for a ferroelectric (polycrystalline) material is shown in Figure 1.4.

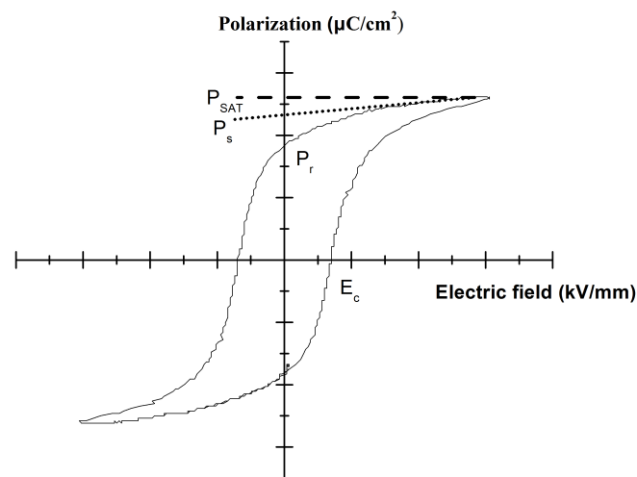


Figure 1.4 A typical ferroelectric hysteresis loop.

P is defined as the dipole moment per unit volume of the material. Under a high electric field, P reaches a maximum value that is called the saturated polarization P_{sat} . When the high electric field is decrease to zero, P has a value called the remanent polarization P_r , i.e. the net polarization remained in the materials. The electric field required to reduce the polarization to zero is called the coercive field E_c .

Another typical characteristic of ferroelectric materials is the ferroelectric-



paraelectric phase transition occurred at a temperature called the Curie temperature T_c . Above T_c , the material is in the paraelectric phase and possesses no spontaneous polarization. As the temperature decreases below T_c , the material transforms to the ferroelectric phase and the spontaneous polarization becomes non-zero. However, because of random orientation of domains (regions with uniformly aligned dipoles), the net polarization of polycrystalline ferroelectric materials is zero, and hence exhibiting no piezoelectric effect. To induce the piezoelectric effect, a high electric field has to be applied to align the dipoles to a single direction. This process is called poling. After poling, the material becomes piezoelectric and anisotropic.

1.3.3 KNN-based Piezoelectric Ceramics

Lead-based piezoelectric materials, such as PZT, have been widely used in various applications, such as sonars [19], transducers [20] and gyro-sensors [21]. As lead has a harmful impact on the global environment and human body [22], various countries including German and Japan have scheduled to weed out lead-containing products. There are hence great importance and need to develop lead-free piezoelectric materials and to explore the use of them in various applications for replacing the lead-based products. Potassium sodium niobate ($K_{0.5}Na_{0.5}NbO_3$) (abbreviated KNN) has been studied extensively and has been considered one of the most promising lead-free candidates.

Alkaline niobates became hot research topics at the end of the 1990s because of



THE HONG KONG POLYTECHNIC UNIVERSITY

the increased environmental awareness. Most of the research works were focused on potassium niobate (KNbO_3) and sodium niobate (NaNbO_3). It has been shown that, because of the morphotropic phase boundary (MPB), the solid solution of KNbO_3 and NaNbO_3 with a composition $\text{K/Na} = 50/50$, i.e., $\text{K}_{0.5}\text{Na}_{0.5}\text{NbO}_3$ or KNN, exhibits rather high electromechanical coupling coefficients [3,7,8,23]. KNbO_3 has a similar sequence of phase transitions as BaTiO_3 during cooling: cubic ($>435^\circ\text{C}$), tetragonal ($435 - 225^\circ\text{C}$), orthorhombic ($225 - -12^\circ\text{C}$), rhombohedral ($< -12^\circ\text{C}$). On the other hand, NaNbO_3 undergoes a more complicated sequence of phase transitions from a cubic phase above 630°C to an orthorhombic antiferroelectric phase at room temperature [3]. The phase diagram of the solid solution of KNbO_3 - NaNbO_3 is shown in Figure 1.5 [3].

As illustrated in Figure 1.5, KNN has a Curie temperature of $\sim 400^\circ\text{C}$. During cooling, it transforms to a tetragonal phase at $\sim 200^\circ\text{C}$ and then to an orthorhombic phase at about -160°C , below which it has a rhombohedral phase. The melting temperatures of KNbO_3 and NaNbO_3 are 1040°C and 1420°C , respectively. For KNN, the solidus and liquidus lines are at $\sim 1140^\circ\text{C}$ and $\sim 1280^\circ\text{C}$, respectively.

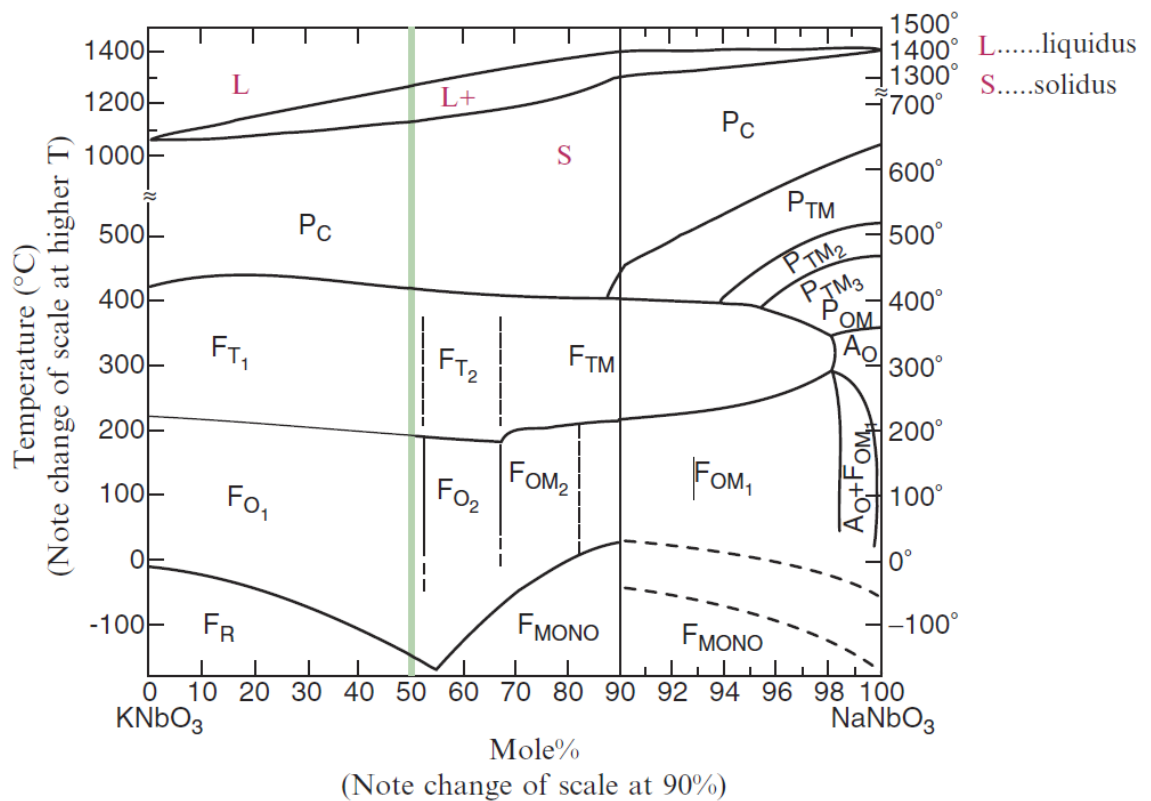


Figure 1.5 Phase diagram of the system $\text{KNbO}_3\text{-NaNbO}_3$ [3].

Because of the volatilization of alkaline elements at high temperatures, it is very difficult to obtain dense and stoichiometric KNN ceramics using conventional sintering method. Therefore, early investigations on KNN were focused on enhancing its sinterability and then piezoelectric properties. Hot pressing is a solution to produce dense KNN ceramics in early days, and then the spark plasma sintering (SPS) method became an alternative. Table 1.1 compares the properties of KNN ceramics fabricated by different methods. It can be seen that dense samples fabricated by hot-pressing or SPS have better piezoelectric properties than the one sintered in air (i.e., the conventional method).



Table 1.1 Characteristic of KNN ceramics with different preparation methods.

	Air-fired [7]	Hot-press sintered [7]	SPS [13]	Attrition-milling [24]
Relative permittivity ϵ_r	290 (100 kHz)	420 (100 kHz)	606 (1 kHz)	605 (1 kHz)
Dielectric loss $\tan\delta$ (%)	2 (100 kHz)	1.4 (100 kHz)	3.6 (1 kHz)	4.36 (1 kHz)
Density (g/cm^3)	4.25	4.46	4.47	4.44
d_{33} (pC/N)	~80	160	148	102
k_p	0.36	0.45	0.39	0.38

As the sintering conditions for obtaining dense KNN ceramics are very critical, the repeatability is generally low. Sintering aids and dopants have hence been added to broaden the sintering window of KNN ceramics for improving its sinterability, dielectric and piezoelectric properties. A number of works have also been carried out to form new solid solutions of KNN with other ABO_3 perovskites, e.g., KNN- SrTiO_3 [25], KNN- BaTiO_3 [26], KNN- LiTaO_3 [12], and KNN- LiNbO_3 [10], for improving the properties of KNN ceramics. Table 1.2 summarizes the results of some KNN-based solid solutions. For the best composition of each solid solution, the dielectric loss ($\tan\delta$) decreases from over 6% (at 10 kHz) to about 4%.

Table 1.2 Summary of the properties of KNN doped with different materials by Guo *et al.*

Chemical formula	Best composition	d_{33} (pC/N)	k_t	k_p	$\tan\delta$ (%)
Pure KNN	-	98	0.38	0.295	6.8
(1-x) KNN – x SrTiO ₃	x = 0.005	96	0.438	0.325	2.9
(1-x) KNN – x BaTiO ₃	x = 0.02	104	0.38	0.29	~4
(1-x) KNN – x LiTaO ₃	x = 0.05	~200	-	~0.36	~5
(1-x) KNN – x LiNbO ₃	x = 0.06	~235	0.48	0.42	~4

(1-x)K_{0.47}Na_{0.47}Li_{0.06}NbO₃-xNaSbO₃ is one of the KNN-based solid solutions which has been recently developed and studied extensively [14]. The ceramics with excellent piezoelectric properties can be fabricated by a conventional sintering process in air. The substitution of Li⁺ for K⁺ and Na⁺ in the A site of the KNN lattices can decrease the sintering temperature and thus improve the sinterability of the ceramics [27]. Although NaSbO₃ has an ABO₃-type ilmenite structure [28], it can diffuse into the KNN lattices to form a new solid solution. It has been shown that coexistence of the orthorhombic and tetragonal phases is formed in the ceramics with x = 0.04 – 0.10 at room temperature. Owing to the more possible polarization states, the piezoelectric properties of the ceramics are improved. The ceramics with x = 0.09, i.e., 0.91K_{0.47}Na_{0.47}Li_{0.06}NbO₃-0.09NaSbO₃ (abbreviated as KNLN-NS) exhibits the optimum piezoelectric properties, giving a piezoelectric coefficient d_{33} of 305 pC/N, electromechanical coupling coefficients k_p and k_t of 0.51. Because of the high



electromechanical coupling coefficients, the KNLN-NS ceramics have been used to fabricate transducers and good performance has been obtained [14]. Because of the good piezoelectric properties as well as the good performance in transducer applications, KNLN-NS ceramics are chosen in this project as the base compositions for the fabrication of gyro-sensors. As compared with PZT, the KNLN-NS ceramics offer an advantage of lead-free which is environmental friendly. Table 1.3 lists the properties of the KNLN-NS and PZT ceramics for comparison.

Table 1.3 Piezoelectric properties of KNLN-NS and PZT.

	KNLN-NS	PZT-8 Navy III [29]
Curie Temperature T_c ($^{\circ}\text{C}$)	~ 320	300
Relative permittivity ϵ_r (at 1 kHz)	1502	1100
Piezoelectric coefficient d_{33} (pC/N)	305	300
Electromechanical coupling coefficient k_p	0.51	0.51
Electromechanical coupling coefficient k_t	0.51	0.46

1.4 Low-temperature Sintering Techniques

Owing to the easy evaporation of K and Na during high-temperature sintering, compositional control is a common challenge for fabricating KNN-based ceramics, including KNLN-NS. The defects induced by the volatilization of K and Na may decrease piezoelectric properties of the ceramics. A low sintering temperature is hence desired for suppressing the volatilization of these alkaline elements and then improving the piezoelectric properties as well as reproducibility. Furthermore, it also provides a benefit for fabricating multilayered piezoelectric components, such as gyro-sensors.



THE HONG KONG POLYTECHNIC UNIVERSITY

Internal metal electrodes are generally co-fired with the multilayered piezoelectric structures at high temperatures. Therefore, a low sintering temperature such as 1000°C allows the use of relatively cheap inner electrodes such as Pd/Ag rather than Pt.

Low temperature sintering is very important for commercial production of electronic ceramics, especially multilayered devices [30,31]. Ferroelectric ceramics with fine grain structures exhibit superior mechanical properties and thus they have drawn much attention in potential applications, such as piezoelectric sensors and actuators [32,33]. Low-temperature sintered ceramics are also widely applied for multilayer capacitors, piezoelectric transducers, packaging materials for integrated circuits, high voltage insulators and chemical sensors [34,35,36,37,38]. Ferroelectric ceramics with dense and homogeneous microstructure as well as well-developed grains of uniform size are desired for practical applications. In general, a high temperature is required for sintering the ceramics to achieve such an ideal microstructure. Expensive inner metal electrodes such as Pt are hence needed for preparing multilayered components by the conventional sintering processes. Apparently, for saving cost as well as energy, there is great interest to develop low-temperature sintered ceramics.

Metal oxides and carbonates are conventionally used as the starting materials in solid-state reaction process to prepare the precursor powders for fabricating piezoelectric ceramics. Due to the relatively large and non-uniform particle size of the starting materials, the resulting precursor powders are also large and non-uniform in size. Accordingly, a high sintering temperature is required for obtaining dense ceramics



[39,40,41]. For KNN-based ceramics, due to high volatilities, the alkaline metals will very likely evaporate during the sintering at high temperatures, and thus degrading the electrical properties. One of the approaches to reduce the sintering temperature is to use precursor powders with small and uniform particle size. For this purpose, submicron as well as nanosized precursor powders have been synthesized by various methods, such as wet-chemical co-precipitation method [42,43], sol-gel process [44,45] and hydrothermal synthesis [46,47]. Although significant progresses have been achieved, there are some drawbacks. For example, those methods are expensive and extremely sensitive to the environmental conditions such as moisture, light and heat [48]. Therefore there is a need to develop effective and inexpensive processing techniques to reduce the sintering temperature.

1.4.1 High Energy Ball Milling

High-energy ball milling (HEBM), which is also known as mechanical alloying, was invented for developing dispersion-strengthened high-temperature alloys. The technique has then been successfully extended to synthesize various materials, such as nanocrystalline oxide powders [49], solid state solutions of ceramics [50], nanoparticles of $\text{YBa}_2\text{Cu}_3\text{O}_{7-\delta}$ superconductor [51], Ni-Zn and barium ferrites [52], and lead titanate powders [47]. The most important advantage of HEBM is that it can synthesize designed compounds with grain size in the nanometer scale at room temperature. This is especially important for handling elements that have high volatilities at elevated temperatures, such as lead and alkaline metals. The high volatility will cause the



THE HONG KONG POLYTECHNIC UNIVERSITY

composition of the designed materials to deviate from its stoichiometry. It has always been a concern for the preparation of materials containing such elements.

Among various preparation methods, HEBM is simple and efficient for preparing nanometer powders. It is also an easy and inexpensive method for producing nanostructured materials in bulk quantities. After the HEBM process, the sintering kinetics of the starting powders is enhanced effectively [53]. Desu *et al.* studied the effects of mechanical milling on the formation of lead titanate (PT) from oxides [54]. They showed that the kinetic energy for forming PT compound from a mixture of PbO/TiO₂ decreased from 152 to 110 kJ/mol after milling the mixture for 30 min. This was suggested to be due to the reduced phase formation temperature arisen from the nanometer particle size and very high homogeneity [55]. Furthermore, compared with soft chemical methods [56], HEBM is suitable for mass production. As the process takes place in well-sealed vials at room temperature, the loss of volatile elements is reduced effectively. Although the method is practically very simple, it is a complex process which depends on a number of factors, e.g., physical and chemical parameters such as the precise dynamic conditions, temperature and nature of the grinding tools [57,58]. For most of the compounds prepared by the technique, various processing conditions such as the ball to powder weight ratio (BPR), milling speed and milling type have been studied and shown to have significant effects on the final product [59].

HEBM technique has been used to prepare various ferroelectric ceramics, such as BaTiO₃ [60], Pb(Zr_{0.53}Ti_{0.47})O₃ [61], PbTiO₃ [62]. In general, it can successfully



THE HONG KONG POLYTECHNIC UNIVERSITY

increase the sinterability of the calcined powders. Leyt-Ruiz *et al.* [48] reported that the sintering temperature of PZT could be effectively decreased by 100°C using the HEBM technique. In their study, PbO, ZrO₂ and TiO₂ were first mixed by conventional ball milling and calcined to form PZT powders. The calcined PZT powders were then subjected to high-energy ball milling. A zirconium vial and zirconium balls of diameter 3 mm were used as milling media and the ball to powder ratio was 15. The milling speed was 400 rpm, and the milling was stopped for 5 min after every 60 min to avoid overheating. After a total milling time of 80 h, the particles size decreased from ~75 nm to ~35 nm and the sintering temperature was hence decreased.

Cheng *et al.* [63] reported that the sintering temperature of Mg₂SiO₄ were successfully reduced by 300°C using HEBM as compared with the conventional solid state reaction process. In their study, a mixture of MgO and SiO₂ was high-energy ball milled for 30 h in air. Tungsten carbide vial with a diameter of 80 mm and tungsten carbide balls of diameter 10 mm were used as milling media. The rotational speed of the vials was 300 rpm, while the ball-to-powder-to-deionized water ratio was 20:1:5. The average particle size of the calcined powders was decreased from ~1100 nm to ~150 nm and the sintering temperature was decreased to 1075°C. The ceramics possessed a dense microstructure and exhibited excellent microwave dielectric properties, which were comparable to those of the ceramics sintered at 1350-1550°C using a conventional solid state reaction method.



Owing to the advantages of reducing the sintering kinetic energy and producing uniform and nano-sized powders, HEBM is used in this work to prepare KNLN-NS ceramics. It is expected that, by applying HSBM, the sintering temperature can be lowered, the grain size can be reduced and the homogeneity can be improved.

1.4.2 Sintering Aids

In general, the sintering temperature of ceramics can be reduced by utilizing sintering aids with low melting temperatures such as glasses and oxides. However, it has been shown that electrical properties of the ceramics are commonly deteriorated by the low-temperature sintering. So, it becomes very important in selecting a suitable sintering aid [64].

Li *et al.* [65] reported that the sintering temperature of $(\text{K}_{0.49}\text{Na}_{0.51})_{0.98}\text{Li}_{0.02}(\text{Nb}_{0.77}\text{Ta}_{0.18}\text{Sb}_{0.05})\text{O}_3+0.5 \text{ mol}\% \text{BaZrO}_3$ ceramics could be reduced from 1150°C to 1100°C using the $\text{BaO-CuO-B}_2\text{O}_3\text{-MnO}_2$ (BCBM) frit as a sintering aid. 1.0 wt% BCBM frit was effective in increasing the bulk density, promoting densification, as well as suppressing the volatilization of K and Na under a low sintering temperature. Besides the good piezoelectric properties, the dielectric loss of the ceramics was also reduced and the mechanical quality factor was increased, giving: $d_{33} = 345 \text{ pC/N}$ and $k_p = 44.5 \%$.



MnO₂ had also been used as a sintering aid to reduce the sintering temperature of KNN ceramics from 1150°C to 1100°C [66]. After the addition of MnO, the grain size was reduced, and a more homogeneous distribution in grain size was obtained. This was suggested to be attributed to the low melting temperature of MnO₂, which could effectively lower the sintering temperature and then suppress the abnormal grain growth near the original melting temperature (~1140°C) of KNN ceramics [67].

Bencan *et al.* [68] reported that alkaline germanate (K,Na-germanate) with a melting temperature near 700°C could be used as a novel sintering aid for KNN ceramics to reduce the sintering temperature by 100°C, to about 1000°C. The sintering aid not only improved the densification (95.6%TD) but also retained the good piezoelectric properties of KNN.

Sasaki *et al.* [69] reported that LiBO₂ could effectively decrease the sintering temperature of (Li_{0.04}K_{0.52}Na_{0.44})(Nb_{0.84}Ta_{0.1}Sb_{0.06})O₃ ceramics to 950°C, which was lower than the melting temperature of Ag (961 °C). For the ceramic added with 3 wt% LiBO₂, the relative density reached a high value of 95%TD. However, the piezoelectric coefficient (d_{33}) decreased severely from 225 pC/N to 93 pC/N. In order to mitigate the degradation of the piezoelectric properties, excess Na was added together with LiBO₂ to restrict the incorporation of Li ions into the lattices. The piezoelectric coefficient was then increased to 138 pC/N, while the sintering temperature was remained unchanged at 950°C.



THE HONG KONG POLYTECHNIC UNIVERSITY

Besides KNN-based ceramics, sintering aids have also been developed for lowering the sintering temperatures of other ferroelectric materials. Hayashi *et al.* [70] reported that lithium bismuth oxide (LiBiO_2) with a melting temperature of 700°C was effective in lowering the sintering temperature of $(\text{Pb}_{0.86}\text{Ba}_{0.04}\text{Sr}_{0.12})(\text{Zr}_{0.56}\text{Ti}_{0.44}\text{Sb}_{0.02})\text{O}_3$. For the ceramics added with 1wt% LiBiO_2 , the sintering temperature was effectively reduced by about 200°C , while the dielectric and piezoelectric properties were improved and became superior to those of the ceramics without the sintering aids.

Hasegawa and Otagiri [64] reported that copper bismuth oxide (CuBi_2O_4) with a melting temperature of 600°C was effective in lowering the sintering temperature of BaTiO_3 . Pure BaTiO_3 ceramics could not be fully densified at a sintering temperature lower than 1300°C . After the addition of 6.0 wt% CuBiO_4 , the ceramics could be well-sintered to a high density of 5.95 g/cm^3 at a low sintering temperature of 920°C .

Wong *et al.* [71] reported that a complex of Cu/Ba (in a molar ratio of 71.5/28.5) with a eutectic temperature of 890°C was effective in lowering the sintering temperature of $\text{CaBi}_4\text{Ti}_4\text{O}_{15}$. They showed that the Cu/Ba complex could promote the sintering of the $\text{CaBi}_4\text{Ti}_4\text{O}_{15}$ ceramics at a low temperature of 990°C , which is 210°C lower than that for the ceramics without the sintering complex (1200°C). Moreover, the dielectric and piezoelectric properties were remained almost unchanged or even slightly improved as compare with the ceramics without the sintering complex.



In this project, the Cu/Ba complex is used as a sintering aid for reducing the sintering temperature of the KNLN-NS ceramics. The Cu/Ba complex possesses a low eutectic temperature of 890°C which can provide a liquid phase for promoting the sintering of the KNLN-NS ceramics.

1.5 Gyro-sensors

The applications of gyro-sensors have been expanded beyond the traditional fields of transportation and spacecraft to the new growing fields of portable consumer electronics. Miniaturized gyro-sensors with good sensitivity are longed for wide applications, in particular for consumer electronic applications. Gyro-sensors provide a means for measuring angular rate or angle on rotatable systems. They can be used to transform a physical rotation into electrical signals that can be analyzed for controlling the position of a system or a user.

There are two types of gyro-sensors: macroscopic and microscopic gyro-sensors. In the early days, the volume of gyro-sensors is generally large, which are the so-called macroscopic gyro-sensors. For examples, ring laser gyro-sensors and ball electrostatic gyro-sensors are macroscopic gyro-sensors. The sensitivity of macroscopic gyro-sensors is generally high, but the portability is poor because of the large volume. Microscopic gyro-sensors are the devices combining gyro-sensor technologies with MEMS technologies [72]. In the past few decades from the invention of silicon vibrating micro-gyro-sensors, the micro-gyro-sensor technology has advanced quickly. Particularly,



micro-gyro-sensors have advantages on their size miniaturization, low fabrication cost and low power consumption in applications such as consumer electronics and defense.

Micro-gyro-sensors are widely used in automotive applications, such as anti-rollover systems [73], antiskid control [74] and electronic stability. They are also applied in a number of consumer applications, such as camera stabilization, cell phone stabilization, virtual reality (e.g., head-mounted displays [75]), inertial mouse and navigation for portable electronics. Furthermore, attitude control systems comprising inertial sensors and gyro-sensors are commonly used in robotics applications [76]. Micro-gyro-sensors are also adopted in military applications such as GPS, aeronautics and astronautics, missiles navigation, stable platform, etc.

1.5.1 Coriolis Effect

All the micro electro-mechanical system (MEMS) gyroscopes take advantage of the Coriolis effect. In a reference frame rotating at angular velocity Ω , a mass M moving with velocity v experiences a force F :

$$F = -2Mv \times \Omega \quad (1.5)$$

As the Coriolis force F is perpendicular to both v and Ω , it only changes the motion direction of the mass, but does not change the speed of the motion, i.e. it does not do work on the moving mass [77,78]. As shown in Figure 1.6, a mass vibrates at the driving mode in the x -direction. If a rotation about the z -axis is applied on it, a Coriolis force is induced, exciting a vibration of the mass in the y -direction. Depending on



THE HONG KONG POLYTECHNIC UNIVERSITY

different systems, the induced vibration in the y-direction will generate an electrical signal (i.e., output signal) that is proportional to the rotation speed and then can be used for controlling the position of the system.

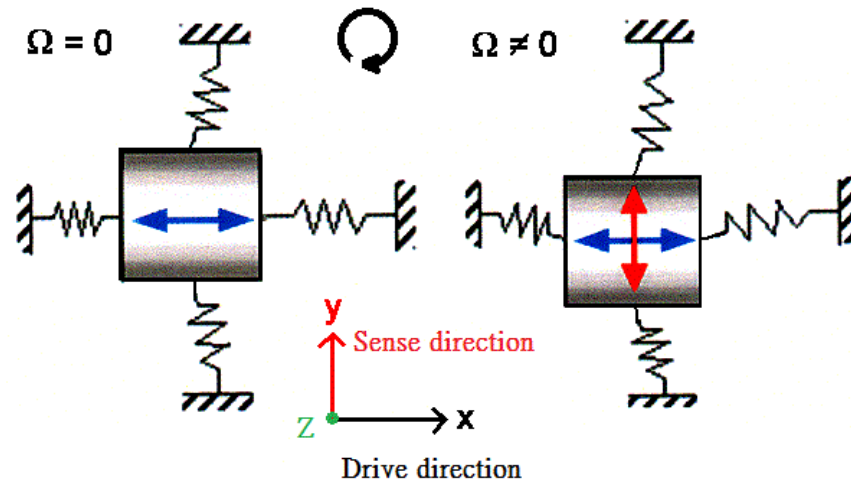


Figure 1.6 Coriolis effect on vibrating object.

1.5.2 Piezoelectric Vibratory Gyro-sensors

Gyro-sensors [79,80] can be fabricated using piezoelectric materials. They can be applied in motion control of vehicles, consumer electronics, moving equipment, machine parts, and weapon systems. Piezoelectric gyro-sensors utilize two vibration modes of a vibrating piezoelectric body. The directions of the two vibration modes are perpendicular to each other. One of the two modes is excited into vibration (driving mode) by an applied alternating voltage based on the converse piezoelectric effect. If the vibrating gyro-sensor is rotated about an axis that is normal to the two modes, a Coriolis force is induced, exciting the other mode in vibration (sensing mode). According to the direct piezoelectric effect, an alternating voltage (output voltage) that



is proportional to the rotation speed is generated. The working principle is similar to that illustrated in Figure 1.6. The resonance frequencies of the two modes should be very close to each other for achieving a maximum sensitivity. Examples of piezoelectric vibratory gyro-sensors include tuning forks [81], flexural vibration in two perpendicular directions of beams [82,83,84,85,86], thickness-shear vibration in two perpendicular directions of plate [87,88,89], and radial and torsional vibrations of circular cylindrical shells [90]. Degenerate modes of rings, shells, and circular disks have also been used to make gyro-sensors [91,92,93,94,95].

1.5.2.1 Tuning Fork Gyro-sensor

A tuning fork gyro-sensor consists of two bimorph piezoceramic beams of square cross-section connected by a non-active elastic half-ring as shown in Figure 1.7. Both the bimorph beams and the half-ring have the same mechanical properties. The remanent polarization of the driving arm (on the right in Figure 1.7) is along the x -axis while the remanent polarization of the sensing arm (on the left in Figure 1.7) is along the y -axis. Thin electrodes (black area in Figure 1.6) are deposited on the two side surfaces of the driving arm and the top and bottom surfaces of the sensing arm [81]. The driving arm is electrically driven to vibrate at its bending resonance frequency along the x -axis. When the sensor is rotated about the z -axis, a Coriolis force is induced, bending the sensing arm in a direction normal to both the driving and rotation directions (y -axis). The induced bending is used to generate the electrical signal by the direct piezoelectric effect. This type of gyro-sensors has simple electrode patterns, and the



output signal is large. However the fabrication of this gyro-sensor, in particular the half-ring, is difficult.

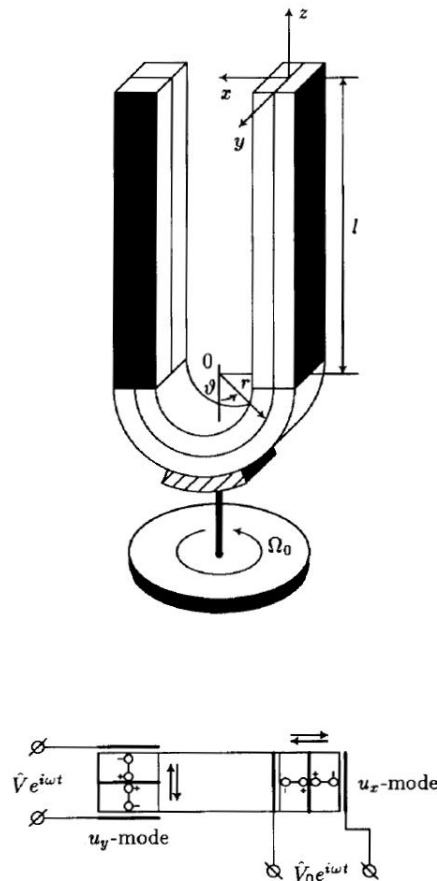


Figure 1.7 The Schematic diagram of tuning fork gyro-sensor [81].

1.5.2.2 Thickness-shear Plate Gyro-sensor

A thickness-shear plate gyro-sensor is comprised of a rectangular ceramic plate poled in the thickness direction as shown in Figure 1.8. The plate can vibrate at two thickness shear modes that can be excited or detected by lateral electrodes on the sides $X_1 = \pm a$ or $X_3 = \pm c$ of the plate [88]. Similarly, one of the thickness-shear modes is electrically driven to vibrate (driving mode) based on the converse piezoelectric effect, while the other is excited by the Coriolis force induced by a rotation about the X_2 -axis.



Based on the direct piezoelectric, the induced vibration generates an electrical signal (output signal). Although this type of gyro-sensors has a simpler structure, the output signal is very weak and of high-frequency, making the peripheral electronics become demanding.

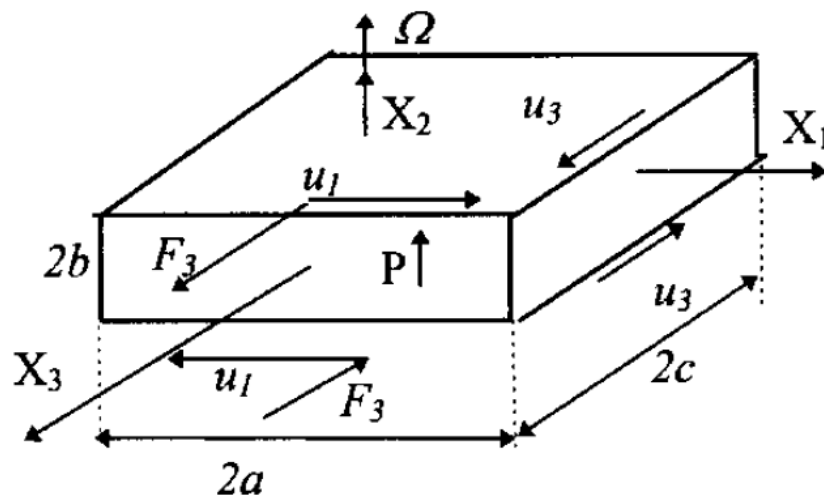


Figure 1.8 The Schematic diagram of thickness-shear plate gyro-sensor [88].

1.5.2.3 Circular Cylindrical Shell Gyro-sensor

A typical circular cylindrical shell gyro-sensor is shown in Figure 1.9. The upper part of the gyro-sensor is served as the driving and is poled in the wall-thickness direction. Electrodes are deposited on the inner and outer cylindrical surfaces. The lower part of the gyro-sensor is served as the sensing part and is poled in the circumferential direction. One of the sensing electrodes is deposited on the bottom surface, while the other is deposited on the interface between the two parts or is shared



THE HONG KONG POLYTECHNIC UNIVERSITY

with one of the driving electrodes of the upper part [96]. The circular cylindrical shell gyro-sensor is electrically driven to vibrate at its resonance frequency (Figure 1.10b). When the vibrating cylindrical shell is rotated about the z -axis, a Coriolis force is induced, driving it into a torsional motion (Figure 1.10a). The induced torsional motion is used to generate an electrical signal by the direct piezoelectric effect. This type of gyro-sensors has the hollow structure which can enhance the torsional motion for sensing. However the size of this gyro-sensor is relatively bulky and the fabrication involves more and complicated processes, such as etching and polishing.

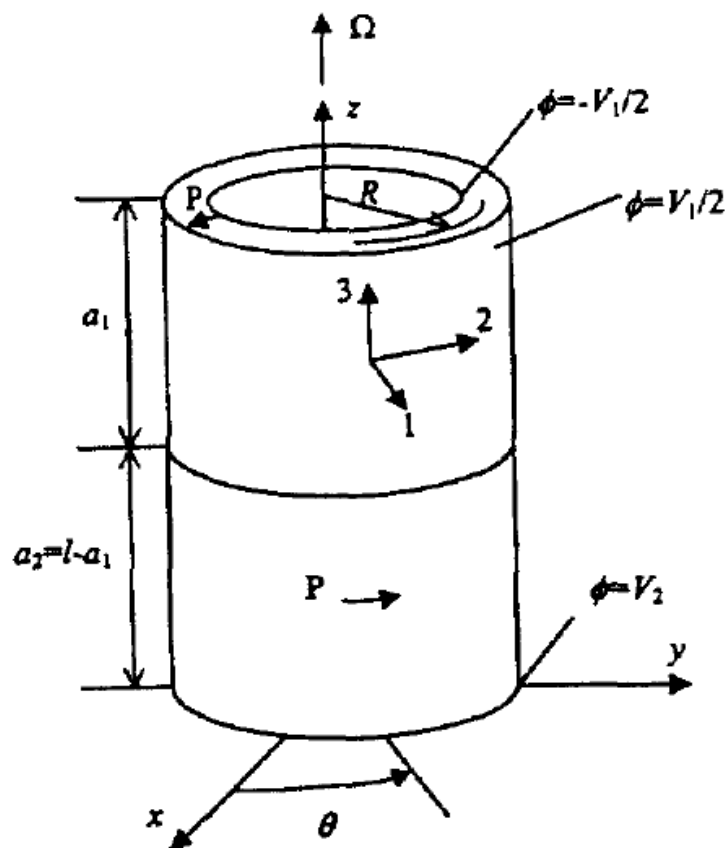


Figure 1.9 The Schematic diagram of circular cylindrical shell gyro-sensor [96].

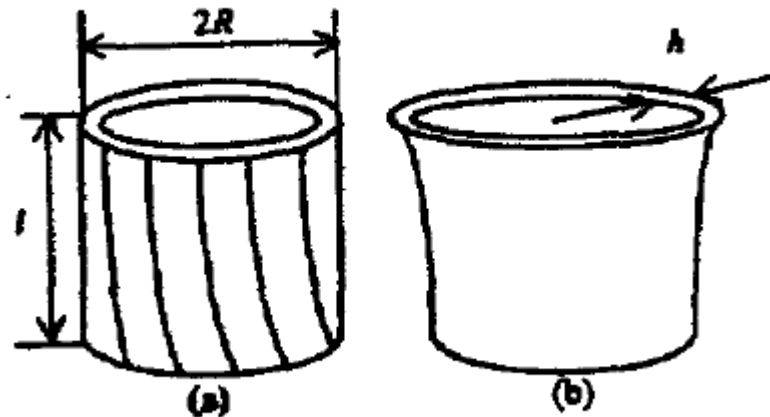


Figure 1.10 Vibration modes of circular cylindrical shell gyro-sensor: (a) sensing mode, (b) driving mode [96].

1.5.2.4 Ring Gyro-sensor

A schematic diagram of a ring gyro-sensor is shown in Figure 1.11. It is comprised of a piezoelectric ring poled in the z direction. Eight pairs of identical electrodes are deposited on the top and bottom surfaces of the ring. As illustrated in Figure 1.11, an input or driving voltage V_1 is applied to four pairs of the electrodes, while an output or sensing V_2 is expected to be detected at the four pairs of electrodes [96]. The ring gyro-sensor is electrically driven (applying V_1) to vibrate at its resonance frequency along x -axis (primary mode in Figure 1.12). When the vibrating ring is rotated about z -axis, a Coriolis force is induced, exciting the sensing mode (secondary mode in Figure 1.12). The induced vibration is used to generate an electrical signal (V_2) by the direct piezoelectric effect. The ring structure of this type of gyro-sensors can



THE HONG KONG POLYTECHNIC UNIVERSITY

enhance the vibration amplitude and the output signal. But the fabrication of the ring structure is difficult and the deposition of the electrodes is relatively complicated.

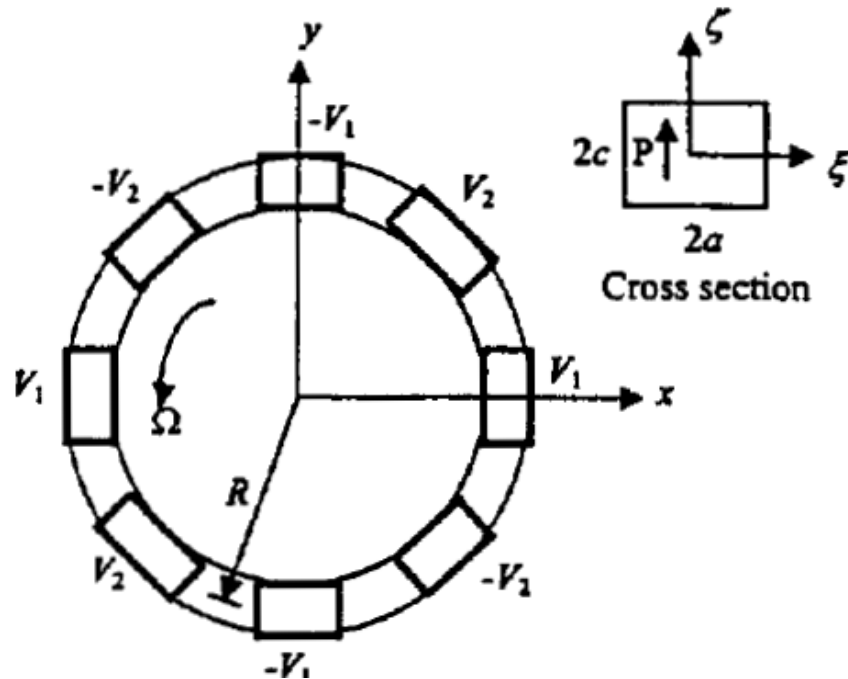


Figure 1.11 The Schematic diagram of a ring gyro-sensor [96].

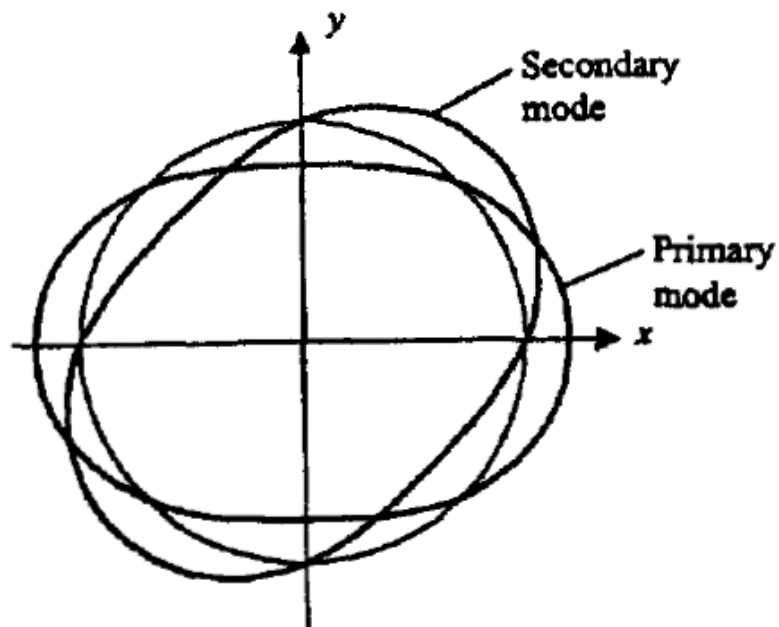


Figure 1.12 The vibration modes of a ring gyro-sensor [96].



1.5.2.5 Bimorph-type (beam-type) Gyro-sensor

The simplest structure of piezoelectric vibratory gyro-sensors is the beams type structure as it does not involve any curved structure. The gyro-sensor simply consists of two piezoelectric plates that are poled in opposite directions as shown in Figure 1.13. This is also called a bimorph beam [86] which can also be made of two different piezoelectric materials. As shown in Figure 1.13, the top electrode is divided into two parts. When an electric field is applied along the z-axis, the two ceramic plates deform differently, e.g. the top one contracts along the x-axis while the bottom one expands because of the Poisson effects, and thus leading to a upward bending. Therefore, if an alternating voltage is applied, the beam will vibrate in the z-direction (driving mode). When the vibrating beam is rotated about the x-axis, a Coriolis force is induced, exciting the beam to vibrate in the y-direction (sensing mode). When the beam is induced to vibrate in the y-direction, the two sides of the beam have different deformations, e.g. the left side contracts along the x-axis while the right side expands. Because of Poisson effect, the left side expands along the z-axis and the right side contracts. The charges induced on both sides by the direct piezoelectric effect are then different, leading to a difference in the currents passing through the two sides. By comparing the currents passing through the two sides, an output signal that is proportional to the rotation speed is obtained.

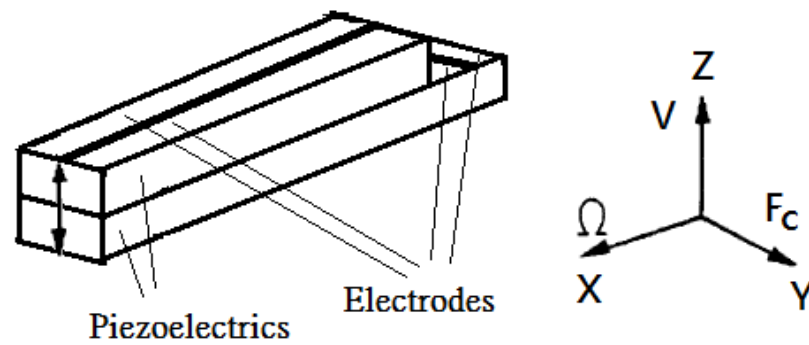


Figure 1.13 The schematic diagram of bimorph beam gyro-sensor.

Because of the simple structure and easy fabrication, bimorph-type gyro-sensors are fabricated using the lead-free piezoelectric ceramics in this project. The performance of the gyro-sensors is evaluated.



1.6 Scope of Work

The main objectives of the present work are to prepare low-temperature sintered lead-free piezoelectric ceramics and to fabricate piezoelectric vibratory gyro-sensors using the lead-free piezoelectric ceramics.

In Chapter 2, the fabrication processes for piezoelectric lead-free ceramics and bimorph-type piezoelectric vibratory gyro-sensors are presented.

In Chapter 3, characterizations of the piezoelectric lead-free ceramics are presented.

In Chapter 4, the fabrication and characterizations of bimorph-type piezoelectric vibratory gyro-sensors are presented.

In Chapter 5, summary of the major findings in this project is given.



Chapter 2 Fabrication of Piezoelectric Ceramics and Piezoelectric Gyro-sensors

2.1 Introduction

In this project, modified potassium sodium niobate ceramics $0.91\text{K}_{0.47}\text{Na}_{0.47}\text{Li}_{0.06}\text{NbO}_3-0.09\text{NaSbO}_3$ (KNLN-NS) are prepared by conventional solid-state sintering method. Two approaches: high-energy ball milling (HEBM) or sintering aids, are studied for lowering the sintering temperature of the ceramics. The ceramics are then used for fabricating bimorph-type piezoelectric vibratory gyro-sensors. In this chapter, the fabrication processes for the KNLN-NS ceramics and gyro-sensors are presented.

2.2 Fabrication of Piezoelectric Ceramics

Figure 2.1 shows the flow chart for the preparation of the KNLN-NS ceramics. Two ball milling techniques: conventional and high-energy, are used to treat the powders. Sintering aids for lowering the sintering temperature are used for some ceramics.

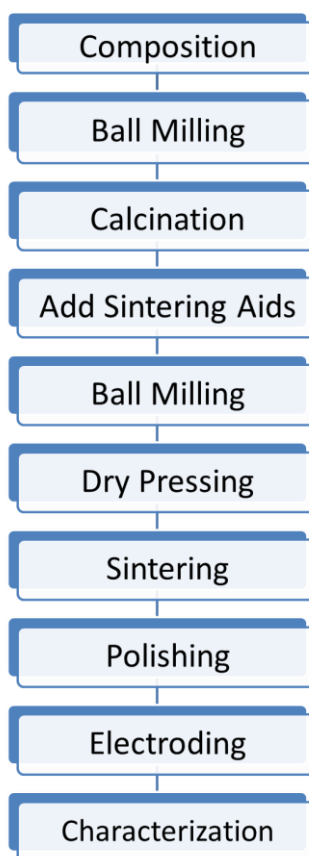


Figure 2.1 Flow chat for fabrication of piezoelectric ceramics.

2.2.1 Ball Milling and High-energy Ball Milling

Analytical-grade carbonate and metal oxide powders: K_2CO_3 (99%), Na_2CO_3 (99%), Li_2CO_3 (99%), Nb_2O_5 (99.99%) and Sb_2O_3 (99%) were used in this project. The powders were weighted in the stoichiometric ratio of the composition. After mixing and grounding roughly, the powder mixture was ready for ball milling.



2.2.2.1 Conventional Ball Milling

Ball milling is a process for grinding materials into fine powders. As shown in Figure 2.2, a vial that is partially filled with the materials to be ground and the grinding media rotates about an axis. For conventional ball milling (CBM), zirconia balls and ethanol are used as the grinding media, and the rotation speed is relatively slow. So, it generally takes longer time for CBM to obtain fine powders. In this project, the powder mixture prepared in Section 2.2.1 was ball-milled, using zirconia balls and ethanol as the grinding media, at a speed of 60 rpm for 8 h.

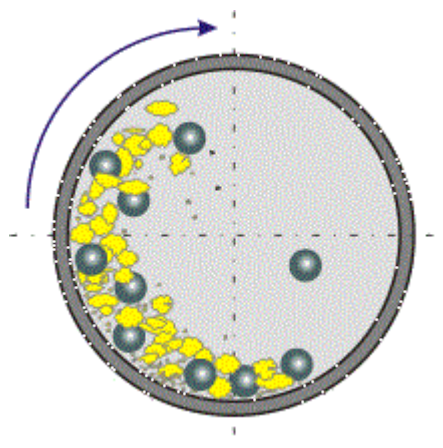


Figure 2.2 Schematic diagram showing the ball milling.



2.2.2.2 High-energy Ball Milling

Apart from conventional ball milling, the high-energy ball milling (HEBM) technique is also widely used to prepare ceramics. The major differences between the two techniques are the grinding media and rotation (/milling) speed. Tungsten carbide balls and vials are used in HEBM, while zirconia balls and plastic vials are commonly used for CBM. The rotation speed for HEBM is much higher than that for CBM, so that it usually takes shorter time for HEBM to obtain fine powders.

In this project, HEBM was carried out using a Fritsch Pulverisette 5 planetary mill. A tungsten carbide vial and tungsten carbide balls of diameters 10 mm and 20 mm were used as the milling media. The ball to powder ratio is 10:1 by weight. The milling speed was 200 rpm. The milling process was stopped for 10 min after every 30 min of milling to avoid overheating. The total milling time was 2 h.

2.2.2 Calcination

Calcination is a high-temperature solid state chemical reaction for decomposing the carbonates to the oxides and forming the perovskite structure of the compounds. In this project, the ball-milled powders, after drying, were calcined at 800°C for 6 h.



2.2.3 Sintering Aids

For the second approach, i.e., lowering the sintering temperature by sintering aids, a complex of Cu/Ba (in a molar ratio of 71.5/28.5) was used as the sintering aid. It was prepared from analytical-grade CuO (99%) and BaCO₃ (99.5%), and was added to the mixture after the calcination. The weight percentages (wt%) of the sintering aid studied in this project were 1.25, 2.5, 3.75 and 5.00, which corresponded to about 0.5 mol%, 1.0 mol%, 1.5 mol% and 2.0 mol%, respectively. The mixture of the calcined KNLN-NS powders and Cu/Ba sintering aid were then ball-milled again, either by CBM or HEBM.

2.2.4 Dry Pressing

The calcined powders (together with the Cu/Ba sintering aid for the second approach) prepared in previous procedures were dried and further mixed thoroughly with a polyvinyl alcohol (PVA) binder solution (5 wt%) manually using a pair of mortar and pestle. The weight ratio of powders to PVA solution is 10:3. The mixture was then dried and sieved using an 80-mesh screen. After that, the ceramic powders were put into a mold as shown in Figure 2.3 for dry-pressing.

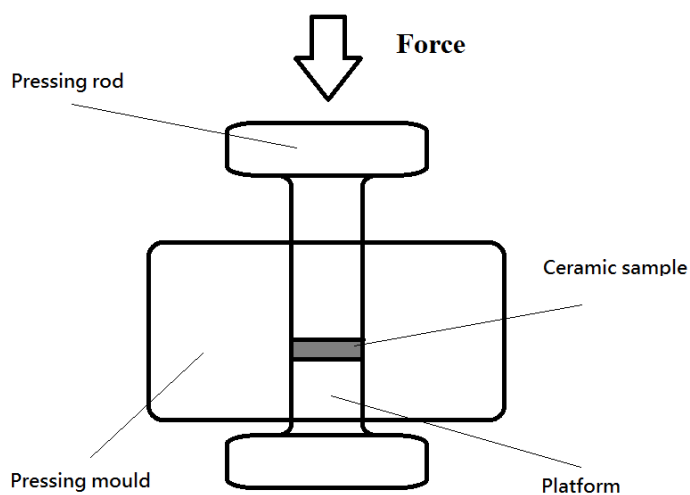


Figure 2.3 Schematic diagram of the dry pressing of ceramic disk.

In this project, a uniaxial pressure of ~ 440 MPa was applied for several minutes to remove the air trapped inside and compact the powders into a disk shape.

2.2.5 Binder Removal and Sintering

Heat treatment is an essential and important process in fabricating ceramics and it is usually carried out in a computer controlled furnace. The PVA binder in the pressed disk samples should be removed before sintering. In this project, the PVA binder was burnt out at 800°C for 2 hours in a programmable Carbolite furnace. During the binder removal, the samples were placed on an alumina plate without cover (Figure 2.4). The temperature profile for the process is shown in Figure 2.5.

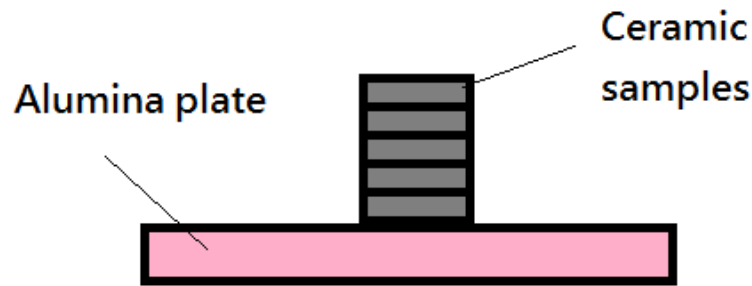


Figure 2.4 Schematic diagram of the binder removal process.

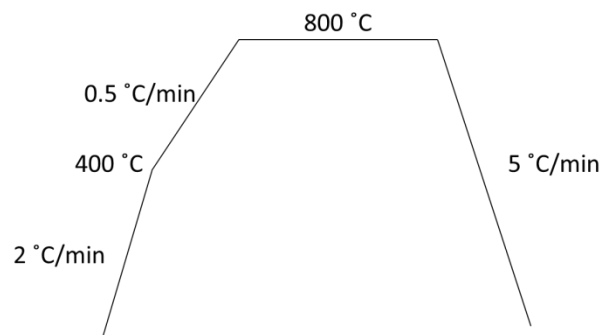


Figure 2.5 Temperature profile of the binder removal process.

After removal of the binder, the samples were put into a programmable Carbolite furnace for sintering. Sintering is a process for densifying the ceramics and reducing the size of the pores of the samples [97]. During sintering, the pores become smaller and more spherical in shape, and the properties of the samples can be enhanced. The temperature profile for the sintering process used in this project is shown in Figure 2.6. The samples were heated to the sintering temperature of 940 – 1080 °C at a heating rate of 2 °C/min. The samples were then kept at the sintering temperature for several hours to ensure complete densification.

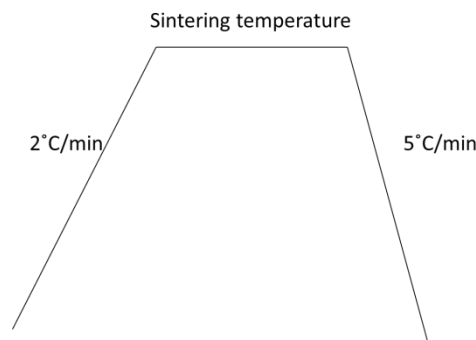


Figure 2.6 Temperature profile of the sintering process.

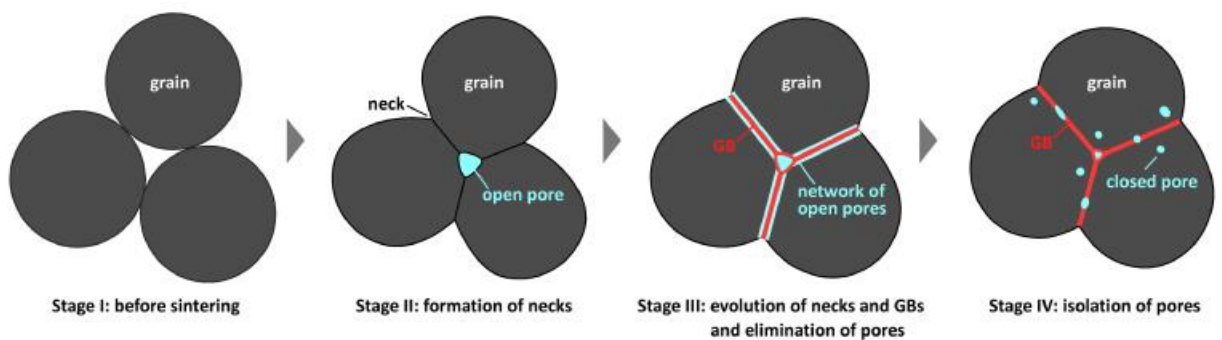


Figure 2.7 Schematic diagrams of stages in solid-state sintering [98].

The schematic diagram illustrating the sintering mechanism is shown in Figure 2.7. Stage I shows the arrangement of particles before sintering. Stage II is the early stage of sintering, where the contact angle of grains becomes shallower and the necks are formed. Stage III is the middle stage of sintering, where the necks grow up and the pores diffuse through and accumulate at grain boundaries. Stage IV is the final stage of sintering, where some pores are eliminated, and some are isolated to form closed pores. The grain boundary area increases progressively and densification occurs during sintering [98].



2.2.6 Polishing and Electroding

After sintering, the ceramic surfaces are rough due to shrinkage in the sintering process. Thus polishing is necessary before electroding. In this project, the ceramics were polished with silicon carbide abrasive papers until the thickness becomes uniform. If the thickness is not uniform, electric break down will easily occur at the thinner part under high electric fields. After polished, silver electrodes were fired on the top and bottom surfaces of the samples. The temperature profile for firing silver electrodes is shown in Figure 2.8.

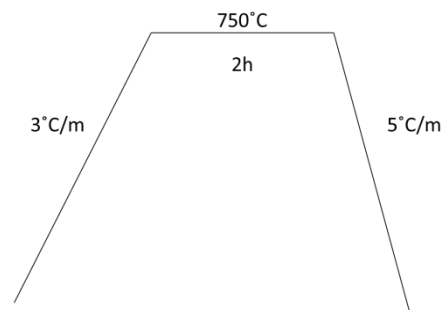


Figure 2.8 Temperature profile of the silver electrodes firing process.

2.2.7 Poling

Because of the random orientation of domains (regions with uniformly aligned dipoles), as-prepared polycrystalline ferroelectric ceramics do not exhibit piezoelectric properties. A poling process is required to induce the piezoelectric effect. In the process, a high electric field is applied to align the dipoles along a single direction. As a result, a remanent polarization is obtained and the ferroelectric ceramics become piezoelectric



THE HONG KONG POLYTECHNIC UNIVERSITY

(Figure 2.9). Obviously, the poling conditions are different for different materials.

The poling setup used in this project is shown in Figure 2.10. The sample was mounted on a holder and placed into a silicone oil bath during the poling process. The oil bath was heated up to the poling temperature and kept constant during the process. The applied voltage, V_{app} was calculated by:

$$V_{app} = \text{Poling Field} \times \text{Thickness of the disk} \quad (2.1)$$

The applied voltage was increased slowly to the designed value (poling field) and then was kept for a designated time (poling time). After that, the silicone oil bath was cooled down to room temperature. During cooling, the applied voltage was still kept at the designed value. After poling, the ceramic samples were short circuited by wrapping in an aluminum foil to remove the charges injected to the sample during the poling process. The general processing conditions for the KNLN-NS ceramics are listed in Table 2.1.

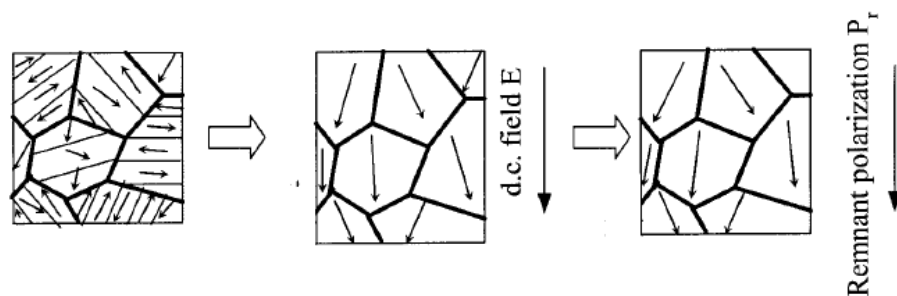


Figure 2.9 The switching of the ferroelectric grains polarization under DC electric field.

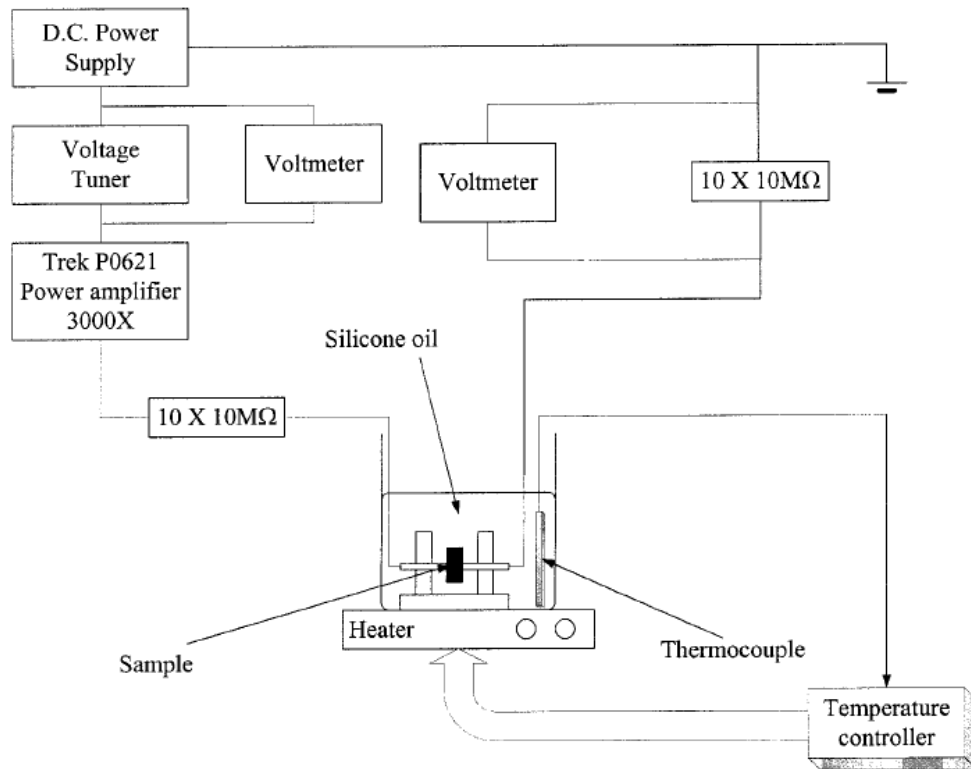


Figure 2.10 Schematic diagram of the DC poling circuit for ceramic sample.



Table 2.1 General processing conditions for fabricating the KNLN-NS ceramics.

Conventional Ball Mill	
Rotation Speed (rpm)	60
Milling time (h)	8
High-energy Ball Mill	
Rotation Speed (rpm)	200
Milling time (h)	2
Calcination	
Temperature (°C)	800
Time (h)	6
Pressing	
Pressure (MPa)	~440
Binder Removal	
Temperature (°C)	800
Time (h)	2
Poling	
Electric Field (kV/mm)	5.0
Temperature (°C)	150
Time (h)	0.5

2.3 Fabrication of Piezoelectric Vibratory Gyro-sensors

The schematic diagram of the piezoelectric vibratory gyro-sensor fabricated using the KNLN-NS ceramics in this project is shown in Figure 2.12. As the aim of this project is to develop gyro-sensors for consumer applications, the dimensions of the gyro-sensors are designed to be as small as possible. The gyro-sensor consists of a stack of two ceramic plates that are poled in opposite directions as shown in Figure 2.11.



THE HONG KONG POLYTECHNIC UNIVERSITY

When an electric field is applied along the z-axis, the two ceramic plates deform differently, e.g. the top one contracts along the x-axis while the bottom one expands because of the Poisson effects, and thus leading to a upward bending. Accordingly, when an ac electric field is applied to the stack, it vibrates along the z-axis, which is then served as the driving part of the gyro-sensor. As discussed in Chapter 1, if the vibrating stack is rotated about the x-axis, a Coriolis force will be induced and force the stack to vibrate along the y-axis. The induced vibrating motion is thus served as the sensing part of the gyro-sensor.

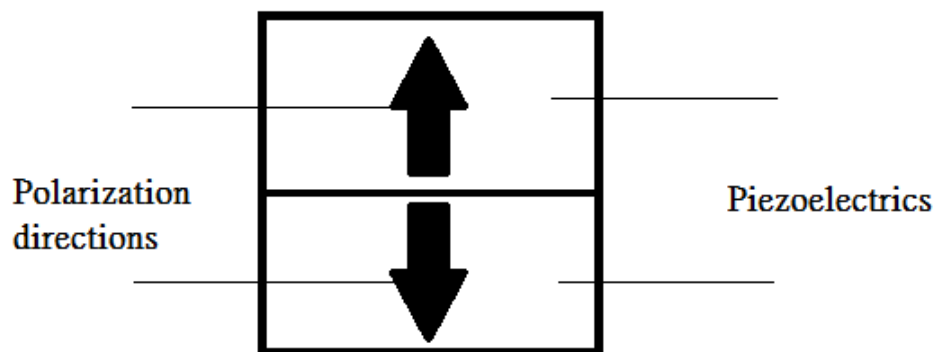


Figure 2.11 The polarization directions of the piezoelectrics.

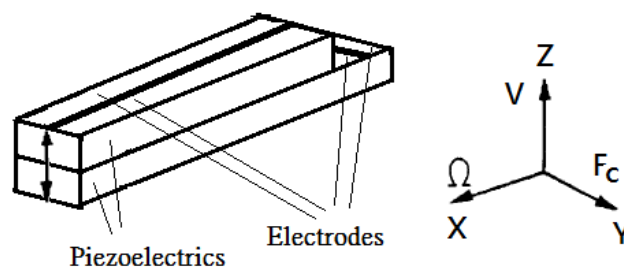


Figure 2.12 The schematic diagram of piezoelectric vibratory gyro-sensor.



2.3.1 Preparation of Piezoelectric Plates

Similar procedures were applied to prepare the piezoelectric ceramic plates for fabricating the gyro-sensors. The sintered disk samples were thinned down to 0.3 – 0.5 mm using silicon carbide abrasive papers. Silver electrodes were then fired on the top and bottom surfaces of the disk samples. After poling, the disk samples were cut into rectangular plates of dimensions 10 mm × 4 mm and 8 mm × 4 mm, respectively, using a dicing saw cutting machine. The ceramic plates were then used to fabricate the gyro-sensors.

2.3.2 Stacking, Cutting and Electroding the Bimorph Beams Gyro-sensors

The poled ceramic plates with their polarizations oriented oppositely were glued together using epoxy. The sample was pressed by a weight for 24 h to ensure a tight and firm adhesion. The schematic diagram of the double-layered stack is shown in Figure 2.13. Then the double-layered piezoelectric stack was cut into rods with a square cross-section as shown in Figure 2.13. Hence a bimorph beam was fabricated. The top electrode of the shorter plate was cut into two equal parts. The emerged top electrode of the longer plate was cut roughly into two parts, one of which was then electrically connected to the bottom electrode (of the longer plate) with silver paint. The schematic diagram of the bimorph-type piezoelectric vibratory gyro-sensors is shown in Figure 2.12.

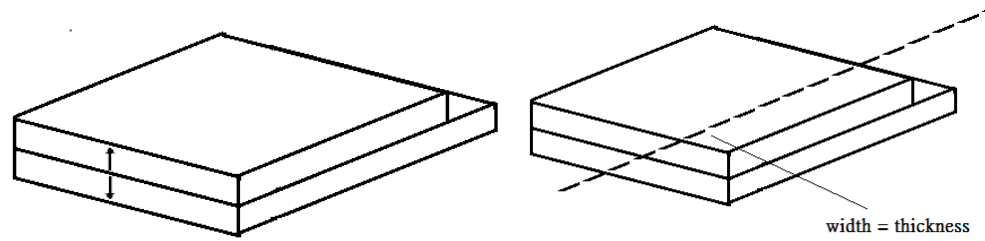


Figure 2.13 The schematic diagram of cutting the double layers ceramic into rod shape.



Chapter 3 Characterizations of Ceramics

3.1 Introduction

In this chapter, the KNLN-NS ceramics prepared by the two methods: high-energy ball milling (HEBM) and sintering aids, are characterized. Based on the properties, such as density, crystalline structure, microstructure, ferroelectric properties, dielectric properties and piezoelectric properties, the optimum processing and sintering conditions of the ceramics are determined.

3.2 Density

Density is an important parameter for evaluating the quality of ceramics. Defects and improper fabrication conditions can affect the densification and then the properties of the ceramics. In this project, the density ρ of the ceramics was measured by the Archimedes method. The mass of the ceramic in air m_{dry} and the mass of the ceramic suspended in water m_{water} were measured using an electronic balance. The density of the ceramic was calculated by:

$$\rho = \frac{m_{dry}}{m_{dry} - m_{water}} \times \rho_{water} \quad (3.1)$$

where ρ_{water} is the density of water (1.0 g/cm³).



3.3 Crystalline Structure

X-ray diffraction (XRD) analysis was used to study the crystalline structure of the ceramics using a Rigaku SmartLab X-ray diffractometer with CuK_α radiation ($\lambda = 0.154\text{nm}$). In the measurement, an X-ray beam is incident on the sample surface with an angle of θ (Figure 3.1). Owing to the interaction with the crystal lattices of the sample, part of the X-rays is scattered. The X-rays scattered from different lattices interfere with each other, causing a variation in intensity of the overall scattered (received) beam upon the change of θ , i.e., a diffraction pattern is produced. Due to the system geometry, only those reflections from lattice planes parallel to the surface are detected. The atoms in these planes act as a diffraction grating. Maximum in the detected intensity (i.e., diffraction peak) appears when the Bragg law is satisfied (Figure 3.1):

$$2d_{hkl} \sin \theta = n\lambda \quad (3.2)$$

where d_{hkl} is the interplanar spacing of the $\{hkl\}$ set of lattice planes with Miller indices h , k and l , n is an integer representing the order of the diffraction peak, and λ is the wavelength of the X-ray. X-ray diffraction may be used to determine the lattice parameters of a unit cell, to identify unknown compounds and to give information on the structural development as material is formed.

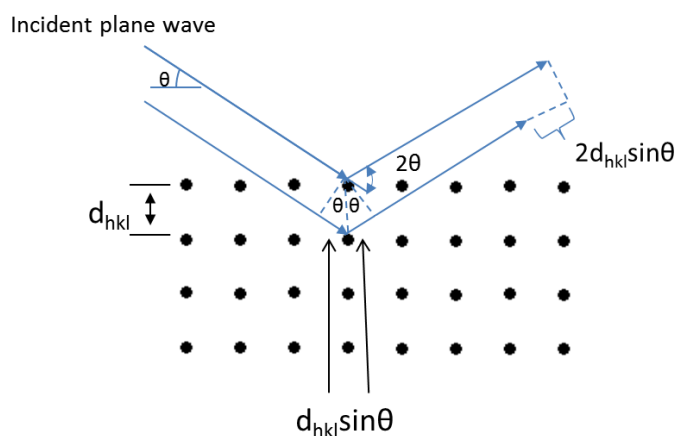


Figure 3.1 The schematic diagram of X-ray diffraction in crystal.

3.4 Microstructure

The microstructure of the KNLN-NS ceramics was examined using a scanning electron microscope (SEM) (JSM-6490, JEOL Ltd., Japan). SEM is a type of electron microscopes which produces images by focusing an electron beam on different positions of a sample surface. The electrons interact with atoms in the sample, and then producing signals that containing information of the surface topography and composition of the sample.

3.5 Ferroelectric Hysteresis Loop

Ferroelectric hysteresis loop (P-E loop) is one of the most important characteristics of ferroelectric materials. From the P-E loop, ferroelectric properties of the sample, such as the coercive field E_c and remanent polarization P_r , can be determined.



In this project, the P-E loop of the KNLN-NS ceramics was measured using a modified Sawyer Tower circuit [99]. The experimental setup for the measurement is schematically shown in Figure 3.2. An AC voltage at 100 Hz generated by a function generator (HP 8116A) and amplified by a voltage amplifier (Trek 609D-6) was applied to the sample, which was placed in a silicon oil bath for preventing from electrical breakdown at the sample edge. The polarization charges generated on the sample was collected by a reference capacitor that was connected in series with the sample and stored in the Sawyer-Tower Circuit Box. In order to minimize the effect on the polarization current, the capacitance of the reference capacitor was chosen to be at least 1000 times larger than that of the sample. The AC input voltage and the voltage across the reference capacitor were measured using a digital oscilloscope (HP 5465A), which was connected to a computer for data collection and analysis. The polarization P of the sample was calculated as:

$$P = \frac{C_o V_o}{A} \quad (3.3)$$

where C_o is the capacitance of the reference capacitor, V_o is the voltage across the reference capacitor, and A is the area of the sample.

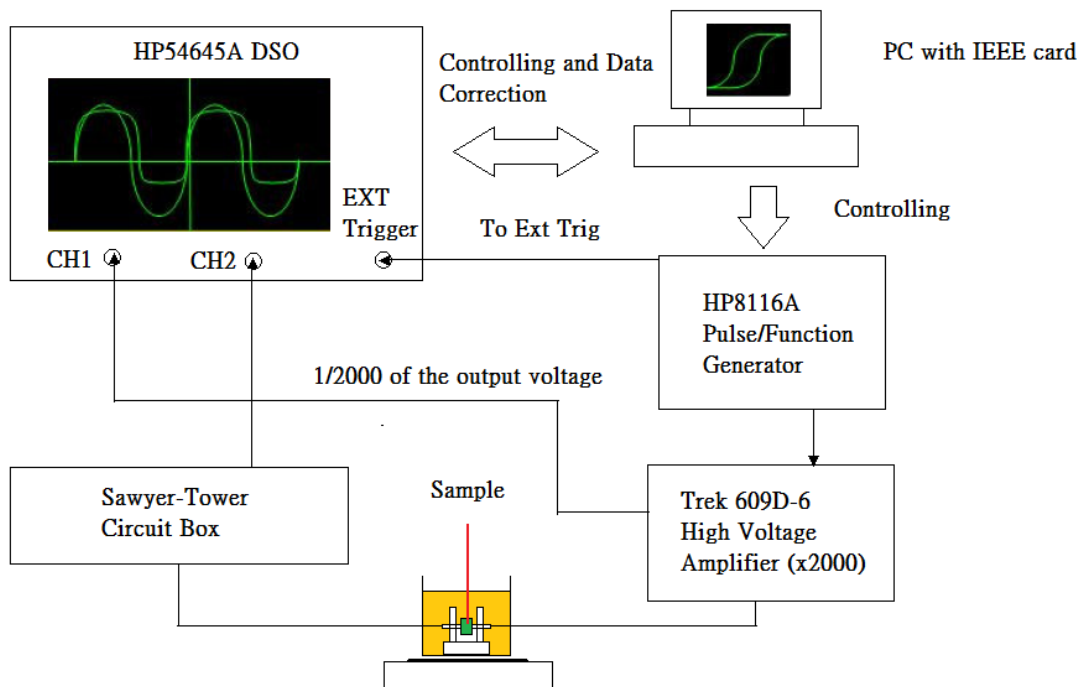


Figure 3.2 Schematic diagram of the experiment setup for P-E loop measurement.

3.6 Dielectric Properties

The relative permittivity ϵ_r and dielectric loss $\tan\delta$ of the KNLN-NS ceramics were measured at 1 kHz using a HP4294A precision impedance analyzer. The capacitance C of the sample was measured and ϵ_r was calculated as follows:

$$C = \frac{\epsilon_0 \epsilon_r A}{t} \quad (3.4)$$

where ϵ_0 is the permittivity of free space, A is the electrode area and t is the thickness of the sample.



Dielectric materials absorb electrical energy under an alternating electric field and hence have dielectric loss. The relative permittivity can be expressed in a complex form:

$$\varepsilon_r = \varepsilon_r' - i\varepsilon_r'' \quad (3.5)$$

where ε_r' is the real part of permittivity and ε_r'' is the imaginary part. The dielectric loss is given as:

$$\tan \delta = \frac{\varepsilon_r''}{\varepsilon_r'} \quad (3.6)$$

3.7 Piezoelectric Properties Measurement

The longitudinal piezoelectric coefficient d_{33} was measured based on the direct piezoelectric effect using a piezo d_{33} meter (model ZJ-3D, Beijing Institute of Acoustics). d_{33} is defined as:

$$d_{33} = \frac{D}{T} \quad (3.7)$$

where D is the dielectric displacement, and T is the elastic stress. In the measurement, the ceramic was placed in between two measuring probes in the meter and the value of d_{33} can be obtained from the meter directly. The measurement setup is shown schematically in Figure 3.3.

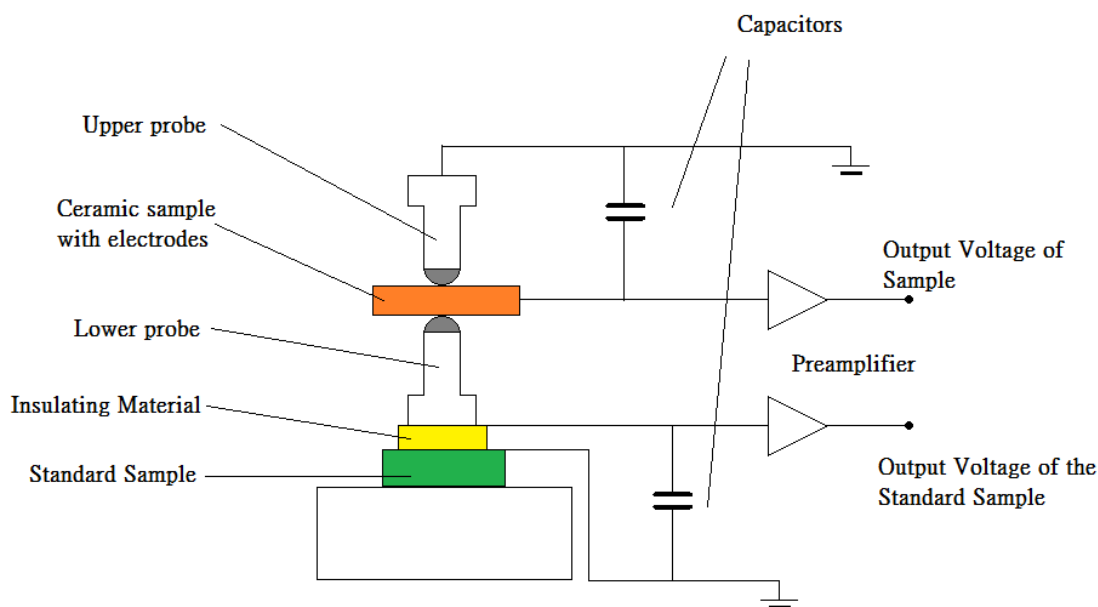


Figure 3.3 The schematic diagram of a d_{33} meter.

3.8 Results and Discussion

3.8.1 KNLN-NS Ceramics Prepared by High-Energy Ball Milling

Before preparing the KNLN-NS ceramics using high-energy ball milling (HEBM), the technique has been evaluated via the preparation of KNN ceramics. Table 3.1 summarizes the sintering conditions as well as the properties of the KNN ceramics prepared by conventional ball-milling (CBM) and HEBM. The general processing conditions are listed in Table 2.1. It can be seen that both the KNN ceramics exhibit similar dielectric and piezoelectric properties. The HEBM technique cannot lower the sintering temperature of the ceramics significantly. However, probably due to the



THE HONG KONG POLYTECHNIC UNIVERSITY

higher-speed collision, the grains of the ceramic prepared by HEBM are smaller and uniform (Figure 3.4 and 3.5) [55].

Table 3.1 Characteristics of KNN ceramics prepared by CBM and HEBM.

	CBM	HEBM
Sintering Condition		
Temperature (°C)	1100	1100
Time (h)	4	4
Density (g/cm ³)	4.23	4.25
ϵ_r	~1020	~1050
$\tan\delta$ (%)	4.6	5.8
d_{33} (pC/N)	89	83

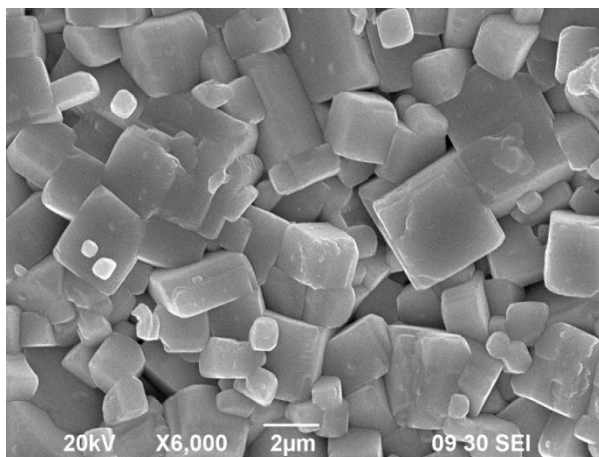


Figure 3.4 SEM micrograph of the KNN ceramic prepared by CBM.

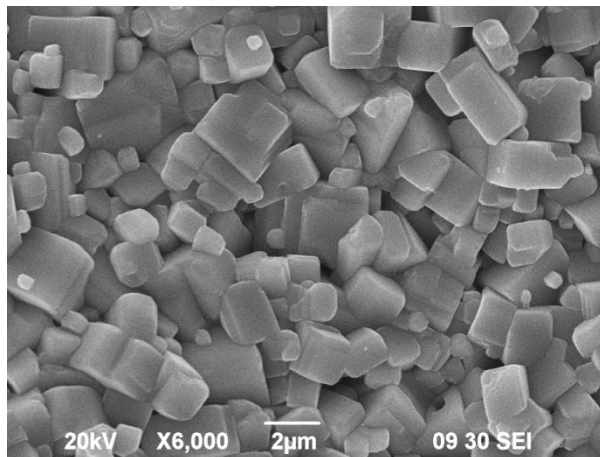


Figure 3.5 SEM micrograph of the KNN ceramic prepared by HEBM.

The sintering conditions and properties of the KNLN-NS ceramics prepared by CBM and HEBM are compared in Table 3.2. The general processing conditions are listed in Table 2.1. Similar to KNN, the sintering of the KNLN-NS ceramics is not affected significantly by the HEBM technique. The sintering temperature of the ceramics remains the same at 1080°C, and the observed density increases only slightly from 4.35 g/cm³ to 4.47 g/cm³ after using HEBM. There are also no significant changes in the ferroelectric and dielectric properties of the ceramics. The observed P_r and E_r remain almost unchanged at 17 $\mu\text{C}/\text{cm}^2$ and 1.3 kV/mm, respectively, while ϵ_r and $\tan\delta$ are ~ 1450 and 3.0%, respectively. The P-E loops of the ceramics are shown in Figure 3.6. However, the observed d_{33} decreases by about 30%, from 240 pC/N to 170 pC/N.



Table 3.2 Characteristic of KNLN-NS ceramics prepared by CBM and HEBM.

	CBM	HEBM
Sintering Condition		
Temperature (°C)	1080	1080
Time (h)	4	4
Density (g/cm ³)	4.35	4.47
ϵ_r	~1530	~1450
$\tan\delta$ (%)	2.4	3.0
d_{33} (pC/N)	240	170

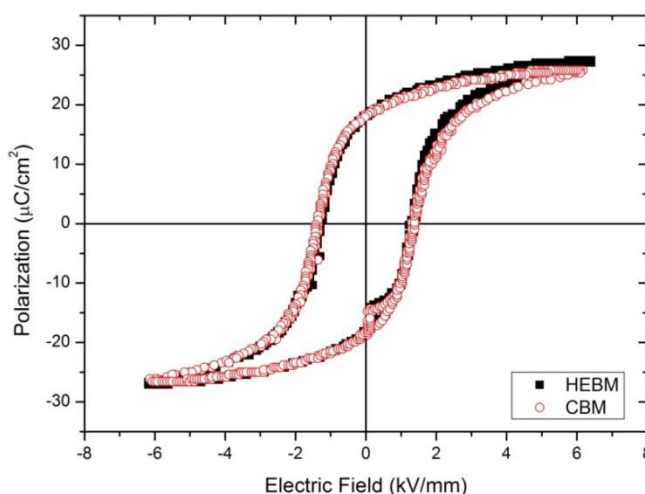


Figure 3.6 Ferroelectric hysteresis loops of the KNLIN-NS ceramics prepared by CBM and HEBM.

Figure 3.7 and 3.8 show the SEM micrographs of the ceramics prepared by CBM and HEBM, respectively. For the ceramic prepared by CBM (Figure 3.7), the grain size is not uniform, varying from 1 μm to 5 μm . The grains of the ceramic prepared by HEBM are more uniform and smaller ($\sim 1 \mu\text{m}$). The reduction in grain size may be the partial reason for the decrease in d_{33} [100]. The degraded piezoelectric properties may also be due to the impurity produced from the high-speed collision between the tungsten carbide balls, which is inevitable for HEBM processes [101].

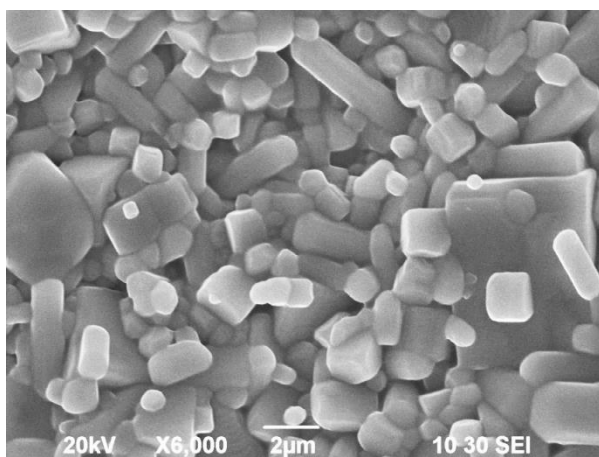


Figure 3.7 SEM micrograph of the KNLN-NS ceramic prepared by CBM.

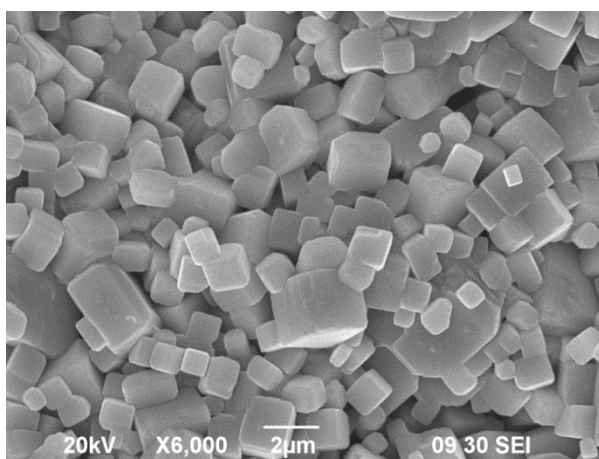


Figure 3.8 SEM micrograph of the KNLN-NS ceramic prepared by HEBM.

Dense KNLN-NS ceramics can be prepared using HEBM. Although the grain size distribution is improved, the grains become smaller and then the piezoelectric coefficient of the ceramics decreases by about 30%. However, the sintering temperature cannot be reduced, still remaining at $\sim 1080^{\circ}\text{C}$. The unchanged sintering temperature may also be due to the impurity produced from the HEBM or the not enough milling time. Therefore, HEBM may not be a good choice for lowering the sintering temperature of the KNLN-NS ceramics.



3.8.2 KNLN-NS ceramics prepared Using Sintering Aid

The effects of sintering temperature on the KNLN-NS ceramics (without sintering aids) are first investigated. Then the effects of the sintering aid, Cu/Ba complex, on the sintering temperature and properties of the KNLN-NS ceramics are studied.

3.8.2.1 KNLN-NS Ceramics

Figure 3.9 shows the density of the KNLN-NS ceramics sintered at different temperatures. The ceramics become molten as the sintering temperature increases higher than 1080°C. It can be seen that the ceramic sintered at 1080°C has the highest density of 4.35 g/cm³. The ceramic also possesses a dense structure as shown in Figure 3.10a. The average grain size is ~3 μm. As the sintering temperature decreases, the observed density decreases (Figure 3.9). The amount of pores also increases and the grain size decreases with decreasing the sintering temperature (Figure 3.10b-e). These should be attributed to the incomplete densification caused by the low sintering temperatures.

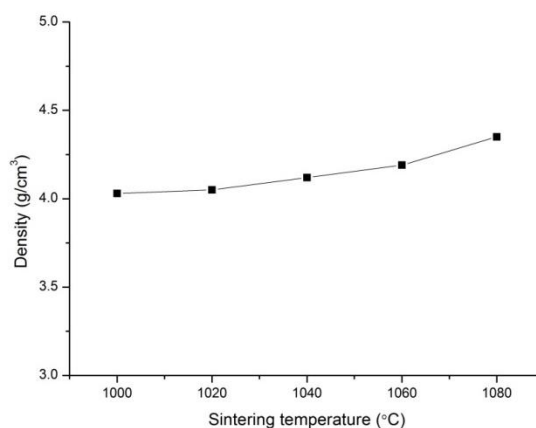


Figure 3.9 Density measurement of KNLN-NS with different sintering temperature.

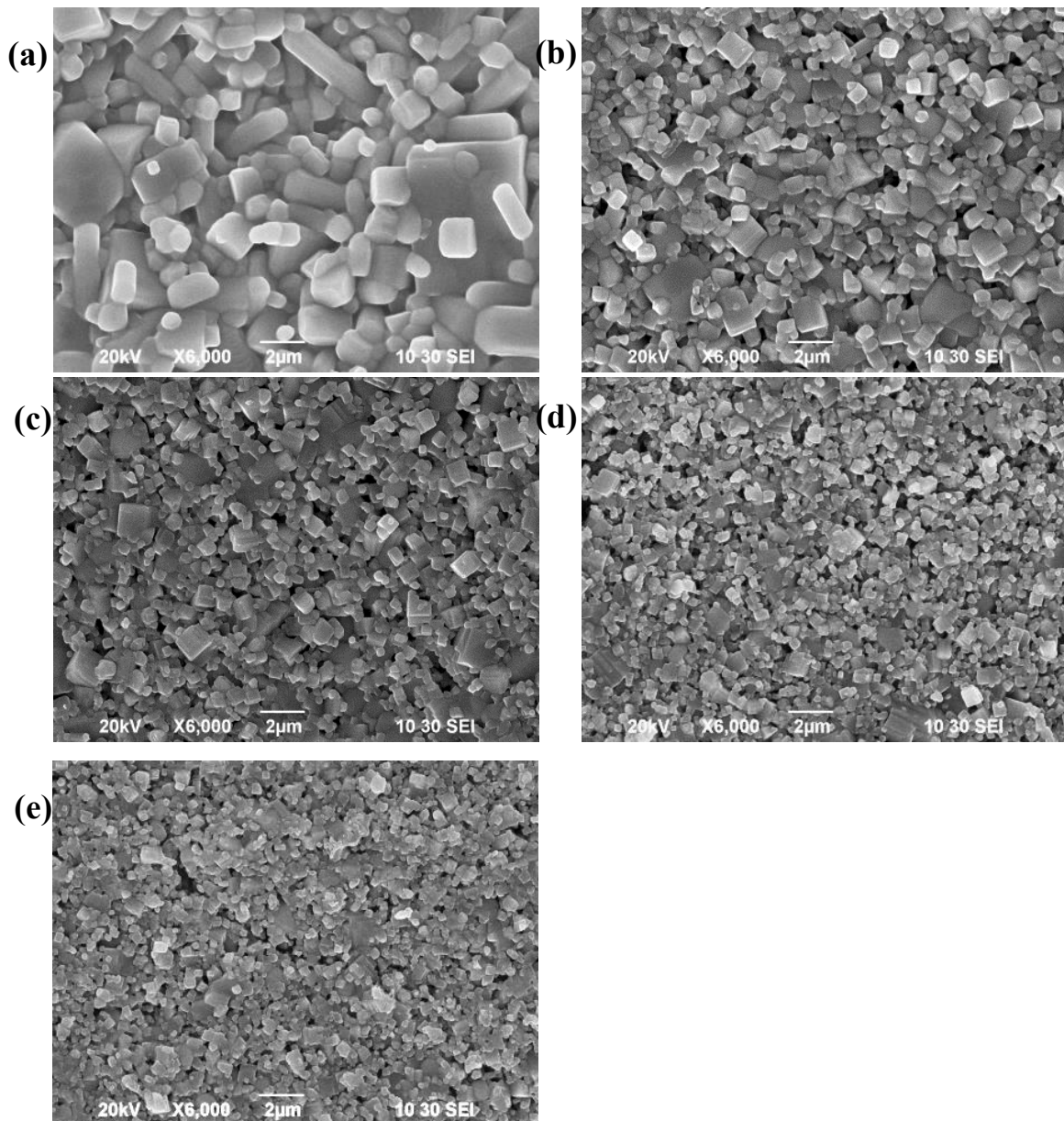


Figure 3.10 SEM micrograph of KNLN-NS sintering at (a) 1080°C, (b) 1060°C, (c) 1040°C, (d) 1020°C and (e) 1000 °C.

The variations of ϵ_r and $\tan\delta$ with sintering temperature for the KNLN-NS (unpoled) ceramics are shown in Figure 3.11. For the ceramic sintered at 1080°C, the observed ϵ_r has the highest value of 1530 and $\tan\delta$ has the lowest value of 2.4%. As the sintering temperature decreases, the observed $\tan\delta$ increases. For the ceramics sintered at temperature below 1060°C, $\tan\delta$ becomes very large, usually $> 40\%$. This should be



THE HONG KONG POLYTECHNIC UNIVERSITY

partly caused by the porosity as shown on Figure 3.10. However, the observed ϵ_r does not change significantly (Figure 3.11). Even for the ceramics sintered at low temperatures, the observed ϵ_r remained at ~ 1500 which is close to the value published for well-sintered ceramics [14]. As the ceramics had been stored in laboratories for several days before the measurements, the high ϵ_r as well as $\tan\delta$ for the porous ceramics may be caused by the moisture absorbed in the ceramics. Accordingly, the ceramics were heated at 120°C for 24 h and the dielectric measurements were repeated, giving the results shown in Figure 3.11. It can be seen that the observed ϵ_r and $\tan\delta$ for the porous ceramics (i.e., sintered at temperatures $< 1060^\circ\text{C}$) decrease significantly after the removal of moisture. It has been noted that the observed ϵ_r and $\tan\delta$ for these ceramics increases to high values again after storing in laboratory for 2 days.

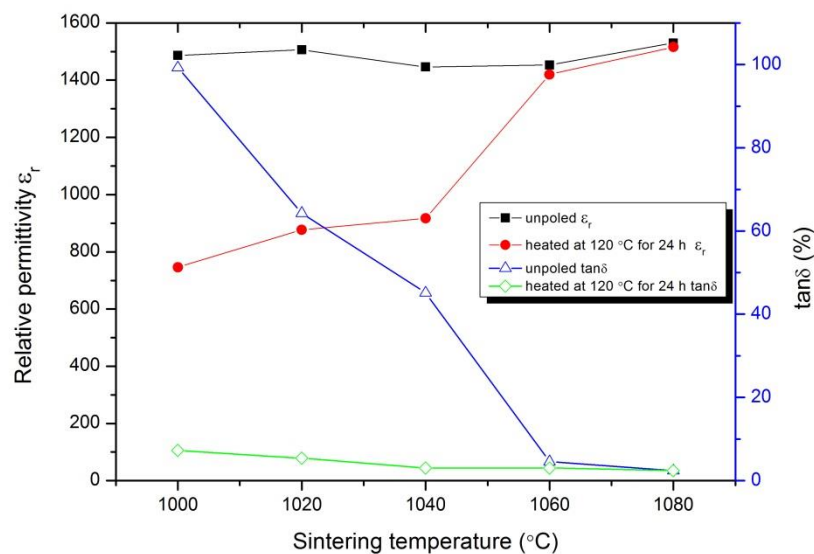


Figure 3.11 Dielectric properties of KNLN-NS of different sintering temperature measured at 1 kHz.



THE HONG KONG POLYTECHNIC UNIVERSITY

Figure 3.12 shows the observed d_{33} of the KNLN-NS ceramics sintered at different temperatures. The observed d_{33} increases with increasing sintering temperature, and reaches the highest value of 240 pC/N at 1080°C. Similar to the dielectric properties, the low d_{33} for the ceramics sintered at low temperatures should be attributed to the high porosity. In general, a high $\tan\delta$ (e.g. > 10%) will cause current leakage, and hence piezoelectric ceramics with high $\tan\delta$ cannot be poled and then cannot be used in practical applications. For the ceramics sintered at temperature < 1060°C, the moisture is removed during the poling at 150°C, and hence they can be (partially) poled under a high electric field of 5.0 kV/mm and exhibit piezoelectric properties in spite of the high $\tan\delta$ ($\geq 40\%$).

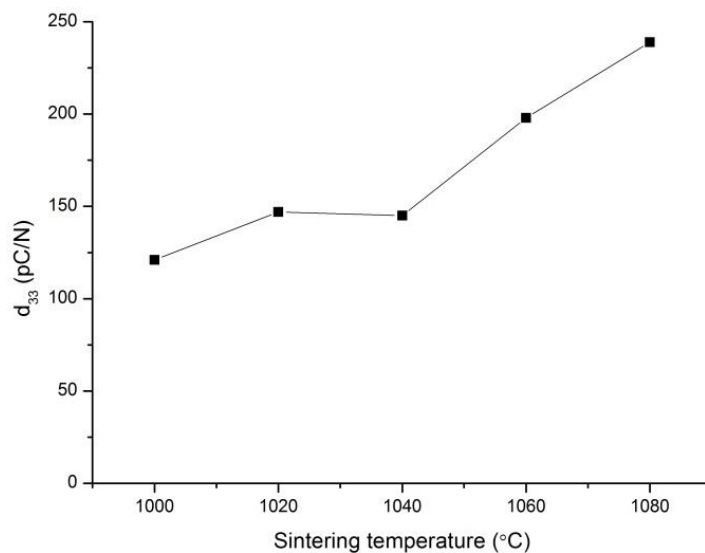


Figure 3.12 Piezoelectric properties of KNLN-NS of different sintering temperature.

The variations of ϵ_r and $\tan\delta$ with time for the poled KNLN-NS ceramics are shown in Figure 3.13 and 3.14. After poling, the observed ϵ_r for the ceramics sintered at 1060°C and 1080°C increases by about 10% while that of the ceramics sintered at lower



THE HONG KONG POLYTECHNIC UNIVERSITY

temperatures decreases by about 10%. The observed $\tan\delta$ for all the ceramics decreases to a small value of $\sim 2\%$. For the ceramics sintered at 1060°C and 1080°C , the observed ε_r and $\tan\delta$ remain almost unchanged with time. Probably due to the absorbed moisture, both ε_r and $\tan\delta$ for the ceramics sintered at $< 1060^\circ\text{C}$ increase with time. However, unlike the un-poled ceramics, the changes arisen from the moisture are not so large, in particular for ε_r .

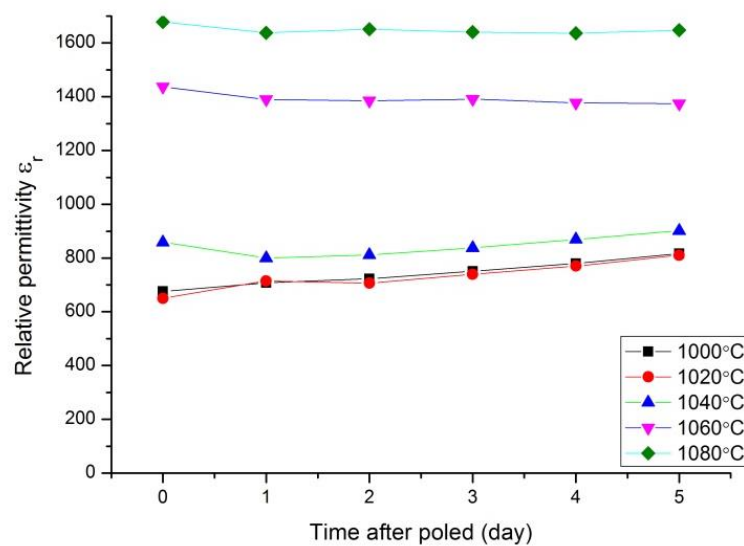


Figure 3.13 Variation of ε_r with the day after poled for KNLN-NS ceramics.

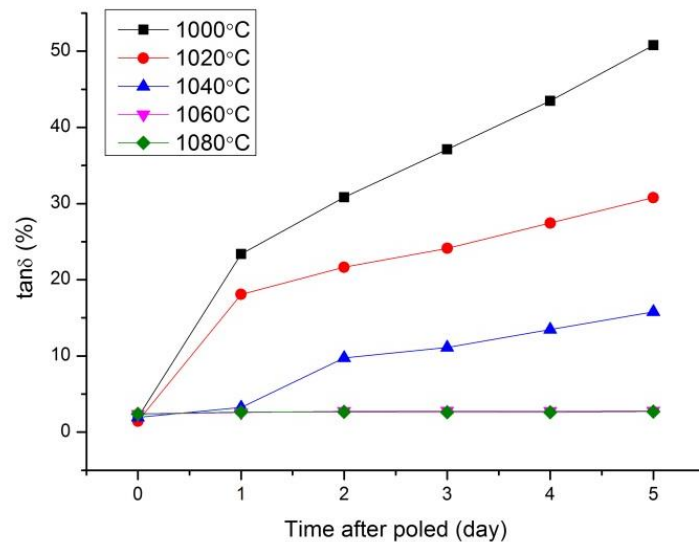


Figure 3.14 Variation of $\tan\delta$ with the day after poled for KNLN-NS ceramics.

Consistent with the common knowledge, a high sintering temperature is preferred for promoting densification and then enhancing the properties of ceramics [102]. For the KNLN-NS ceramics, the optimum sintering temperature and time are 1080°C and 4 h, respectively.

3.8.2.2 KNLN-NS-Cu/Ba Ceramics

Although a high temperature is preferred for sintering the KNLN-NS ceramics to a high density, a sintering temperature of 1000°C is used in studying the effects of the Cu/Ba (in a molar ratio of 71.5/28.5) sintering aids. As discussed, one of the aims of the present project is to develop low-temperature sintered KNN-based ceramics for multilayered devices. It has been shown that the relatively cheap Pd/Ag (30/70) inner electrode can be co-fired with ceramics up to 1000°C [103]. Therefore, a sintering



THE HONG KONG POLYTECHNIC UNIVERSITY

temperature of 1000°C is used for the investigation in determining the optimum content of Cu/Ba. A long sintering time of 8 h is also adopted to ensure the densification at low sintering temperatures can be completed. In this section, KNLN-NS ceramics added with different wt% of Cu/Ba have been prepared and characterized, and the samples are labeled as KNLN-NS-CuBa-x, where x denote the wt% of the Cu/Ba sintering aid.

Figure 3.15 shows the density of the KNLN-NS-Cu/Ba-x ceramics. As discussed in the previous section, the densification of the KNLN-NS-Cu/Ba-0 (i.e. KNLN-NS) ceramic at 1000°C is not completed (or even not started), and thus leading to a porous structure and a low density (Figure 3.10e). After the addition of Cu/Ba, the observed density increases, indicating that the densification is promoted. For the ceramics with $x \geq 2.5$, the density has a high value of 4.43 g/cm³.

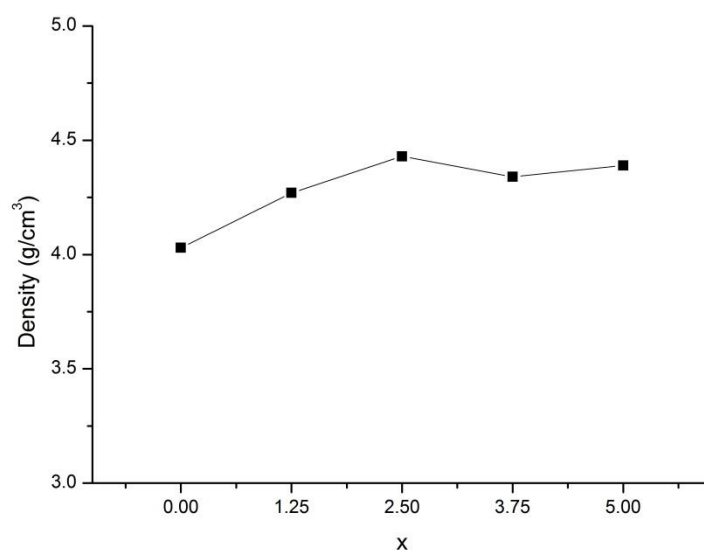


Figure 3.15 Variation of density with x for the KNLN-NS-Cu/Ba-x ceramics.



The SEM micrographs of the KNLN-NS-Cu/Ba-x ceramics are shown in Figure 3.16. As compared with the KNLN-NS ceramics (Figure 3.10e), the grain size of the ceramics is larger, indicating that the densification is improved. The grains of the ceramics with $x > 0$ are more uniform in size. The grain size increases slightly with x (wt% of Cu/Ba). For the KNLN-NS-Cu/Ba-2.5, the grains size is about $2\ \mu\text{m}$. Probably due to the excess content, the grains of the ceramic with $x = 5$ become non-uniform in size, having a mixture of large grains ($> 2\ \mu\text{m}$) and small grains ($< 0.5\ \mu\text{m}$).

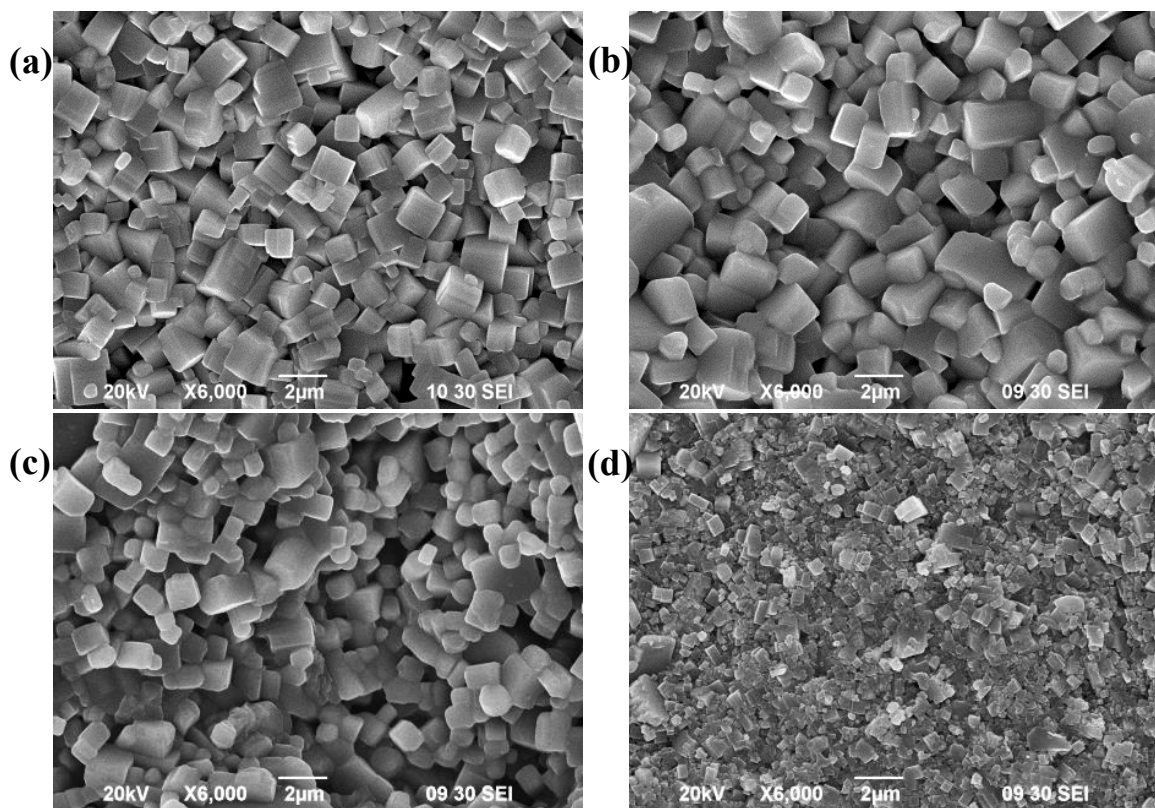


Figure 3.16 SEM micrographs of the KNLN-NS-Cu/Ba-x ceramics: (a) $x = 1.25$; (b) $x = 2.5$; (c) $x = 3.75$; and (d) $x = 5$.



THE HONG KONG POLYTECHNIC UNIVERSITY

Figure 3.17 shows the P-E loops of the KNLN-NS-Cu/Ba-x ceramics. All the ceramics exhibit a typical P-E loop. Similarly, probably due to the excess content, the P-E loop of the ceramic added with 5 wt% Cu/Ba is not well-saturated. The variations of P_r and E_c of the ceramics are shown in Figure 3.18.

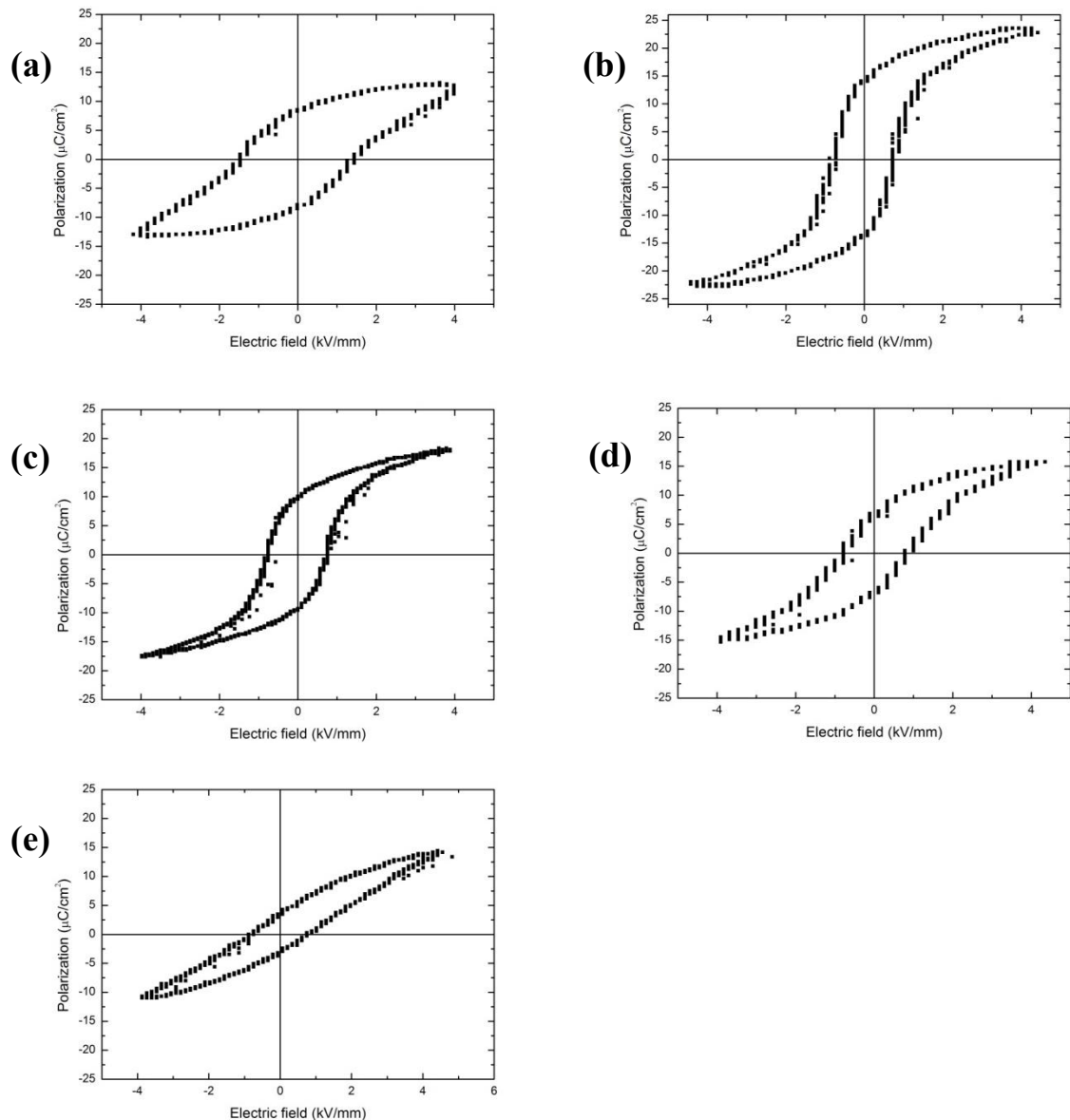


Figure 3.17 Ferroelectric hysteresis loops (100Hz) of KNLN-NS-Cu/Ba-x ceramics: (a) $x = 0$; (b) $x = 1.25$; (c) $x = 2.5$; (d) $x = 3.75$; and (e) $x = 5$.

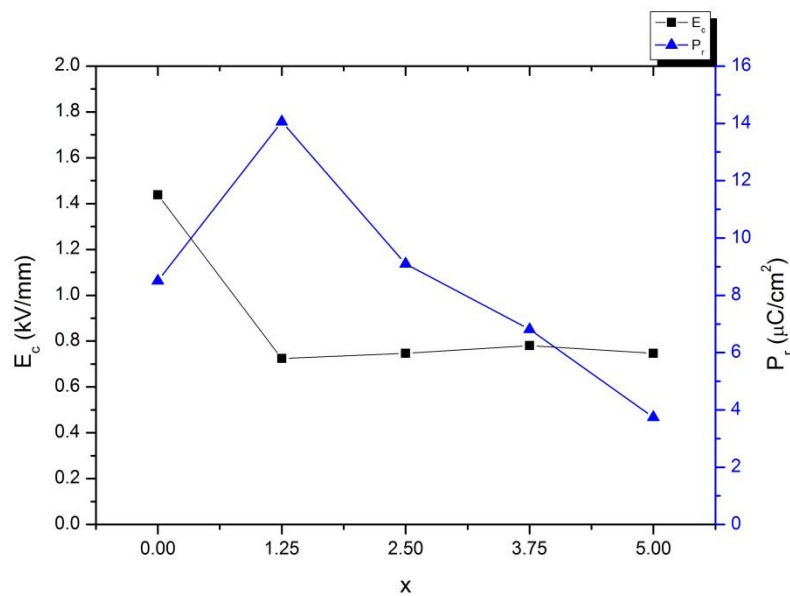


Figure 3.18 E_c and P_r of KNLN-NS-Cu/Ba-x ceramics measured at 100 Hz.

The XRD patterns of the KNLN-NS-Cu/Ba-x ceramics are shown in Figure 3.19. All the ceramics possess a pure perovskite structure. Probably due to the small amount, no secondary phase associated with the Cu/Ba complex is observed (Figure 3.19a). As also shown in Figure 3.19b, the diffraction peaks (202) and (020) of the ceramic with $x = 5.0$ become merged into a single peak, suggesting that the ceramic may be transformed into another phase, e.g., pseudocubic. This may be the cause for the abnormal grain distribution as shown in Figure 3.16d and the degraded piezoelectric properties which will be shown in the following section.

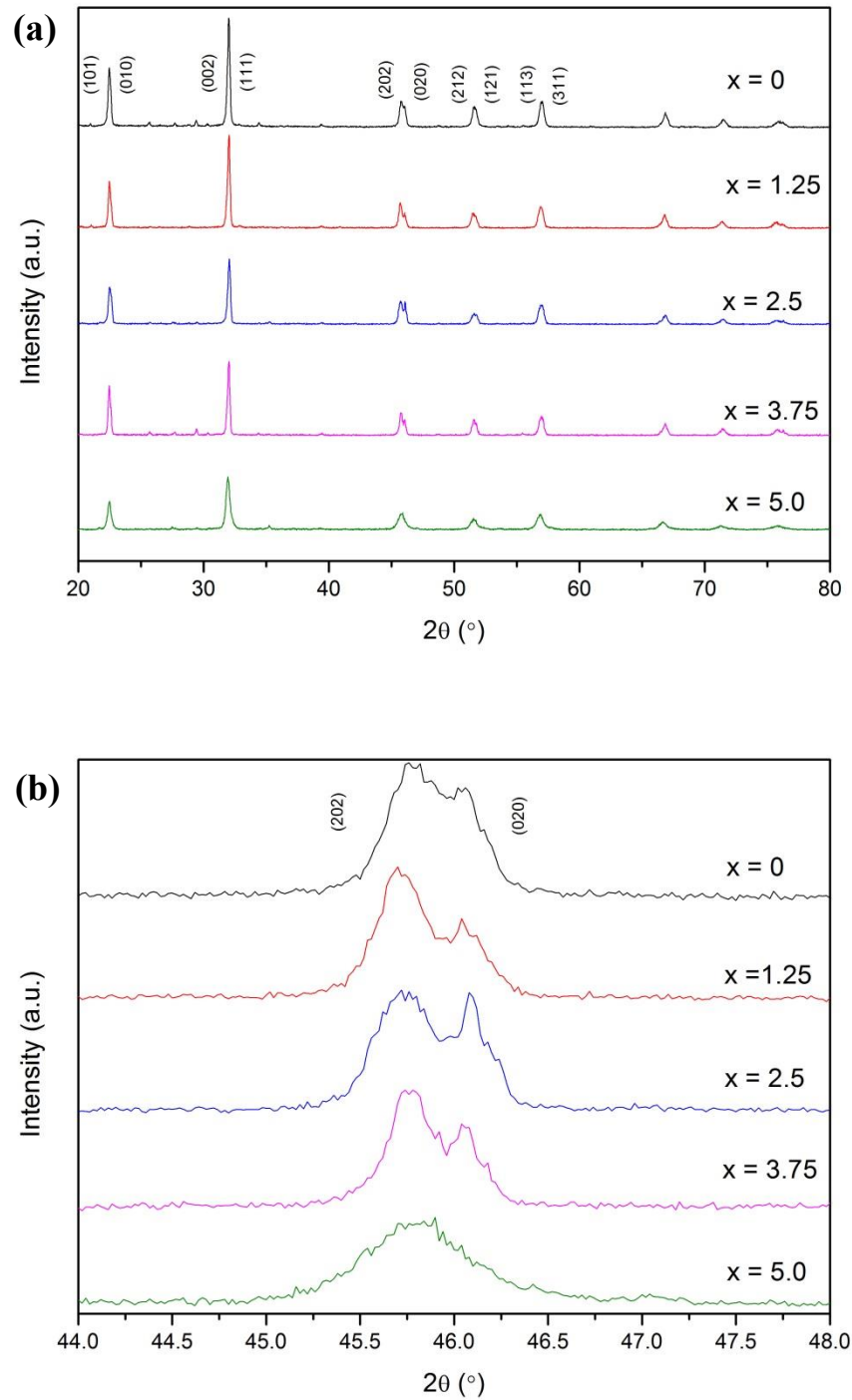


Figure 3.19 X-ray diffraction patterns of the KNLN-NS-Cu/Ba-x ceramics: (a) $\theta = 20^\circ$ - 80° and (b) $\theta = 44^\circ$ - 48° .



THE HONG KONG POLYTECHNIC UNIVERSITY

The variations of ϵ_r and $\tan\delta$ with x for the un-poled KNLN-NS-Cu/Ba- x ceramics are shown in Figure 3.20. The samples have been stored in the laboratory for several days before the measurement. The observed $\tan\delta$ decreases significantly with increasing x , and reaches a low value of 1.3% at $x \geq 2.5$. This is consistent with the variation of density as shown in Figure 3.15, suggesting that the high $\tan\delta$ for the ceramics with $x < 2.5$ should be partly due to the incomplete densification and high porosity of the ceramics. Similarly to the KNLN-NS ceramics, the high $\tan\delta$ should also be partly due to the absorbed moisture.

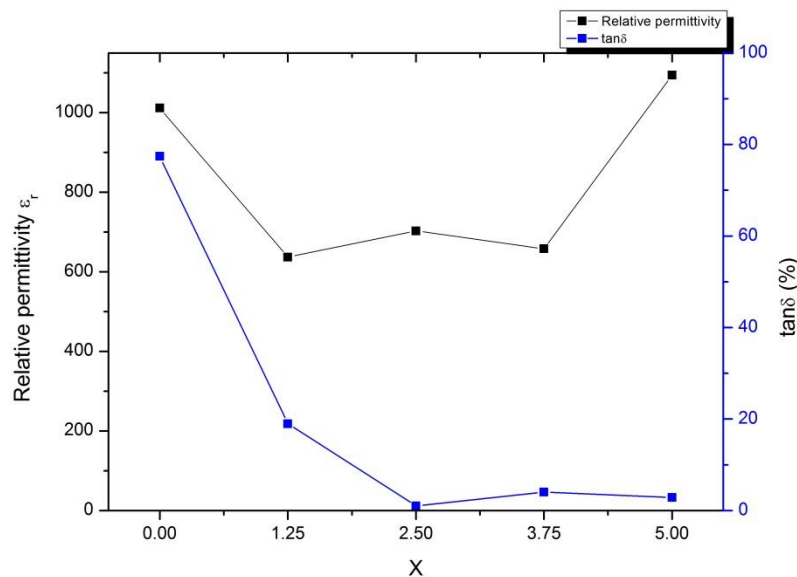


Figure 3.20 Dielectric properties of KNLN-NS-Cu/Ba- x ceramics measured at 1 kHz.

Figure 3.21 shows the variation of d_{33} with x for the KNLN-NS-Cu/Ba- x ceramics. Similarly, because of the high poling temperature (150°C), the absorbed moisture is removed and hence the ceramics, in particular for those with $x < 2.5$, can withstand the high poling field (5.0 kV/mm), without severe current leakage or electrical breakdown. As shown in Figure 3.21, the observed d_{33} increases after the



THE HONG KONG POLYTECHNIC UNIVERSITY

addition of Cu/Ba, and then decreases with increasing x . However, it is interesting to note that the ceramic with $x = 1.25$ exhibits the highest d_{33} (153 pC/N), in spite of the incomplete densification (low density and high $\tan\delta$) and smaller grain size. As discussed, the low d_{33} for the ceramic with $x = 5$ should be partly due to the excess content of Cu/Ba and partly due to the change of the crystal structure (Figure 3.16).

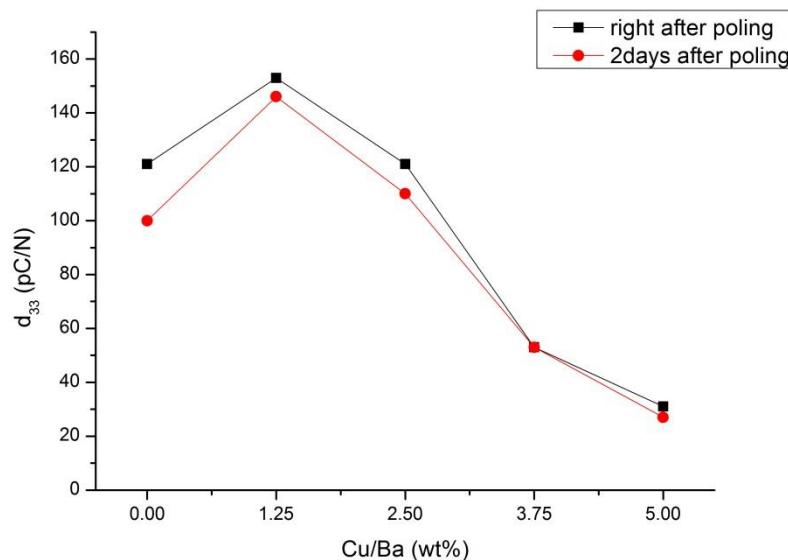


Figure 3.21 Piezoelectric properties of KNLN-NS-Cu/Ba- x ceramics.

The dielectric properties of the poled KNLN-NS-Cu/Ba- x ceramics are shown in Figure 3.22, in which both the data measured right after and 2 days after poling are presented. For all the ceramics, the observed ε_r are similar to those for the un-poled samples and does not change significantly after storing in laboratory for 2 days. For the well-densified ceramics (i.e., $x \geq 2.5$), the observed $\tan\delta$ remains at a small value ($\sim 3\%$) after poling and does not change with time. For the ceramics with $x < 2.5$, partly due to the removal of moisture during the high-temperature poling, the observed $\tan\delta$



THE HONG KONG POLYTECHNIC UNIVERSITY

decreases to a small value ($\sim 3\%$) after poling. However, probably because of moisture absorption, it increases significantly ($>20\%$) after 2 days, and then remains almost unchanged with time. Similar to the KNLN-NS ceramics, the poling process (the alignment of dipoles) as well as the addition of Cu/Ba can restrict the moisture absorption and then reduce the change of $\tan\delta$. Again, $\tan\delta$ can return to the low values after the ceramics are heated at high temperatures (e.g., 120°C) for several hours (e.g., 24 h).

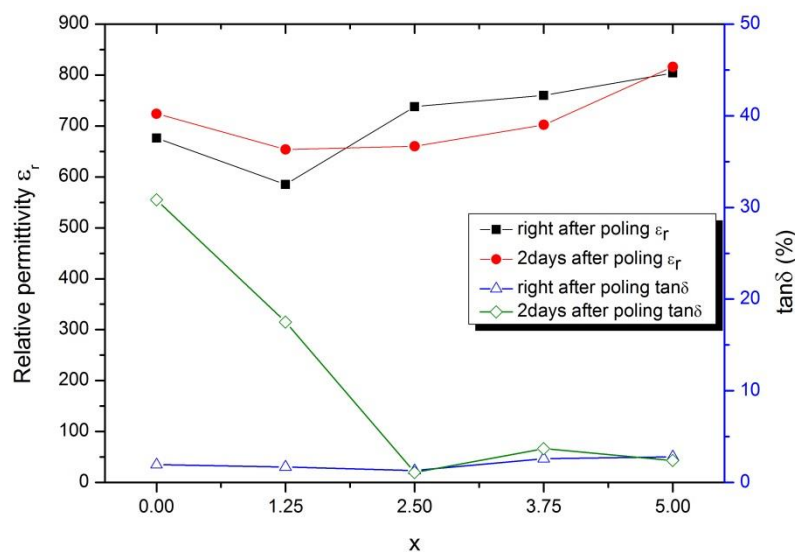


Figure 3.22 Dielectric properties of KNLN-NS-Cu/Ba-x ceramics measured at 1 kHz after poled.

Although the dielectric properties of the ceramics with incomplete densification are affected by moisture, it has no significant effect on the piezoelectric properties. As also shown in Figure 3.21, the observed d_{33} for all the ceramics, except for $x = 0$, remains almost unchanged after storing in the laboratory for 2 days. The KNLN-NS-Cu/Ba-1.25 still has the highest d_{33} (~ 140 pC/N). It can then be used in practical



THE HONG KONG POLYTECHNIC UNIVERSITY

applications as long as the high $\tan\delta$ does not cause significant problems, e.g., current leakage and high energy consumption. As compared with the KNLN-NS ceramics sintered at 1080°C (240 pC/N), the observed d_{33} for the KNLN-NS-Cu/Ba ceramics are lower. This may be partly due to the smaller grain size, less dense microstructure and residues of Cu/Ba. Nevertheless, as the KNLN-NS-Cu/Ba-2.5 be well-densified at a low temperature (1000°C) and has stable piezoelectric properties ($d_{33} = 121$ pC/N) and dielectric properties ($\epsilon_r = 740$), in particular the low $\tan\delta$ (1.3%), it should be a promising candidate for practical applications, in particular for multilayered devices.

As discussed, a sintering temperature of 1000°C, which is the maximum temperature used for co-firing with Pd/Ag inner electrode, is first used for studying the effects of Cu/Ba so as to determine the optimum content. Next, the effects of sintering temperature are studied. As the KNLN-NS-Cu/Ba-2.5 ceramic exhibits the optimum properties, the study is focused on it. Figure 3.23 shows the density of the ceramic sintered at different temperatures. The sintering time is still 8 h. It can be seen that a high density (~ 4.40 g/cm³) can be obtained in a temperature range from 960°C to 1020°C.

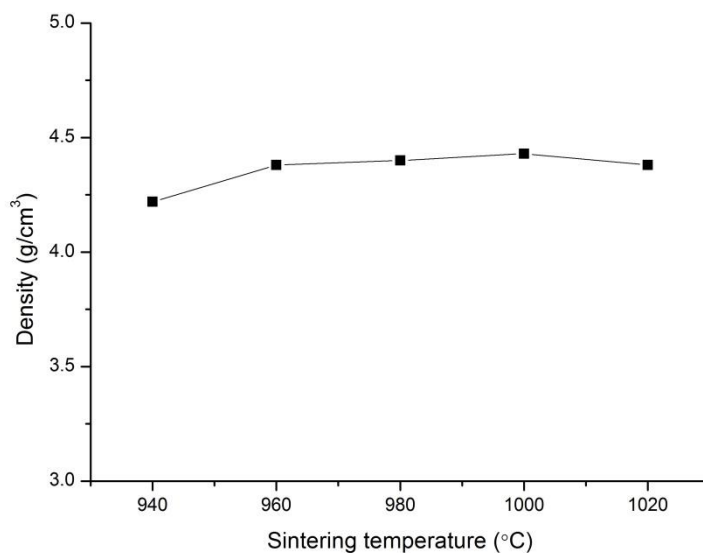


Figure 3.23 Density measurement of KNLN-NS-Cu/Ba-2.5 sintered at different temperature.

The SEM micrographs of the ceramics sintered at different temperatures are shown in Figure 3.24. Consistent with the density measurement, the ceramics sintered in the temperature range of 960°C – 1020°C generally possess larger grains ($\sim 2 \mu\text{m}$). The small grains of the ceramic sintered at 940°C are probably due to the incomplete densification.

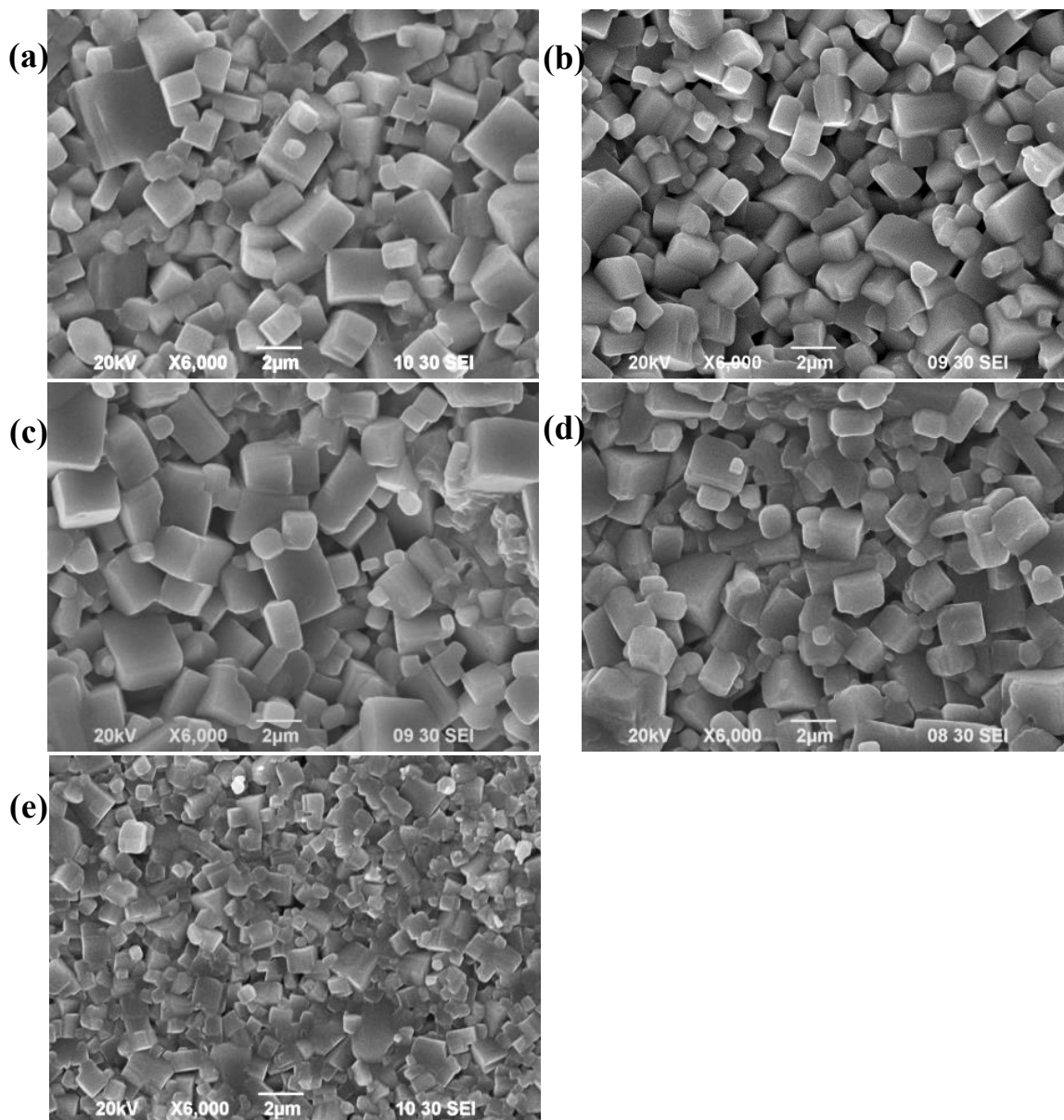


Figure 3.24 SEM micrograph of KNLN-NS-Cu/Ba-2.5 sintered at (a) 1020°C, (b) 1000°C, (c) 980°C, (d) 960°C and (e) 940°C.

The variations of ϵ_r and $\tan\delta$ with sintering temperature for the poled ceramics are shown in Figure 3.25. In general, the ceramic sintered at higher temperature exhibit higher ϵ_r and lower $\tan\delta$, but the differences are not significant. These should be



THE HONG KONG POLYTECHNIC UNIVERSITY

attributed to the higher density and larger grains. It is noted that even for the ceramic sintered at 940°C, the observed $\tan\delta$ is low, about 2%, indicating the good densification promoted by the sintering aid. Figure 3.26 shows the variation of d_{33} with sintering temperature for the ceramics. For the ceramic sintered in the temperature of 960°C – 1020°C, the observed d_{33} are similar, having a high value of ~ 120 pC/N. Probably due to the smaller grains and higher porosity, the ceramic sintered at 940°C exhibit a lower d_{33} (~ 80 pC/N).

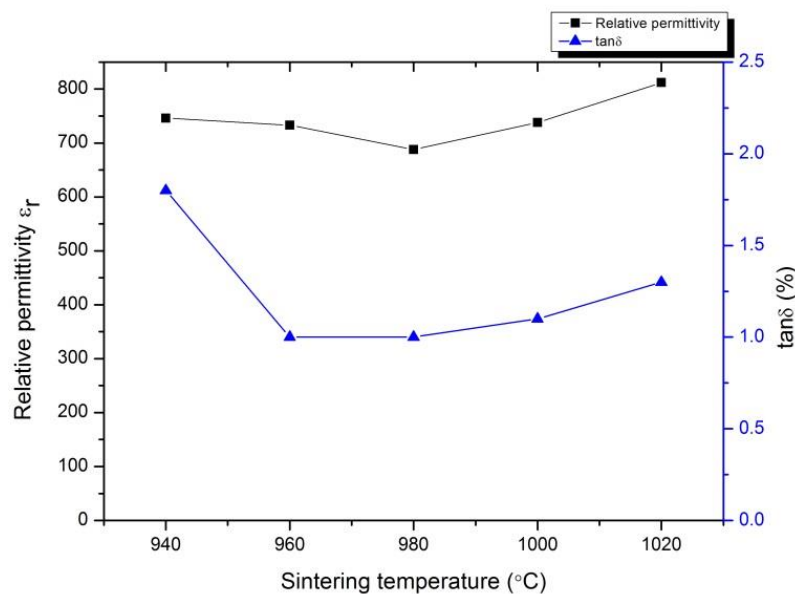


Figure 3.25 Dielectric properties of KNLN-NS-Cu/Ba-2.5 sintered at different temperature measured at 1 kHz.

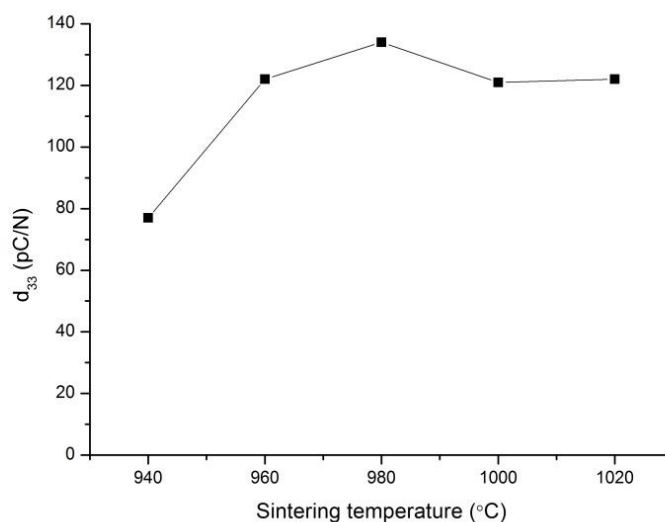


Figure 3.26 Piezoelectric properties of KNLN-NS-Cu/Ba-2.5 sintered at different temperature.

3.9 Summary

In this chapter, the KNLN-NS ceramics are prepared using HEBM and Cu/Ba sintering aid, respectively, with the aim of lowering the sintering temperature. Our results reveal that HEBM can promote uniform grain growth and reduce the grain size to about $\sim 1 \mu\text{m}$. However, the technique cannot lower the sintering temperature, so it may not be a good choice for lowering the sintering temperature of the KNLN-NS ceramics.

On the other hand, the Cu/Ba sintering aid is effective in lowering the sintering temperature of the KNLN-NS ceramics. In general, high densification, good dielectric and piezoelectric properties can be obtained in the KNLN-NS-Cu/Ba-x ceramics sintered at 1000°C for 8 h. For the ceramic with $x = 2.5$, $\epsilon_r = 688$, $\tan\delta = 1.0\%$ and $d_{33} = 134 \text{ pC/N}$. Our results also show that the dielectric and piezoelectric properties of the ceramics are stable with time. As the sintering temperature is lower than 1000°C , the



THE HONG KONG POLYTECHNIC UNIVERSITY

ceramic can be co-fired with a relatively cheap Pd/Ag (30/70) inner electrode. Therefore, together with the low $\tan\delta$ and high d_{33} , the ceramic is a promising candidate for practical applications, in particular for multilayered devices.



Chapter 4 Characterization of Piezoelectric

Gyro-sensors

4.1 Introduction

As discussed in Chapter 2, the piezoelectric vibratory gyro-sensor fabricated in this project is comprised of a stack of two ceramic plates that are poled in opposite direction as shown in Figure 2.11. The gyro-sensor is driven electrically to vibrate at its resonance frequency in the z-direction by applying an ac voltage to the bottom plate (Figure 2.12). As it bends upwards and downwards, positive and negative charges are generated, respectively, on the two top-electrodes of the top plate by the direct piezoelectric effect. Because of symmetry, the currents collected from the two top-electrodes are of the same magnitude and in phase. If the gyro-sensor is rotated about the x-axis, a Coriolis force is induced, exciting the stack to vibrate in the y-direction. As the stack has a square cross-section, the induced vibration is close to the corresponding resonance and hence has the optimum amplitude. When the stack vibrates in the y-direction, the two sides have different deformations, e.g., the left side contracts along the x-direction while the right side expands. Because of Poisson effect, the left side expands in the z-direction and the right side contracts. The charges or currents induced on the two top-electrodes hence become different, and the difference is proportional to the rotation speed. The induced currents on both electrodes are weak and the difference between them is extremely small. Charge amplifiers are then needed and should be located as close as possible to the rotating gyro-sensors. Moreover, our aim is to



THE HONG KONG POLYTECHNIC UNIVERSITY

develop a prototype of gyro-sensors that can be used in practical applications. Therefore, instead of using sophisticated equipment such as lock-in amplifiers, an electronic readout circuit (Figure 4.1) is developed in this project to detect, amplify and analyze the weak currents and then to output a dc voltage that is proportional to the rotation speed. It is expected that the electronic readout circuit can be further miniaturized to a small chip by the industries and become a small part of the gyro-sensor. As gyro-sensors of different dimensions and then different frequencies are fabricated and characterized, a function signal generator module (AD9851 DDS) is used in this project to drive the gyro-sensor to vibrate at its resonance frequency. Indeed, it can be easily replaced by some simple electronics if the operating frequency is fixed.

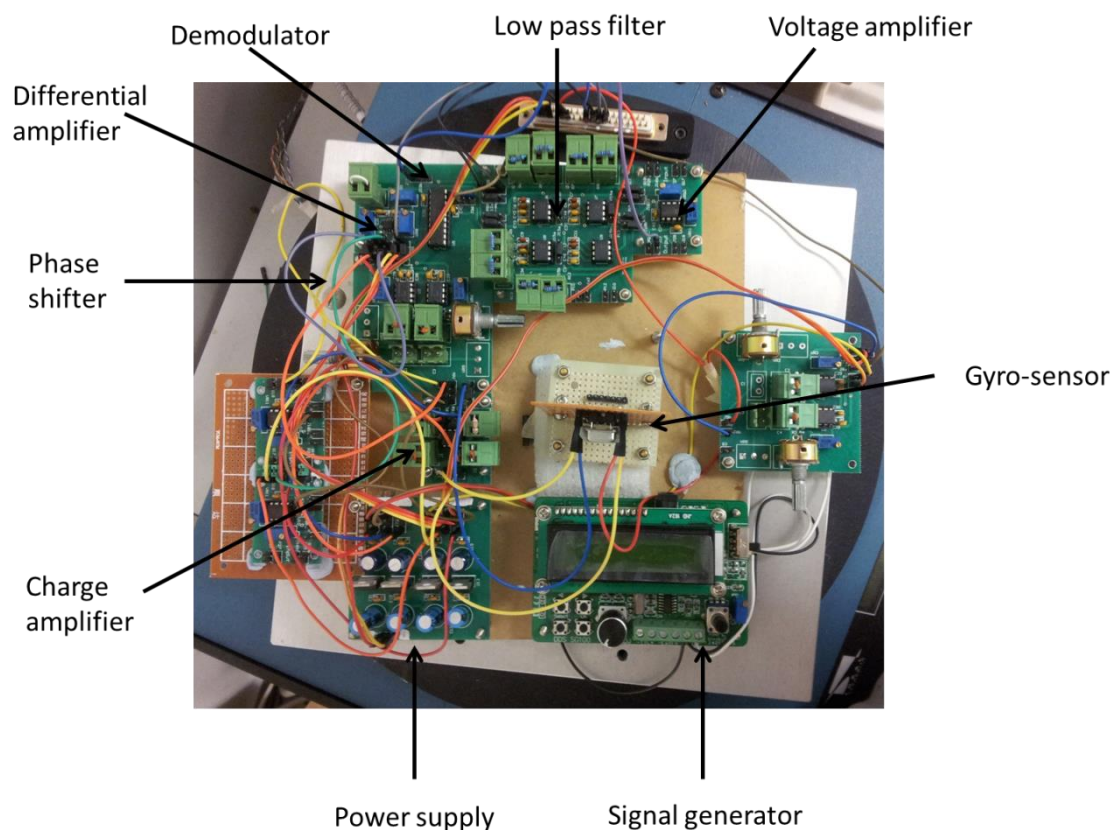


Figure 4.1 Photo of the readout circuit.

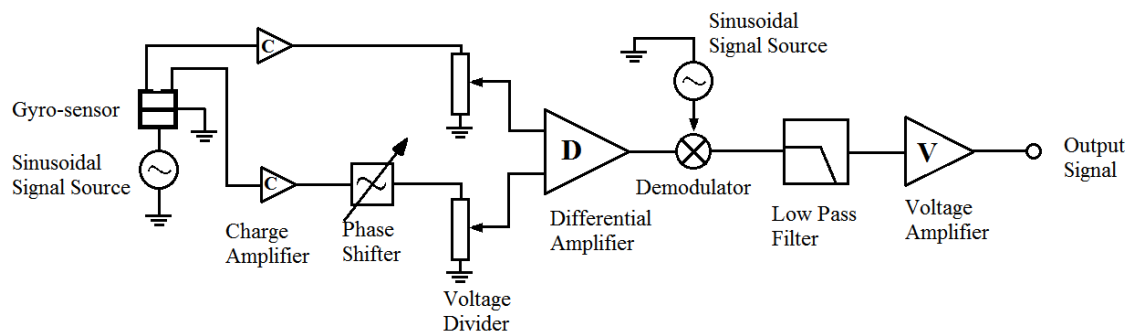


Figure 4.2 The block diagram of the readout circuit.

4.2 Electronic Readout Circuit

As illustrated in Figure 4.2, the electronic readout circuit is comprised of two charge amplifiers, a phase shifter, a differential amplifier, a demodulator, a low-pass filter and a voltage amplifier. As the induced currents are very weak, the selections of electronic components are pivotal for developing the readout circuit. An operational amplifier (AD823) with ultra-low input leakage and low input bias current is used for the charge amplifier. An instrumentation amplifier (AD8429) with high common mode rejection ratio (CMRR) is used for the differential amplifier to detect the difference between the currents collected and amplified from the two top-electrodes. A high CMRR is beneficial for enhancing the accuracy of the sensor outputs. The demodulation is implemented using a balanced modulator (AD630) by phase-sensitive demodulation with a signal generated from drive-mode oscillations. Low-noise operational amplifier (OP27) is used for both the phase shifter and 2-pole Butterworth low-pass. In order to



provide a sharp transition band at the cut-off frequency, an 8th-order low-pass filter is formed by cascading four 2-pole Butterworth low-pass filters. Finally, an instrumentation amplifier (AD620) is used for providing gain control and offset adjustment to calibrate the final DC output voltage.

4.2.1 Charge Amplifier

As discussed, the induced charges on the two top-electrodes of the vibrating gyro-sensor are weak, and charge amplifiers are needed to amplify and converted to voltage of certain magnitude for the subsequent processing. Operational amplifiers AD823 in negative feedback via a capacitor C_f (Figure 4.3) are used to convert the high-impedance charges collected from each top-electrode to low-impedance voltage. For a sufficiently high open-loop gain, the capacitances of the cables and gyro-sensor can be neglected and the output voltage depends only on the input charge V_o and feedback capacitance C_f as:

$$V_o = \frac{-q}{C_f} \quad (4.1)$$

The (lower) cut-off frequency f_c of the charge amplifier is given as:

$$f_{c1} = \frac{1}{2\pi R_1 C_f} \quad (4.2)$$

where R_1 is the resistance. Practically, f_{c1} must be much lower than the operating frequency (i.e. the resonance frequencies f_r) of the gyro-sensors.

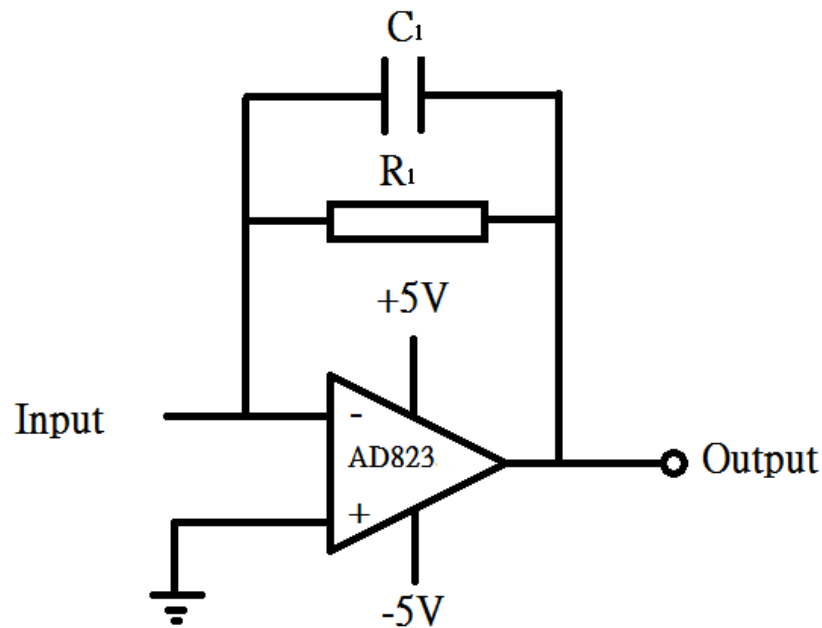


Figure 4.3 The circuit diagram of the charge amplifier.

4.2.2 Phase shifter

Ideally, the gyro-sensors should be symmetric about the central line, and thus the currents induced on the two top-electrodes of the vibrating (but not rotating) gyro-sensor are of the same amplitude and in phase. However, it is difficult to fabricate gyro-sensors with perfect symmetry and the detected and amplified signals may not be of the same amplitude and in phase. For example, the two top-electrodes may not be of the same dimensions. Therefore, a phase shifter is needed to adjust the phase of one of the signals to make them become in phase. In this project, the phase shift (Figure 4.4) is designed by connecting two phase shifters in series so as to achieve a maximum phase

shift of 360° . For each phase shifter, the phase shift θ is given as:

$$\theta = 2 \tan^{-1}(2\pi f_r C_2 VR_1) \tag{4.3}$$

If a maximum VR_1 of $100 \text{ k}\Omega$ is used, the phase shift is $\sim 180^\circ$. Therefore, for the two phase shifter connected in series, the maximum phase shift is $\sim 360^\circ$.

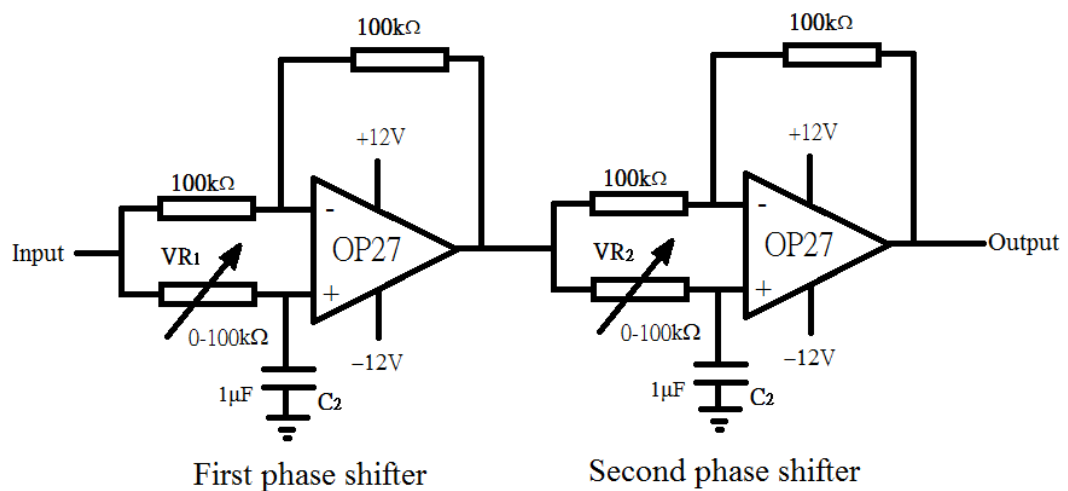


Figure 4.4 The circuit diagram of phase shifter.

4.2.3 Differential amplifier

An instrumentation amplifier AD8429 is used as a differential amplifier for detecting the small difference between the currents induced on the two top-electrodes (Figure 4.5). For a vibrating but not rotating gyro-sensor, these two currents should be of the same amplitude and in phase, and then the output of the amplifier is zero. To ensure a zero voltage output for a non-rotating gyro-sensor, the amplitudes of these two currents are adjusted to the same, via the potential dividers VR_3 and VR_4 , before feeding



into the amplitude. When the vibrating gyro-sensor rotates, these two currents become different, and the difference that is proportional to the rotation speed can be detected by the differential amplifier. The amplitude of the detected signal is amplified up to a factor of 20 by the variable resistor VR_5 .

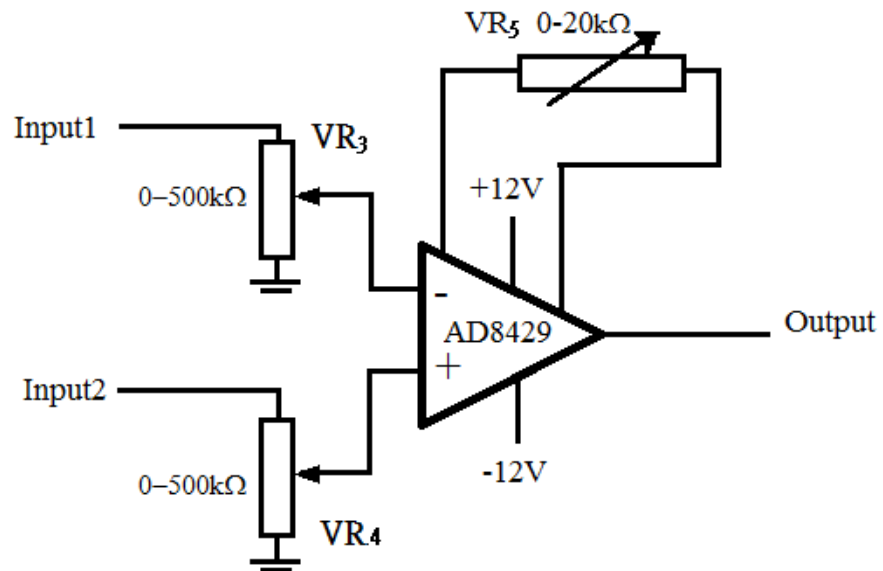


Figure 4.5 The circuit diagram of the differential amplifier.

4.2.4 Demodulator

A balanced modulator AD630 is used as a synchronous demodulator in this project (Figure 4.6). The signal output from the differential amplifier is demodulated synchronously using phase information derived from the sinusoidal signal source. The output signal of the demodulator is a baseband modulation signal, containing a DC component that is proportional to the rotation speed, and higher order carrier components that are removed with a low-pass filter.

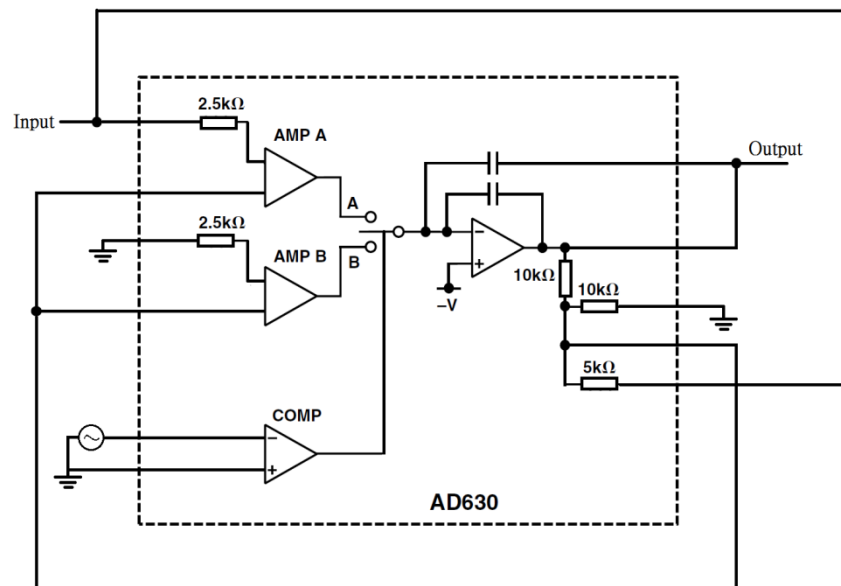


Figure 4.6 The circuit diagram of the demodulator.

4.2.5 Low Pass Filter

An 8th-order low-pass filter formed by cascading four identical 2-pole Butterworth low-pass filters is used to filter the higher order carrier components of the signal output from the demodulator. Low-noise operational amplifiers OP27 are used to form the basic 2-pole Butterworth low-pass filters, and each of them provides a roll-off of 40 dB/decade at the cut-off frequency. The cascaded low-pass filter then provides a sharp transition band with a 160 dB/decade roll-off at the cut-off frequency. The circuit diagram of the low-pass filter is shown in Figure 4.7. The cut-off frequency f_{c2} of the low-pass filter is calculated as:

$$f_r > f_{c2} = \frac{0.707}{2\pi R_2 C_3} \quad (4.4)$$

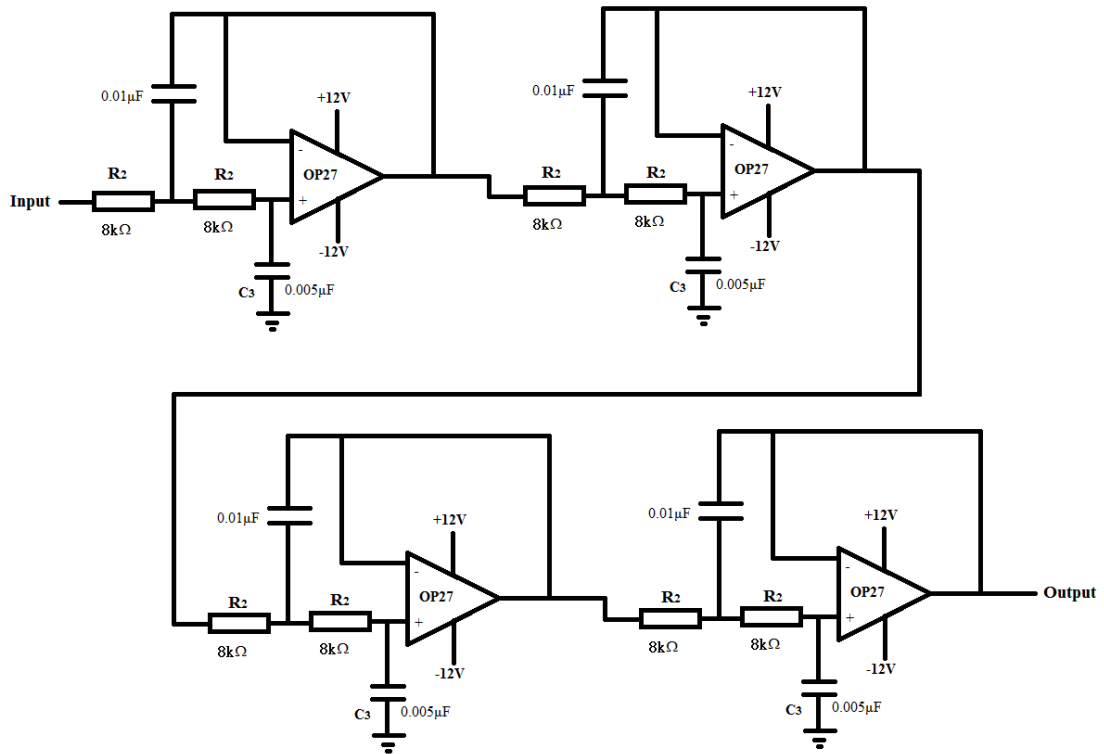


Figure 4.7 The circuit diagram of the low pass filter.

4.2.6 Voltage amplifier

The last part of the readout circuit is a voltage amplifier (Figure 4.8) formed by an instrumentation amplifier (AD620). After the demodulator and low-pass filters, a dc voltage offset may exist in the output signal even for a vibrating but not rotating gyro-sensor. Such an offset is eliminated by adjusting the potential divider VR₆. The voltage amplifier also provides an amplification factor up to 1000, via the adjustment of variable resistor VR₇.

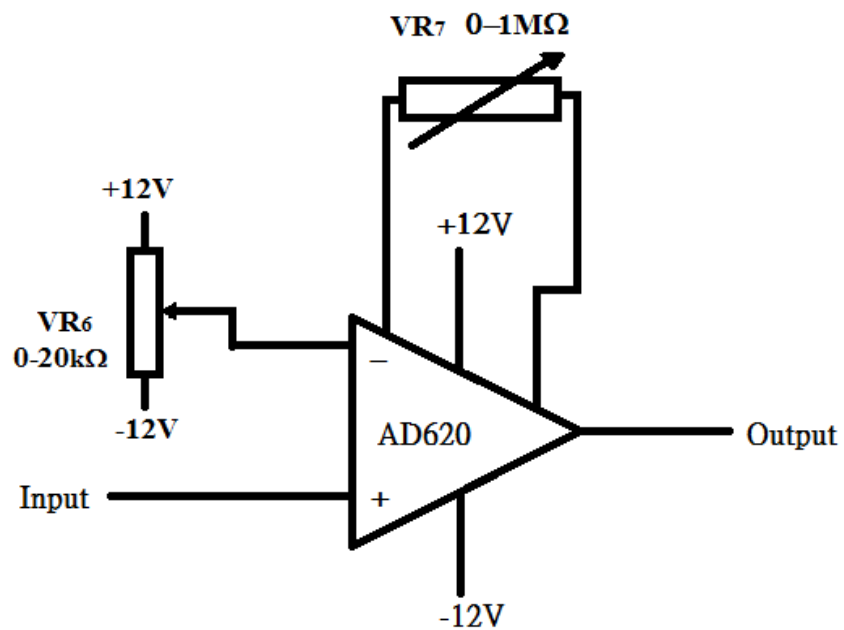


Figure 4.8 The circuit diagram of the voltage amplifier.

4.3 Results and Discussion

4.3.1 KNLN-NS Ceramic Gyro-sensors

KNLN-NS piezoelectric ceramics (i.e., prepared by the conventional method without using high-energy ball milling and sintering aids) are first used to fabricate the bimorph-type piezoelectric vibratory gyro-sensor (Figure 4.9). The ceramics are sintered at 1080°C and exhibit the optimum dielectric and piezoelectric properties: $\epsilon_r = 1530$, $\tan\delta = 2.4\%$ and $d_{33} = 240$ pC/N. To obtain the optimum sensitivity, the width and the thickness of the bimorph beam are set as the same, i.e., 1 mm or 0.6 mm. Gyro-sensors with different lengths (i.e., the length of the vibrating beam 9mm) are fabricated



THE HONG KONG POLYTECHNIC UNIVERSITY

so as to study the relationships between the dimensions, operating frequency and sensitivity. The ceramic gyro-sensors are glued on a holder using epoxy and electrically connected to the pins of the holder for the characterization (Figure 4.10).

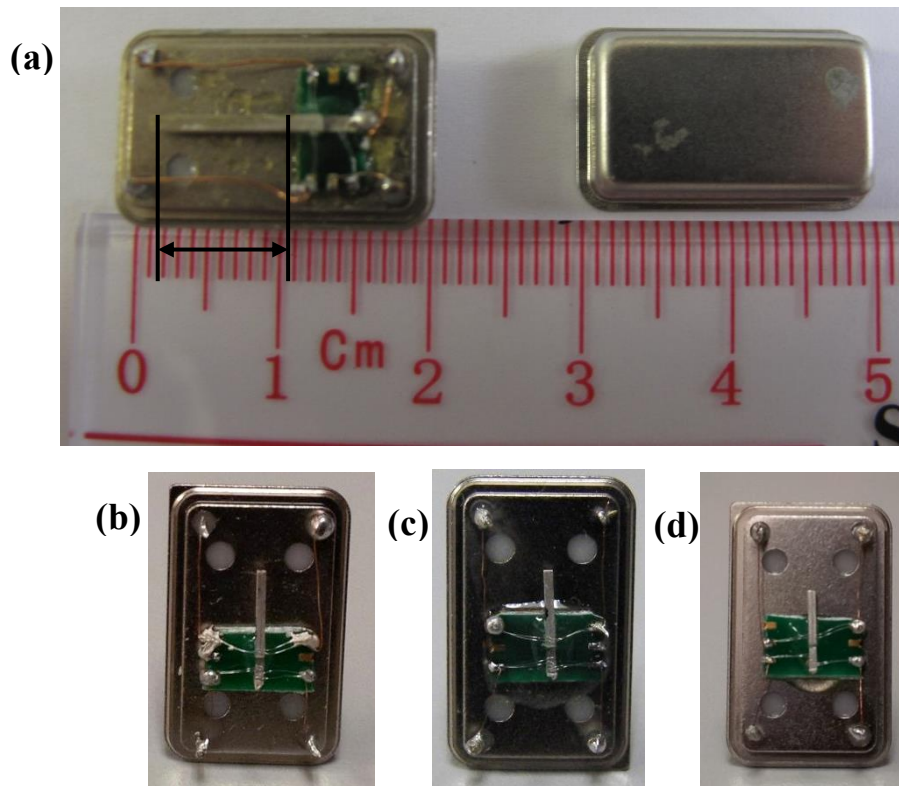


Figure 4.9 Photo of KNLN-NS gyro-sensors with the dimension of: (a) $1\text{mm} \times 9\text{mm}$, (b) $0.6\text{mm} \times 4\text{mm}$, (c) $0.6\text{mm} \times 3\text{mm}$, (d) $0.6\text{mm} \times 2\text{mm}$.

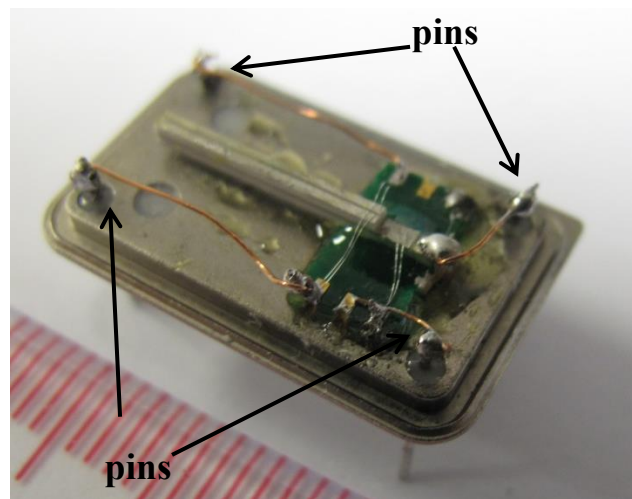


Figure 4.10 Photo depicting the connections of gyro-sensor.

Before measuring the sensitivity of the gyro-sensors, their resonance characteristics are studied. Figure 4.11 shows the resonance characteristics of the gyro-sensors with different dimensions, while Table 4.1 summarizes their resonance frequencies. The frequency at which the impedance reaches a minimum value is considered as the resonance frequency. As shown in Table 4.1, the gyro-sensor with a longer vibrating beam exhibits a lower resonance frequency. For a cantilever with one fixed end, the resonance frequency is given as [104]:

$$f_o = \frac{3.516}{2\pi} \times \sqrt{\frac{Y}{16\rho}} \times \frac{t}{L^2} \quad (4.5)$$

where f_o is the fundamental resonance frequency, Y is the Young's modulus, ρ is the density, t is the thickness and L is the length. By using $Y = 104$ GPa (for KNN) and the observed density for the KNLN-NS ceramics (Table 4.1), the resonance frequencies of the gyro-sensors are estimated and compared in Table 4.1. It can be seen that reasonably good agreement is obtained only for the gyro-sensor with a 9-mm vibrating beam. For the other gyro-sensors, the calculated resonance frequency is considerably higher than



THE HONG KONG POLYTECHNIC UNIVERSITY

the measured value. This should be partly due to the experimental errors in measuring the dimensions of the gyro-sensors, in particular for the length. As the gyro-sensor is glued on the holder manually using epoxy, there may exist a larger error in the length of the vibrating beam, and the error apparently becomes larger for shorter vibrating beams. Moreover, the error may also stem from the clamping condition of the vibrating beam (i.e., cantilever). As the gyro-sensor is simply glued on the holder using epoxy, the clamping may not be as tight as a fixed end. As a result, the vibrating part may be longer than that protruding from the holder (Figure 4.9) and the resonance frequency may then be lower. Again, the difference should be more significant for shorter beams.

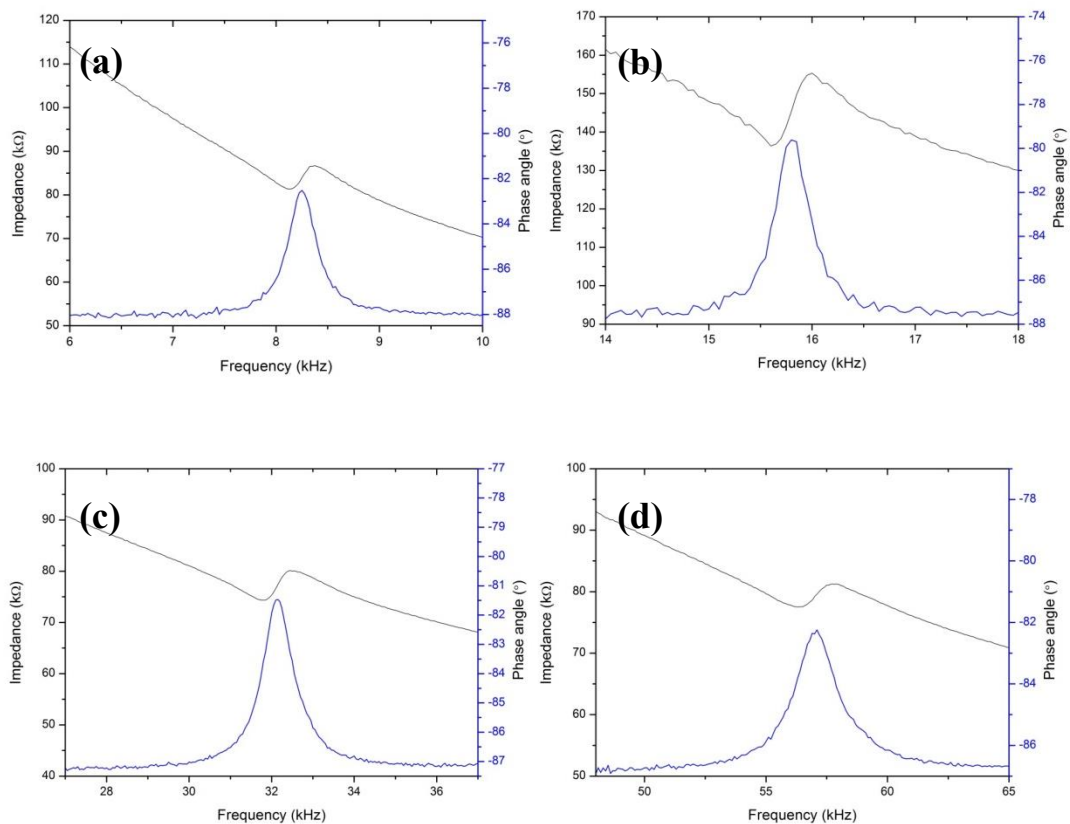


Figure 4.11 Impedance and phase spectra of the KNLN-NS gyro-sensors with the dimension of (a)

1 mm × 9 mm, (b) 0.6 mm × 4 mm, (c) 0.6 mm × 3 mm, (d) 0.6 mm × 2 mm.



Table 4.1 Characteristic of the KNLN-NS gyro-sensors.

Material	KNLN-NS			
Dimension				
Width/thickness (mm)	1	0.6	0.6	0.6
Length (mm)	9	4	3	2
Resonance frequency (kHz)				
Measured value	8.13	15.60	31.85	56.40
Calculated value	9.75	29.62	52.66	118.48
Sensitivity (mV/dps)	1.4	1.1	0.3	0.1
ρ (g/cm ³)	4.35			
ϵ_r	1530			
$\tan\delta$ (%)	2.4			
d_{33} (pC/N)	240			

The performances of the gyro-sensors are then characterized by driving at their resonance frequencies (Figure 4.12). The amplitude of the driving voltage is set at 5 V for all the gyro-sensors. A single-axis rate table (1270VS, Ideal Aerosmith) is used to provide a precise and stable rotation with a speed ranging from 0 to ± 360 dps. The electronic readout circuit is powered with ± 5 V and ± 12 V, and the dc output signal is recorded using a digital oscilloscope (RIGOL DS1052E). A steady dc output is obtained for all the gyro-sensors rotated at any speed in the range studied. The variations of the dc output voltage with the rotation speed for the gyro-sensors are shown in Figure 4.13. It can be seen that a linear relationship between the dc output voltage and rotation speed is obtained for all the gyro-sensors. The sensitivities of the gyro-sensors calculated from the slope of the curves are summarized in Table 4.1. In general, gyro-sensors with a longer vibrating beam (e.g., ~ 9 mm and ~ 4 mm) exhibit a higher sensitivity. A longer



THE HONG KONG POLYTECHNIC UNIVERSITY

vibrating beam generates a larger amplitude and can also be displaced more and easier by the induced Coriolis force. A longer vibrating beam also has larger electrodes and hence the induced charges are more and the current is larger. It should be noted that the observed dc output voltage is optimized via adjusting the parameters of the readout circuit, and the amplification factor may not be the same for all the gyro-sensors. For the gyro-sensors commonly used in the market, the sensitivity is typically about 0.5 mV/dps [105]. As shown in Table 4.1, the gyro-sensor with a 4-mm long and 0.6-mm thick vibrating beam has a good compromise between the size and sensitivity, suggesting that it is a promising miniaturized gyro-sensor for practical applications.

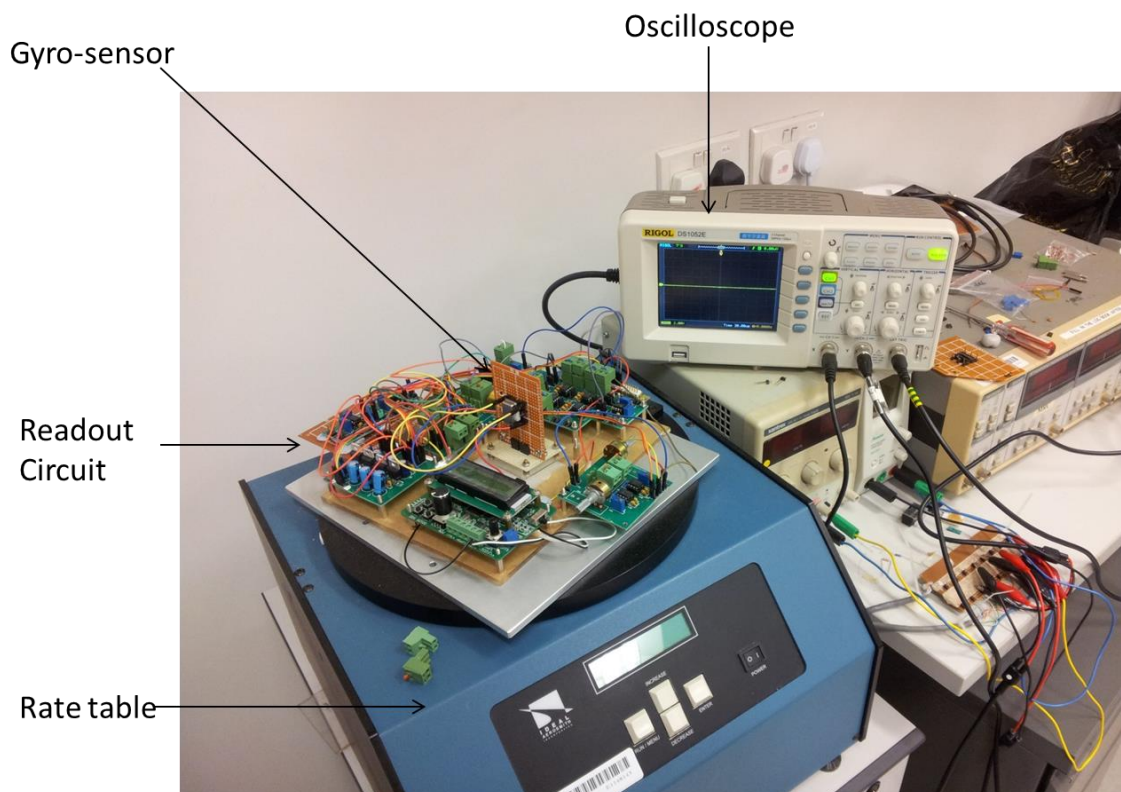


Figure 4.12 Experiment setup for gyro-sensor output measurement.

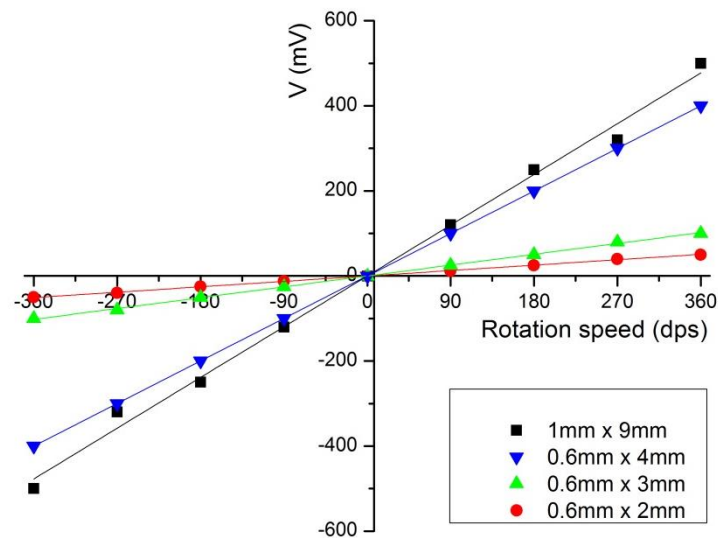


Figure 4.13 The output voltage against rotation speed curves of different KNLN-NS gyro-sensors.

4.3.2 KNLN-NS-Cu/Ba Ceramic Gyro-sensors

The low-temperature sintered KNLN-NS-Cu/Ba-1.25 and KNLN-NS-Cu/Ba-2.5 ceramics have also been used to fabricate the bimorph-type piezoelectric vibratory gyro-sensors with a 3.5-mm long vibrating beam (Figure 4.14). The dielectric and piezoelectric properties of the ceramics are summarized in Table 4.2 for reference. The resonance characteristics of the gyro-sensors are shown in Figure 4.15. It can be seen that, in spite of the high dielectric loss ($\tan\delta = 18\%$) at 1 kHz, the KNLN-NS-Cu/Ba-1.25 ceramic gyro-sensor exhibit a weak resonance at ~ 23 kHz. The variation of $\tan\delta$ with frequency for the KNLN-NS-Cu/Ba-1.25 ceramic is shown in Figure 4.16. At high frequency, e.g., 20 kHz, the observed $\tan\delta$ for the ceramics become small, generally $< 7\%$. Our results then suggest that the high dielectric loss arisen from moisture absorption may not affect the applications of the ceramics, in particular when high frequencies are involved. Because of the weaker piezoelectric properties, the resonance



THE HONG KONG POLYTECHNIC UNIVERSITY

peaks of the gyro-sensors are weaker than those fabricated using the KNLN-NS ceramics (sintered at 1080°C) (Figure 4.9). Due to the larger thickness (0.68 mm), the resonance frequency of the gyro-sensor fabricated using the KNLN-NS-Cu/Ba-2.5 ceramic increases to about 33 kHz. On the other hand, probably due to the non-dense structure and then smaller elastic modulus, the gyro-sensor fabricated using the KNLN-NS-Cu/Ba-1.25 ceramic exhibits a lower resonance frequency (23 kHz). By using equation 4.5, the resonance frequencies of the gyro-sensors are estimated and compared in Table 4.2. Similarly, because of the experimental errors and non-fixed clamping, the calculated resonance frequencies are higher than the measured ones.

Table 4.2 Characteristic of the KNLN-NS-Cu/Ba gyro-sensors

Material	KNLN-NS-Cu/Ba-1.25	KNLN-NS-Cu/Ba-2.5
Dimension		
Width/thickness (mm)	0.62	0.68
Length (mm)	3.5	3.5
Resonance frequency (kHz)		
Measured value	23.4	32.85
Calculated value	40.35	43.44
Sensitivity (mV/dps)	0.8	0.6
ρ (g/cm ³)	4.27	4.43
ϵ_r	585	738
$\tan\delta$ (%)	18	1.3
d_{33} (pC/N)	153	121

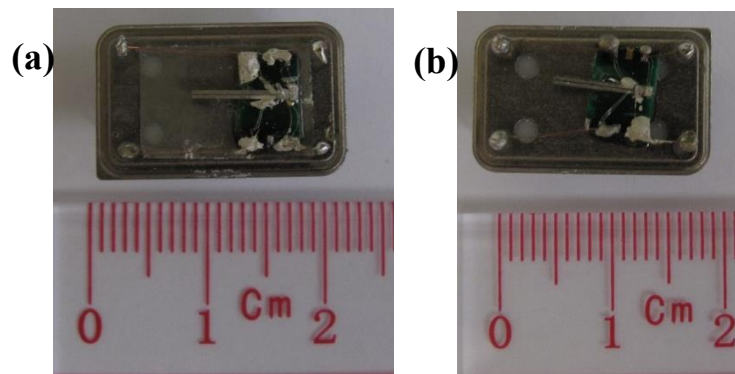


Figure 4.14 Photo KNLN-NS-Cu/Ba-x gyro-sensors: (a) $x = 1.25$ and (b) $x = 2.5$.

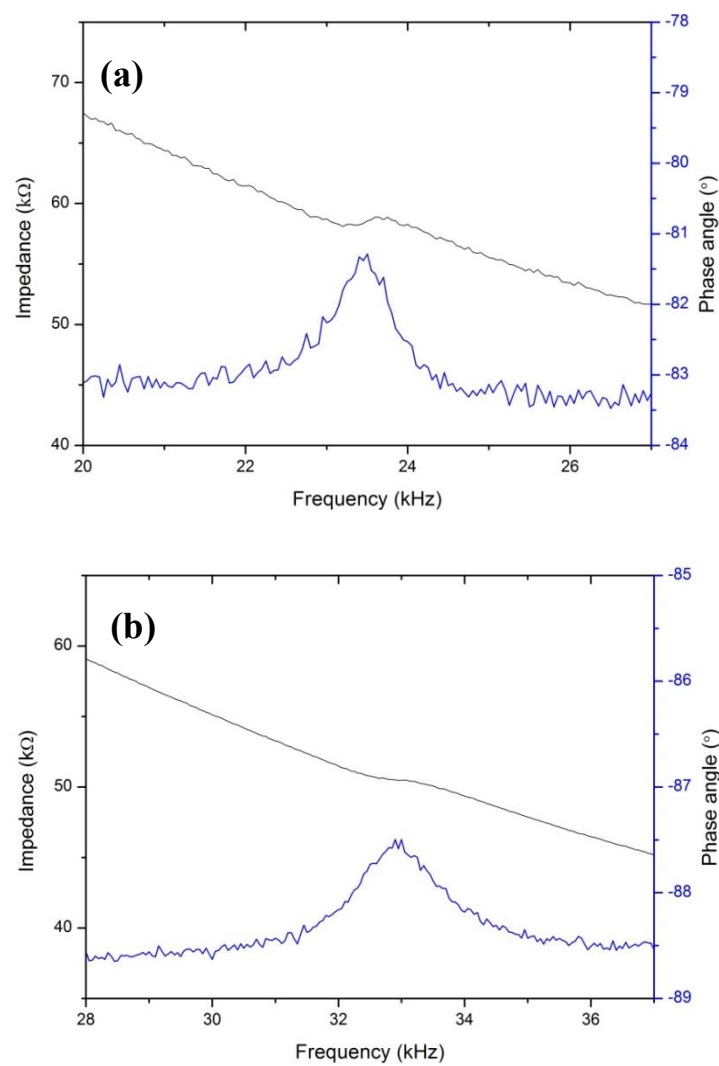


Figure 4.15 Impedance and phase spectra of the KNLN-NS-Cu/Ba-x gyro-sensors: (a) $x = 1.25$ and (b) $x = 2.5$.

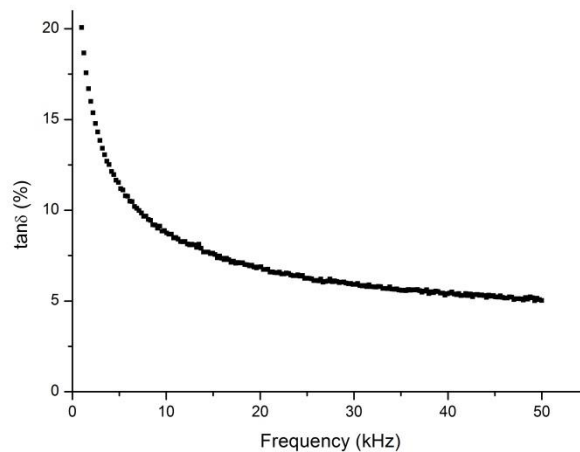


Figure 4.16 The $\tan\delta$ spectrum of KNLN-NS-Cu/Ba-1.25 ceramics.

Although the low-temperature sintered ceramics have weaker piezoelectric properties (Table 4.2), the gyro-sensors also exhibit a linear relationship between the output dc voltage and rotation speed (Figure 4.17). It is also interesting to note that the sensitivities of these gyro-sensors are comparable to those fabricated using the ceramics sintered at higher temperatures (Table 4.1). This suggests that, in spite of the relatively weak piezoelectric properties, the low-temperature sintered KNLN-NS-Cu/Ba ceramics can be used for practical applications, especially for multilayered devices, such as piezoelectric vibratory gyro-sensors.

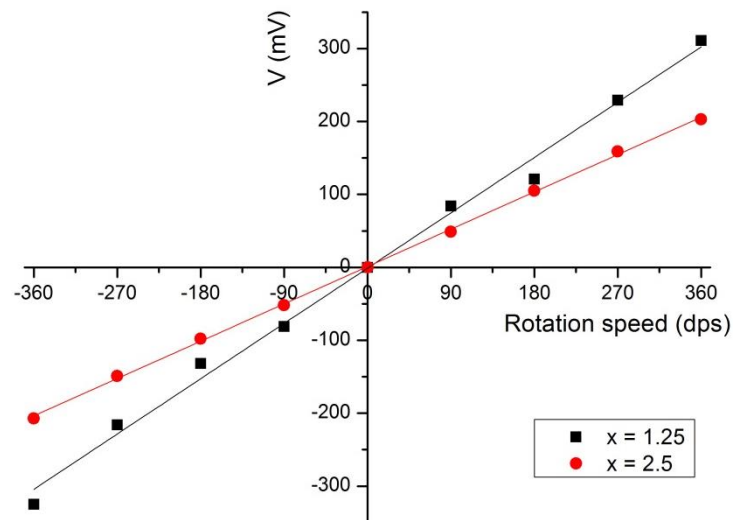


Figure 4.17 The output voltage against rotation speed curves of KNLN-NS-Cu/Ba-x piezoelectric gyro-sensors.

4.4 Summary

In this chapter, an electronic readout circuit has been developed for the piezoelectric ceramic vibratory gyro-sensors. The readout circuit has successfully detected a small difference in charges induced in the gyro-sensors subjected to a rotation ranging from 0 to 360 dps. The gyro-sensors fabricated using both the high-temperature sintered KNLN-NS and low-temperature sintered KNLN-NS-Cu/Ba ceramics have been characterized. All the gyro-sensors exhibit a linear relationship between the dc output voltage and rotation speed. Owing to the ease and larger amplitude of vibration, gyro-sensors with longer vibrating beam exhibit a higher sensitivity. Nevertheless, a high sensitivity of 1.1 mV/dps can be obtained in gyro-sensors of size as small as 4 mm x 0.6 mm x 0.6 mm. Although the piezoelectric properties are weak, the gyro-sensor fabricated using the KNLN-NS-Cu/Ba ceramics also possess a good sensitivity (0.57-0.84 mV/dps) that is comparable to the one



THE HONG KONG POLYTECHNIC UNIVERSITY

fabricated using the high-temperature sintered ceramics. It is also recommended that further research be undertaken in the reliabilities study, such as endurance, vibration and applied bias stabilities of gyro-sensor. Our results also show that the high dielectric loss ($\tan\delta = 18\%$) at 1 kHz of the ceramic arisen from moisture absorption does not affect the performance of gyro-sensors. On the basis of the results, it can be concluded that the low-temperature sintered KNLN-NS-Cu/Ba ceramics can be used for practical applications, in particular for multilayered devices such as piezoelectric vibratory gyro-sensors.



Chapter 5 Conclusions

In this project, lead-free piezoelectric ceramics $0.91\text{K}_{0.47}\text{Na}_{0.47}\text{Li}_{0.06}\text{NbO}_3-0.09\text{NaSbO}_3$ (KNLN-NS) ceramics have been prepared using high-energy ball milling (HEBM) or sintering aid (a complex of Cu/Ba in a molar ratio of 71.5/28.5), respectively, with the aim of lowering the sintering temperature. The dielectric, piezoelectric and ferroelectric properties of the ceramics have been investigated in detail, and the optimum processing and sintering conditions have been determined. The ceramics have then been used to fabricate bimorph-type piezoelectric vibratory gyro-sensors, and their performances have been evaluated in detail using an electronic readout circuit.

Although the HEBM technique can promote uniform grain growth and reduce the grain size, it cannot lower the sintering temperature of the ceramics. On the other hand, the Cu/Ba sintering aid is effective in lowering the sintering temperature of the KNLN-NS ceramics. High densification, good dielectric and piezoelectric properties are generally obtained in the KNLN-NS-Cu/Ba-x ceramics (i.e. KNLN-NS ceramics added with x wt% of the Cu//Ba sintering aid) sintered at 1000°C for 8 h. For the KNLN-NS-Cu/Ba-2.5 ceramics, the dielectric and piezoelectric properties become optimum, giving $\epsilon_r = 688$, $\tan\delta = 1.0\%$ and $d_{33} = 134$ pC/N. If less sintering aid is used, the ceramics become porous, the density decreases and the dielectric loss at low frequencies is sensitive to moisture. However, similar to the KNLN-NS-Cu/Ba-2.5 ceramic, the ceramics can be effectively poled at high temperatures and exhibit good and stable piezoelectric properties. As the sintering temperature is lower than 1000°C , the ceramics can be co-fired with a relatively cheap Pd/Ag (30/70) inner electrode.



THE HONG KONG POLYTECHNIC UNIVERSITY

Therefore, together with the low $\tan\delta$ and high d_{33} , the ceramics are promising candidates for practical applications, in particular for multi-layered devices.

Both the KNLN-NS ceramics (sintered at 1080°C) and KNLN-NS-Cu/Ba ceramics (sintered at 1000°C) have been used to fabricate bimorph-type vibratory gyro-sensors, and their performance has been evaluated. An electronic readout circuit comprising of charge amplifiers, differential amplifiers and demodulator has been developed to detect the small signals induced in the gyro-sensors subjected to a rotation ranging from 0 to 360 dps. The gyro-sensor consists of a stack of two oppositely poled ceramic plates and is electrically driven to vibrate at its bending resonance frequency. Subjected to a rotation, a Coriolis force is induced, bending it in a direction normal to both the vibrating and rotation directions. The charges induced on the gyro-sensor by the induced bending are detected and a dc output voltage is given by the electronic readout circuit. All the gyro-sensors exhibit a linear relationship between the dc output voltage and rotation speed. Our results also show that the high dielectric loss at low frequencies of the KNLN-NS-Cu/Ba ceramic arisen from moisture absorption does not affect the performance of gyro-sensors that operated at high frequencies such as 20-30 kHz. A good compromise between the dimension and sensitivity is obtained for a gyro-sensor of size 4 mm × 0.6 mm × 0.6 mm. The sensitivity of such a gyro-sensor fabricated using the KNLN-NS-Cu/Ba ceramic reaches a high value of 0.57-0.84 mV/dps in the range of -360 dps to +360 dps. On the basis of the results, it can be concluded that the low-temperature sintered KNLN-NS-Cu/Ba ceramics can be used for practical applications, in particular for multilayered devices such as piezoelectric vibratory gyro-sensors.



References

- [1] C. Z. Rosen, B. V. Hires, and R. Newnham, *Key papers in physics piezoelectricity*. New York: American Institute of Physics, 1992.
- [2] K. Uchino, *Ferroelectric devices*, 2nd ed. New York: CRC Press, 2009.
- [3] B. Jaffe, W. R. Cook, and H. Jaffe, *Piezoelectric ceramics*. New York: Academic Press, 1971.
- [4] S. E. Park and T. R. Shrout, "Ultrahigh strain and piezoelectric behavior in relaxor based ferroelectric single crystals," *J. Appl. Phys.*, vol. 82, no. 4, pp. 1804-1811, 1997.
- [5] A. et al Herklotz, "Electrical characterization of PMN-28%PT(001) crystals used as thin-film substrates," *J. Appl. Phys.*, vol. 108, no. 9, p. 094101, 2010.
- [6] C. W. et al Ahn, "Effect of elemental diffusion on temperature coefficient of piezoelectric properties in KNN-based lead-free composites," *J. Mater. Sci. Lett.*, vol. 45, no. 14, pp. 3961-3965, 2010.
- [7] R. E. Jaeger and I. Egerton, "Hot Pressing of Potassium-Sodium Niobates," *J. Am. Ceram. Soc.*, vol. 45, no. 5, pp. 209-213, 1962.
- [8] L. Egerton and D. M. Dillom, "Piezoelectric and Dielectric Properties of Ceramics in the System Potassium-Sodium Niobate," *J. Am. Ceram. Soc.*, vol. 42, no. 9, pp. 438-442, 1959.
- [9] C. W. Ahn, "Effect of MnO₂ on the Piezoelectric Properties of (1-x)(Na_{0.5}K_{0.5})NbO₃-xBaTiO₃ Ceramics," *Jpn. J. Appl. Phys.*, vol. 44, no. 44, pp. L1361-L1364, 2005.
- [10] Y. Guo, K. Kakimoto, and H. Ohsato, "Phase Transitional Behavior and Piezoelectric Properties of (Na_{0.5}K_{0.5})NbO₃-LiNbO₃ Ceramics," *Appl. Phys. Lett.*, vol. 85, no. 18, pp. 4121-4123, 2004.
- [11] R. Wang et al., "Phase Diagram and Enhanced Piezoelectricity in the Strontium Titanate Doped Potassium-Sodium Niobate Solid Solution," *Phys. Stat. Sol. (A)*, vol. 202, no. 6, pp. R57-R59, 2005.
- [12] Y. Guo, K. Kakimoto, and H. Ohsato, "(Na_{0.5}K_{0.5})NbO₃-LiTaO₃ Lead-Free



THE HONG KONG POLYTECHNIC UNIVERSITY

- Piezoelectric Ceramics," *Mater. Lett.*, vol. 59, no. 2-3, pp. 241-244, 2005.
- [13] J. F. Li, K. Wang, B. P. Zhang, and L. M. Zhang, "Ferroelectric and piezoelectric properties of fine-grained $\text{Na}_{0.5}\text{K}_{0.5}\text{NbO}_3$ lead-free piezoelectric ceramics prepared by spark plasma sintering," *J. Am. Ceram. Soc.*, vol. 89, no. 2, p. 706, 2006.
- [14] D. Lin and K. W. Kwok, "Piezoelectric Properties of $\text{K}_{0.47}\text{Na}_{0.47}\text{Li}_{0.06}\text{NbO}_3\text{-NaSbO}_3$ Lead-Free Ceramics for Ultrasonic Transducer Applications," *Int. J. Appl. Ceram. Technol.*, vol. 8, no. 3, pp. 684-690, 2011.
- [15] J. Curie and P. Curie, *C. R. Acad. Sci.*, vol. 91, p. 294, 1880.
- [16] M. G. Lippmann, *Ann Chimie et Phys.*, vol. 24, p. 145, 1881.
- [17] Gene H. Haertling, "Ferroelectric Ceramics: History and Technology," *J. Am. Ceram. Soc.*, vol. 4, no. 82, pp. 797-818, 1999.
- [18] T. Mitsui, *An Introduction To The Physics of Ferroelectrics*. London: GORDON AND BREACH SCIENCE PUBLISHERS LTD., 1976.
- [19] D. F. Waechter, S. E. Prasad, R. G. Blacow, and B. Yan, "Internally Biased PZT materials for high-power sonar transducers," *11th Cf/DrDC international Meeting on Naval Applications of Materials Technology*, pp. 223-232, 2005.
- [20] H. Kara, R. Ramesh, R. Stevens, and C. R. Bowen, "Porous PZT Ceramics for Receiving Transducers," *IEEE Transactions on Ultrasonics, Ferroelectrics, and Frequency Control*, vol. 50, no. 3, pp. 289-296, 2003.
- [21] A. Parent, O. L. Traon, S. Masson, and B. L. Foulgoc, "Design and Performance of a PZT Coriolis Vibrating Gyro (CVG)," *Applications of ferroelectrics, 2006. isaf'06 15th ieee international symposium on the. IEEE*, pp. 216-219, 2006.
- [22] R. A. Goyer and B. C. Rhyne, "Pathological effects of lead," *Int. Rev. Exp. Pathol.*, vol. 12, 1973.
- [23] G. Shirane, R. Newnham, and R. Pepinsky, "Dielectric properties and phase transition of NaNbO_3 and $(\text{Na,K})\text{NbO}_3$," *Phys. Rev.*, vol. 96, no. 3, pp. 581-588, 1954.
- [24] R. Z. Zuo, J. Rodel, R. Z. Chen, and L. T. Li, "Sintering and electrical properties of lead-free $\text{Na}_{0.5}\text{K}_{0.5}\text{NbO}_3$ piezoelectric ceramics," *J. Am. Ceram. Soc.*, vol.



THE HONG KONG POLYTECHNIC UNIVERSITY

- 89, no. 6, p. 2010, 2006.
- [25] Y. Guo, K. Kakimoto, and H. Ohsato, "Dielectric and piezoelectric properties of lead-free (Na_{0.5}K_{0.5})NbO₃-SrTiO₃ ceramics," *Sol. State Comm.*, vol. 129, p. 279, 2004.
- [26] Y. Guo, K. Kakimoto, and H. Ohsato, "Structure and electrical properties of lead-free (Na_{0.5}K_{0.5})NbO₃-BaTiO₃ ceramics," *Jpn. J. Appl. Phys. PART 1-REGULAR PAPERS SHORT NOTES & REVIEW PAPERS*, vol. 43, no. 9B, p. 6662, 2004.
- [27] D. Lin, K. W. Kwok, and H. L. W. Chan, "Microstructure, Phase Transition and Electrical Properties of (K_{0.5}Na_{0.5})_{1-x}Li_x(Nb_{1-y}Ta_y)O₃ Lead-Free Piezoelectric Ceramics," *J. Appl. Phys.*, vol. 102, p. 034102, 2007.
- [28] V. B. Nalbandyan, M. Avdeev, and A. A. Pospelov, "Ion Exchange Reactions of NaSbO₃ and Morphotropic Series MSbO₃," *Solid State Sci.*, vol. 8, pp. 1430-1437, 2006.
- [29] "Piezoelectric Material Specifications Table," Piezo Technologies, 2012.
- [30] A.J. Bell, "Ferroelectrics: The Role of Ceramic Science and Engineering.," *J. Eur. Ceram. Soc.*, vol. 28, no. 7, pp. 1307-1317, 2008.
- [31] N. Setter and R. Waser, "Electroceramic Materials," *Acta materialia*, vol. 48, no. 1, pp. 151-178, 2000.
- [32] T. Kokubo and M. Tashiro, "Dielectric Properties of Fine-Grained PbTiO₃ Crystals Precipitated in a Glass," *J. Non-Cryst. Solids*, vol. 13, no. 2, pp. 328-40, 1973.
- [33] G. H. Beall, B. Flats, and L. R. Pinckney, "US Patent," 5491116, Feb. 13, 1996.
- [34] H. Cai, Z. Cui, and L. Li, "Low-sintering Composite Multilayer Ceramic Capacitors with X7R Specification," *Mater. Sci. Eng. B*, vol. 83, no. 1, pp. 137-141, 2001.
- [35] R. E. Newnham, L. J. Bowen, K. A. Klicker, and L. E. Cross, "Composite Piezoelectric Transducers," *Materials & Design*, vol. 2, no. 2, pp. 93-106, 1980.
- [36] W. H. Yang, S. H. Yu, R. Sun, and R. X. Du, "Nano- and Microsize effect of CCTO Fillers on the Dielectric Behavior of CCTO/PVDF Composites," *Acta Materialia*, vol. 59, no. 14, pp. 5593-5602, 2011.



THE HONG KONG POLYTECHNIC UNIVERSITY

- [37] PFISTERER. [Online]. <http://www.pfisterer.com>
- [38] G. R. Ruschau, R. E. Newnham, J. Runt, and B. E. Smith, "0-3 Ceramic/Polymer Composite Chemical Sensors," *Sensors and Actuators*, vol. 20, no. 3, pp. 269-275, 1989.
- [39] G. Alrt and etl.al., "Dielectric properties of fine-grained barium titanate ceramics," *J. Appl. Phys.*, vol. 58, no. 4, pp. 1619-25, 1985.
- [40] E.E. Oren, E. Taspinar, and A.C. Tas, "Preparation of lead zirconate by homogeneous precipitation and calcinations," *J. Am. Ceram. Soc.*, vol. 80, no. 10, pp. 2714-6, 1997.
- [41] S. Kim, M. Jun, and S. Hwang, "Preparation of undoped lead titanate ceramics via sol-gel processing," *J. Am. Ceram. Soc.*, vol. 82, no. 2, pp. 289-96, 1999.
- [42] G.H. Haertling and C.E. Land, "Recent improvements in the optical and electrooptic properties of PLZT ceramics," *Ferroelectrics*, vol. 3, pp. 269-80, 1972.
- [43] Snow GS., "Improvements in atmosphere sintering of transparent PLZT ceramics," *J. Am. Ceram. Soc.*, vol. 56, no. 9, pp. 479-80, 1973.
- [44] D.M. Ibrahim and H.W. Hennicke, "Preparation of lead zirconate by a sol-gel method," *Trans. J. Br. Ceram. Soc.*, vol. 80, pp. 18-22, 1981.
- [45] S. Sato, T. Murakata, H. Yanagi, and F. Miyasaka, "Hydrothermal synthesis of fine perovskite PbTiO_3 powder with a simple mode of size distribution," *J. Mater. Sci.*, vol. 29, pp. 5657-63, 1994.
- [46] B.G. Muralidharan, A. Sengupta, G.S. Rao, and D.C. Agrawal, "Powders of $\text{Pb}(\text{Zr}_x\text{Ti}_{1-x})\text{O}_3$ by sol-gel coating of PbO ," *J. Mater. Sci.*, vol. 30, pp. 3231-7, 1995.
- [47] L. B. Kong, W. Zhu, and O. K. Tan, "Preparation and characterization of $\text{Pb}(\text{Zr}_{0.52}\text{Ti}_{0.48})\text{O}_3$ ceramics from high-energy ball milling powders," *Mater. Lett.*, vol. 42, pp. 232-239, 2000.
- [48] Y. Leyet-Ruiz, "Preparation and characterization of PZT nanopowder using high energy ball milling," *Revista cubana de Quimica*, vol. 21, no. 3, pp. 15-24, 2009.
- [49] E. Gaffet, D. Michel, L. Mazerolles, and P. Betthet, "Effects of high-energy ball-



THE HONG KONG POLYTECHNIC UNIVERSITY

- milling on ceramic oxides," *Mater. Sci. Forum*, vol. 235-238, no. 1, pp. 103-108, 1997.
- [50] J. Z. Jiang et al., "Gas-sensitive properties and structure of nanostructured (alpha-Fe₂O₃)_x-(SnO₂)_{1-x} materials prepared by mechanical alloying," *J. Phys. D: Appl. Phys.*, vol. 30, no. 10, pp. 1459-1467, 1997.
- [51] M. Simoneau, G. L'Esperance, M. L. Trudeau, and R. Schulz, "Structural and magnetic characterization of granular YBa₂Cu₃O_{7-δ} nanocrystalline powders," *J. Mater. Res.*, vol. 9, no. 3, pp. 535-540, 1994.
- [52] G. Nicoara, D. Fratiloiu, M. Nogues, J. L. Dormann, and F. Vasiliu, "Ni-Zn ferrite nanoparticles prepared by ball milling," *Mater. Sci. Forum*, vol. 235-238, no. 1, pp. 145-150, 1997.
- [53] S. B. Kim, S. J. Kim, C. H. Kim, W. S. Kim, and K. W. Park, "Nanostructure cathode materials prepared by high-energy ball milling method," *Mater. Lett.*, vol. 65, pp. 3313-3316, 2011.
- [54] A. O. Aning, C. Hong, and S. B. Desu, "Novel synthesis of lead titanate by mechanical alloying," *Mater. Sci. Forum.*, vol. 179-181, pp. 207-214, 1995.
- [55] L. B. Kong, T. S. Zhang, J. Ma, and F. Boey, "Progress in synthesis of ferroelectric ceramic materials via high-energy mechanochemical technique," *Prog. Mater. Sci.*, vol. 53, pp. 207-322, 2008.
- [56] K. P. Sanosh, A. Balakrishnan, L. Francis, and T. N. Kim, "Sol gel synthesis of forsterite nanopowders with narrow particle size distribution," *J. Alloys Compd.*, vol. 495, pp. 113-115, 2011.
- [57] R.H. Arendt, J.H. Rosolowski, and J.W. Szymaszek, "Lead zirconate titanate ceramics from molten salt solvent synthesized powders," *Mater. Res. Bull.*, vol. 14, no. 5, pp. 703-9, 1979.
- [58] S.K.S. Parashar, R.N.P. Choudhary, and B.S. Murty, "Ferroelectric phase transition in Pb_{0.92}Gd_{0.08}(Zr_{0.53}Ti_{0.47})_{0.98}O₃ nanoceramic synthesized by high-energy ball milling," *J. Appl. Phys.*, vol. 94, no. 9, pp. 6091-6, 2003.
- [59] E.L. Eskandarani and M. Sherif, *Mechanical Alloying for Fabrication of advanced Engineering Materials*, 14th ed. Norwich, New York, Noyes, Pub,



THE HONG KONG POLYTECHNIC UNIVERSITY

- 2001.
- [60] G. Alrt, et. al., "Dielectric properties of fine-grained barium titanate ceramics," *J. Appl. Phys.*, vol. 58, no. 4, pp. 1619-1625, 1985.
- [61] A. Wu and et.al., "Sol-gel preparation of lead zirconate titanate powders and ceramics: effect of alkoxie stabilizers and lead precursors," *J. Am. Ceram. Soc.*, vol. 83, no. 6, pp. 1379-85, 2000.
- [62] L. B. Kong, W. Zhu, and O. K. Tan, "PbTiO₃ ceramics derived from high-energy ball milled nano-sized powders," *J. Mater. Sci. Lett.*, vol. 19, pp. 1963-1966, 2000.
- [63] L. Cheng et al., "Fabrication of nanopowder by high energy ball milling and low temperature sintering of Mg₂SiO₄ microwave dielectrics," *J. Alloys Compd.*, vol. 513, pp. 373-377, 2012.
- [64] T. Hasegawa and T. Otagiri, "Dielectric Properties and Microstructures of Low-Temperature-Sintered BaTiO₃-Based Ceramics with CuBi₂O₄ Sintering Aid," *Jpn. J. Appl. Phys.*, vol. 45, pp. 7360-7364, 2006.
- [65] Y. M. Li et al., "Low Temperature sintering of high performance KNN-based lead-free piezoelectric ceramic using BCBM frit as sintering aid," *J. Electroceram.*, 2013.
- [66] I. Smeltere, M. Antonova, A. Kalvane, O. Grigs, and M. Livinsh, "The Effect of Dopants on Sintering and Microstructure of Lead-free KNN Ceramics," *Mater. Sci. (MEDŽIAGOTYRA)*, vol. 17, no. 1, 2011.
- [67] K. Kakimoto, K. Ando, and H. Ohsato, "Grain Size Control of Lead-free Li_{0.06}(Na_{0.5}K_{0.5})_{0.94}NbO₃ Piezoelectric Ceramics by Ba and Ti Doping," *J. Eur. Ceram. Soc.*, vol. 30, pp. 295-299, 2010.
- [68] A. Bencan, J. Bernard, J. Tellier, B. Malic, and M. Kosec, "The Influence of Alkaline Germanate Based Liquid Phase Sintering Aid on Microstructure and Phase Composition of K_{0.5}Na_{0.5}NbO₃ Ceramics," *Microsc. Microanal.*, vol. 15, pp. 786-787, 2009.
- [69] R. Sasaki, R. Suzuki, S. Uraki, H. Kakemoto, and T. Tsurumi, "Low-temperature sintering of alkaline niobate based piezoelectric ceramics using sintering aids," *J.*



THE HONG KONG POLYTECHNIC UNIVERSITY

- Ceram. Soc. Jpn.*, vol. 116, no. 11, pp. 1182-1186, 2008.
- [70] T. Hayashi, T. Inoue, and Y. Akiyama, "Low-Temperature Sintering and Properties of (Pb, Ba, Sr)(Zr, Ti, Sb)O₃ Piezoelectric Ceramics Using Sintering Aids," *Jpn. J. Appl. Phys.*, vol. 38, pp. 5549-5522, 1999.
- [71] H. Y. Wong, "Development of Lead-free Piezoelectric Ceramic Resonators for High-frequency Oscillator Applications," The Hong Kong Polytechnic University The Department of Applied Physics, Thesis 2008.
- [72] N Maluf and K Williams, *An Introduction to Microelectromechanical System Engineering*. London: Artech House, 2004.
- [73] T. J. Wielenga, "Anti-rollover brake system," U.S. Patent No 6065558, 2000.
- [74] K. Shimada, S. Horikoshi, and T. Monji, "Anti-skid control system for vehicle," U.S. Patent No 5219212, 1993.
- [75] R. D. Rallison et al., "Head-mounted personal visual display apparatus with image generator and holder," U.S. Patent No 6369952, 2002.
- [76] J. C. Zufferey, A. Klaptocz, A. Beyeler, J. D. Nicoud, and D. Floreano, "A 10-gram microflyer for vision-based indoor navigation," *Intelligent Robots and Systems, 2006 IEEE/RSJ International Conference on IEEE*, pp. 3267-3272, 2006.
- [77] W. D. McComb, *Dynamics and Relativity*. Oxford: Oxford University Press, 1999.
- [78] A. O. Persson, "The Coriolis Effect: Four centuries of conflict between common sense and mathematics, Part I: A history to 1885," *History of Meteorology*, vol. 2, pp. 1-24, 2005.
- [79] J.S. Burdess, A.J. Harris, J. Cruickshank, D. Wood, and G. Cooper, "A review of vibratory gyroscopes," *Engineering Science and Education Journal*, pp. 249-254, 1994.
- [80] J. Soderkvist, "Micromachined gyroscopes," *Sensors and Actuators A*, no. 43, pp. 65-71, 1994.
- [81] I.A. Ulitko, "Mathematical theory of the fork-type wave gyroscope," *Proc. IEEE International Frequency Control Symp.*, pp. 786-793, 1995.



THE HONG KONG POLYTECHNIC UNIVERSITY

- [82] W.D. Gates, "Vibrating angular rate sensor may threaten the gyroscope," *Electronics*, no. 41, 130-134 1968.
- [83] S. Fujishima, T. Nakamura, and K. Fujimoto, "Piezoelectric vibratory gyroscope using flexural vibration of a triangular bar," *Proc. IEEE 45th annual symp. on Frequency Control*, pp. 261-265, 1991.
- [84] C.S. Chou, J.W. Yang, Y.C. Huang, and H.J. Yang, "Analysis on vibrating piezoelectric beam gyroscope," *Int. J. of Applied Electromagnetics in Materials*, no. 2, pp. 227-241, 1991.
- [85] J. Soderkvist, "Piezoelectric beams and vibrating angular rate sensors," *IEEE Trans. Ultrasonic, Ferroelectrics, and Frequency Control*, no. 38, pp. 271-280, 1991.
- [86] J.S. Yang, H.Y. Fang, and Q. Jiang, "Analysis of a bimorph piezoelectric gyroscope," *International Journal of applied Electromagnetics and Mechanics*, no. 10, pp. 459-473, 1999.
- [87] G.M. Reese, E.L. Marek, and D.W. Lobitz, "Three-dimensional finite element calculations of an experimental quartz resonator sensor," *Proc. IEEE Ultrasonics Symp.*, pp. 419-422, 1989.
- [88] J.S. Yang, "Analysis of ceramic thickness shear piezoelectric gyroscopes," *J. Acoust. Soc. Am.*, no. 102, pp. 3542-3548, 1997.
- [89] H Abe, T Yoshida, and H. Watanabe, "Energy trapping of thickness-shear vibrations excited by parallel electric field and its applications to piezoelectric vibratory gyroscopes," *Proc. IEEE int. Ultrasonics Symp.*, pp. 467-471, 1998.
- [90] J.S. Yang, H.Y. Fang, and Q. Jiang, "A vibrating piezoelectric ceramic shell as a rotation sensor," *Smart Materials and Structures*, no. 9, pp. 445-451, 2000.
- [91] J.S. Burdess and T. Wren, "The theory of a piezoelectric disk gyroscope," *IEEE Transactions on Aerospace and Electronic Systems AES-22*, pp. 410-418, 1986.
- [92] J.S. Burdess, "The dynamics of a thin piezoelectric cylinder gyroscope," *Proc. Inst. Mech. Engrs 200(C4)*, pp. 271-280, 1986.
- [93] P.W. Loveday, "A coupled electromechanical model of an imperfect piezoelectric vibrating cylinder gyroscope," *J. Intell. Mater. Syst. Struct.*, no. 7, pp. 44-53,



THE HONG KONG POLYTECHNIC UNIVERSITY

1996.

- [94] Y. Kagawa, T. Tsuchiya, and T. Kawashima, "Finite element simulation of piezoelectric vibrator gyroscopes," *IEEE Transactions on Ultrasonics, Ferroelectrics, and Frequency Control*, no. 43, pp. 509-518, 1996.
- [95] J.S. Yang, H.Y. Fang, and Q. Jiang, "One-dimensional equations for a piezoelectric ring and applications in a gyroscope," *IEEE Transactions on Ultrasonics, Ferroelectrics, and Frequency Control*, no. 48, pp. 1275-1282, 2001.
- [96] J. S. Yang, H. Y. Fang, and Q. Jiang, "Analysis of a Few Piezoelectric Gyroscopes," *Frequency Control Symposium and Exhibition*, pp. 79-86, 2000.
- [97] W. D. Callister, *Materials science and engineering: an introduction*, 4th ed. New York: John Wiley & Sons, 1997.
- [98] H. Tanaka, A. Yamamoto, J. Shimoyama, H. Ogino, and K. Kishio, "Strongly connected ex situ MgB₂ Polycrystalline bulks fabricated by solid-state self-sintering," *Supercond. Sci. Technol.*, vol. 25, p. 115022, 2012.
- [99] C. B. Sawyer and C. H. Tower, "Rochelle Salt as a Dielectric," *Physical Review*, vol. 35, p. 269, 1930.
- [100] C. A. Randall, N. Kim, J. P. Kucera, W. Cao, and T. R. ShROUT, "Intrinsic and Extrinsic Size Effects in Fine-Grained Morphotropic-Phase Boundary Lead Zirconate Titanate Ceramics," *J. Am. Ceram. Soc.*, vol. 81, no. 3, pp. 677-688, 1998.
- [101] C. Wang et al., "Effect of high-energy ball milling time on superconducting properties of MgB₂ with low purity boron powder," *Superconductor Science And Technology*, vol. 25, p. 035018, 2012.
- [102] Y. Zhen and J. F. Li, "Normal Sintering of (K, Na) NbO₃-Based Ceramics: Influence of Sintering Temperature on Densification, Microstructure, and Electrical Properties," *J. Am. Ceram. Soc.*, vol. 89, no. 12, pp. 3669-3675, 2006.
- [103] J. Nowotny, *Science of Ceramic Interfaces II*. Australia: Newnes, 1995.
- [104] P. Morse, *Vibration and sound*, 2nd ed. New York: McGraw-Hill, 1948.
- [105] S. Nasiri, D. Sachs, and M. Maia, "Selection and integration of MEMS-based motion processing in consumer apps," *DSP Design Line*, 2009.

